Search for Excited Electrons with the DØ Experiment at the Tevatron Collider

von

Volker Vorwerk

Diplomarbeit in Physik

vorgelegt der

Fakultät für Mathematik, Informatik und
Naturwissenschaften
der RWTH Aachen

im Oktober 2006

angefertigt am

III. Physikalischen Institut A
Professor Dr. Thomas Hebbeker

don't panic

D. Adams

Contents

List of Figures

List of Tables

1. Introduction

What are the fundamental components of matter? This is the mainspring for physicists to explain nature. They started with small experiments like the Rutherford gold-foil scattering experiment. It was the first time that individual particles were scattered and detected. In the middle of the last century, small synchrotrons were built, which accelerate electrons with the aid of electric fields. Magnetic fields keep the electrons on a constant orbit. Larger and larger synchrotrons were built, until in 1992 the Tevatron accelerator was taken into operation. With $\sqrt{s} = 1.96\,\text{TeV}$ it is the collider with the largest center-of-mass energy on earth.

All these experiments led to the discovery of a motley collection of particles. To describe this "particle zoo", the Standard Model was formulated during the 1960ies. It is a sophisticated gauge theory that is based on invariance under symmetry operations. Due to Noethers theorem, these cause the existence of conservation laws. Every particle corresponds to a field and every symmetry to a gauge field, which mediate the forces. Both can interact with each other.

The Standard Model is composed of the electroweak and the strong theory. The electroweak interaction is the unification of the electromagnetic and the weak interaction. Until today, the Standard Model is confirmed experimentally to a high accuracy. Leptons and quarks are the elementary particles of the Standard Model. Their interaction is mediated via bosons, the W-boson, Z-boson, the photon and the gluon. The leptons and quarks are classified in three generations.

However, there are open questions which the Standard Model does not solve. The Higgs-boson, which is supposed to generate the masses due to its coupling to the particles, was not discovered yet. Also the hierarchical mass structure of the three generations is still a mystery. This is often taken as an evidence for a more fundamental substructure. Possibly, the leptons and quarks of the Standard Model are only the lowest states of excitation.

In this work the search for an excited electron is performed. Two models have been formulated to explain an effective interaction of excited quarks and leptons, the gauge-mediated and the contact interaction. These interactions are characterized by the compositeness scale Λ. In this analysis the production via contact interaction and the decay via gauge-mediated interaction is considered.

The final state consists of two electrons and a photon. Some predictions for the final state of excited electron produced via gauge-mediated interaction are made.

About $1\,\text{fb}^{-1}$ of data was recorded with the DØ Detector and is analyzed in this search. The DØ detector is one of the two main experiments at the Tevatron

collider. This multipurpose detector as well as the Tevatron are explained with main attention to the most important components for this analysis.

Expected background originating from Standard Model processes having the same final state, is generated via Monte Carlo simulation techniques. The data as well as the simulated events are pre-selected to check their agreement. A very good description of data by the Monte Carlo events is found. A final sample of events that contain the three final state particles is selected. The requirements for both samples as well as the methods to identify the particles are explained.

However, no excess of data is observed in the di-electron gamma sample. Limits on the production cross section via contact interaction and the mass of excited electrons are set, as well as on the compositeness scale Λ.

2. The Standard Model

In this chapter the Standard Model of particle physics is discussed briefly with special focus on the interactions between the elementary particles that are mediated by gauge fields (Sec. 2.1 and 2.2). Also the Higgs mechanism generating the masses of the particles is introduced shortly in Sec. 2.3. At last, open questions of the Standard Model are mentioned in Sec. 2.4. For more detailed information see for example in [9–11].

Since the early 1930ies a lot of new particles were discovered. Thus, at the beginning of the 1960ies the physicists found themselves confronted with a large spectrum of different particles, often called "particle zoo".

During the 1960ies the Standard Model (SM) was formulated [12–14]. It is a sophisticated theory to provide a framework for this particle zoo and it is confirmed to a high accuracy (see for example [1] and Fig. 2.1). It can be described by means of a quantum field theory, representing particles by interacting matter-fields.

The SM includes the electroweak (EW) interaction and the strong interaction, or quantum chromodynamics (QCD). The electroweak interaction is the unification of quantum electrodynamics (QED) and weak interaction.

The elementary particles of the SM are leptons and quarks, fermions with spin $1/2$ (see Tab. 2.1). In the same way as in quantum mechanics a Lagrangian $\mathcal{L}$ is formulated, from which the equations of motion can be derived. This is for the corresponding non-interacting fields of fermions the Dirac equation. The four-dimensional Dirac spinors, the wave function of fermions, have to satisfy the Dirac equation.

$$(i\gamma^\mu \partial_\mu - m)\,\psi(x) = 0\,, \tag{2.1}$$

where $\mu = 0, 1, 2, 3$ is the space-time index[1], γ^μ are the 4×4 Dirac matrices, m is the fermion mass, and $\partial_\mu = (\partial_0, \nabla)$ the four-dimensional gradient. The Dirac equation has four independent solutions, which differ in their spin states: two solutions for spin $+1/2$ and two for $-1/2$. For each spin state one solutions correspond to a particle (positive energy) and one to an anti-particle (negative energy).

The interaction is mediated via gauge bosons of spin 1: the photon, the Z-boson, the W-boson and the gluon. When the Standard Model was invented, the idea of forces mediated by particles was new and extraordinary. But this feature originates from the design of the SM as a gauge theory. The SM im-

[1] The Einstein summation convention is applied in this analysis.

plements local gauge symmetries, i. e. the invariance of the theory under local transformations $U(x)$,

$$\psi(x) \rightarrow U(x)\psi(x) = \psi'(x)\,. \tag{2.2}$$

U describes a symmetry if equations of motion remain invariant under such transformations. All such transformations for one symmetry form a Lie-group. Due to the Noether theorem[2] these symmetries yield the existence of conservation laws.

The concept of the SM is to demand symmetries and fermion fields and to construct from these the most general Lagrangian. Since the Dirac equation is not invariant under local symmetries, like for example the special unitary group $SU(2)$, one or more additional vector-fields are introduced. This leads to the above mentioned gauge bosons[3].

2.1. Electroweak Interaction

Following this ansatz the Lagrangian for fermions f is

$$\mathcal{L} = \sum_f \bar{\psi}_f \left(i\,\gamma_\mu\,\partial^\mu - m\right)\psi_f \tag{2.3}$$

with the anti-fermion $\bar{\psi}_f = \psi_f^\dagger \gamma^0$. Fermions are characterized for example by the spin orientation, chirality, and their quantum numbers, i. e. the electrical charge, the hyper-charge, and the isospin. The chirality is the alignment between the spin orientation and the direction of motion. It corresponds to the helicity in case of massless particles and is defined as

parallel alignment	$\equiv + \equiv$ right-handed	$\rightarrow \psi_r = \frac{1+\gamma^5}{2}\,\psi$
anti-parallel alignment	$\equiv - \equiv$ left-handed	$\rightarrow \psi_l = \frac{1-\gamma^5}{2}\,\psi$

The left-handed fermions form weak isospin doublets whereas the right-handed ones form singlets (Tab. 2.1). The $SU(2)$ describes the transformations of the

Leptons			Quarks		
$\begin{pmatrix}\nu_e\\ e\end{pmatrix}_L$	$\begin{pmatrix}\nu_\mu\\ \mu\end{pmatrix}_L$	$\begin{pmatrix}\nu_\tau\\ \tau\end{pmatrix}_L$	$\begin{pmatrix}u\\ d'\end{pmatrix}_L$	$\begin{pmatrix}c\\ s'\end{pmatrix}_L$	$\begin{pmatrix}t\\ b'\end{pmatrix}_L$
$\nu_{eR},\ e_R$	$\nu_{\mu R},\ \mu_R$	$\nu_{\tau R},\ \tau_R$	$u_R,\ d_R$	$c_R,\ s_R$	$t_R,\ b_R$

Table 2.1.: The elementary particles in the Standard Model listed in singlets and doublets.

weak isospin for the left-handed doublets. Transformations of the hyper-charge

[2] To every differentiable symmetry generated by local actions corresponds a conserved current.
[3] Up to this point the bosons are still massless, see Sec. 2.3.

are described by the unitary Lie-group $U(1)_Y$, where the index Y is added to mention that this is not the symmetry $U(1)$ of QED.

The generators of the $SU(2)$ are the weak isospin operators, the Pauli-matrices τ_i $(i = 1, 2, 3)$, or $\mathbf{T} = \boldsymbol{\tau}/2$ with the corresponding gauge fields W_μ^i $(i = 1, 2, 3)$. Generator of the $U(1)_Y$ is the hyper-charge operator $\mathbf{Y}$ and its corresponding gauge field is B_μ. Thus, the symmetry group for the EW theory is $SU(2) \times U(1)_Y$.

The gauge fields are introduced with the following transformations

$$B'^{\mu} = B^{\mu} - \partial^{\mu}\chi(x)\,, \tag{2.4}$$

$$W_i'^{\mu} = W_i^{\mu} - \partial^{\mu}\beta_i(x) - g\,\varepsilon_{ijk}\beta_j(x)W_k^{\mu}\,, \tag{2.5}$$

where ε_{ijk} is the structure constant of the $SU(2)$ symmetry group, $\chi(x)$ and $\beta(\mathbf{x})$ are phases.

The fields are implemented via a covariant derivation

$$D^{\mu} = \partial^{\mu} + i\,g\,\mathbf{T}\cdot\mathbf{W}^{\mu} + i\,\frac{g'}{2}\mathbf{Y}B^{\mu}\,, \tag{2.6}$$

of the Lagrangian, where g' and g are the electroweak coupling constants for $U(1)_Y$ and $SU(2)$, respectively. The gauge bosons are linear combinations of the vector-fields $\mathbf{W}_\mu$, B_μ and A_μ, which mediates the electromagnetic force, such that

$$W^{\pm} \equiv W^{\pm\mu} = 1/\sqrt{2}\,(W_1^{\mu} \pm W_2^{\mu})\,, \tag{2.7}$$

$$\gamma \equiv A^{\mu} = W_3^{\mu}\sin\theta_W + B^{\mu}\cos\theta_W\,, \tag{2.8}$$

$$Z \equiv Z^{\mu} = W_3^{\mu}\cos\theta_W - B^{\mu}\sin\theta_W\,, \tag{2.9}$$

The properties of the gauge bosons are listed in Tab. 2.2.

	γ	W	Z
mass [GeV]	$< 6 \cdot 10^{-26}$	80.425 ± 0.038	91.1876 ± 0.0021
lifetime [s]	∞	$\sim 3 \cdot 10^{-25}$	$\sim 3 \cdot 10^{-25}$
range [m]	∞	$\sim 10^{-18}$	$\sim 10^{-18}$
spin	1	1	1
charge	0	1	0

Table 2.2.: Properties of the gauge bosons of the Electroweak Interaction [7].

This mixing of the $SU(2)$ fields and $U(1)_Y$ field is described by the weak mixing angle or Weinberg angle θ_W. It can be written in terms of the electroweak coupling constants

$$\cos\theta_W = \frac{g}{\sqrt{g^2 + g'^2}} \quad \text{and} \quad \sin\theta_W = \frac{g'}{\sqrt{g^2 + g'^2}}\,. \tag{2.10}$$

The three charges, namely the electromagnetic charge Q, the hyper-charge Y, and the weak isospin I are coupled via the Gell-Mann-Nishijima relation

$$Q = T_3 + \frac{Y}{2} \tag{2.11}$$

fermion	electrical charge Q	hyper-charge Y	Isospin T_3
e_R, μ_R, τ_R	-1	-2	0
ν_{eL}, $\nu_{\mu L}$, $\nu_{\tau L}$	0	-1	$+1/2$
e_L, μ_L, τ_L	-1	-1	$-1/2$
u_R, c_R, t_R	$+2/3$	$+4/3$	0
d_R, s_R, b_R	$-1/3$	$-2/3$	0
u_L, c_L, t_L	$+2/3$	$+1/3$	$+1/2$
d_L, s_L, b_L	$-1/3$	$+1/3$	$-1/2$

Table 2.3.: The quantum numbers for leptons and quarks, divided into left-handed and right-handed fermions.

where T_3 is the third component of the isospin. The quantum numbers of fermions[4] are listed in Tab. 2.3.

Weak eigenstates with the same quantum numbers (Q, Y, T) can interfere with each other, which leads to the mixing of quarks. Because decay modes like for example $\mu \to e\gamma$ are not observed, additional quantum numbers are introduced, i. e. the electron number[5], muon number and the tau number.

However, this feature is only possible for left-handed quarks, i. e. for charged weak currents, because right-handed quarks do not couple to the W-boson. Electromagnetic and neutral weak currents are not affected by the mixing due to the commutation of the Dirac matrices γ^μ with the transformation that mediates between the symmetry eigenstates and the mass eigenstates, e. g. q' and q, respectively.

For quarks is the mixing characterized by the Cabibbo-Kobayashi-Maskawa-matrix

$$\begin{pmatrix} d' \\ s' \\ b' \end{pmatrix}_L = \begin{pmatrix} V_{ud} & V_{us} & V_{ub} \\ V_{cd} & V_{cs} & V_{cb} \\ V_{td} & V_{ts} & V_{tb} \end{pmatrix} \cdot \begin{pmatrix} d \\ s \\ b \end{pmatrix}_L \tag{2.12}$$

The matrix elements V_{ij} are free parameters of the SM and have to be determined experimentally.

Summarizing, the Lagrangian of the electroweak interaction can be written as

$$\begin{aligned} \mathcal{L} \;=\; & -\frac{1}{4}\mathbf{W}_{\mu\nu}\mathbf{W}^{\mu\nu} - \frac{1}{4}B_{\mu\nu}B^{\mu\nu} \\ & + \bar{L}\,\gamma^\mu (i\,\partial_\mu - g\frac{1}{2}\boldsymbol{\tau}\mathbf{W}_\mu - g'\,\frac{Y}{2}B_\mu)L \\ & + \bar{R}\,\gamma^\mu (i\,\partial_\mu - g'\,\frac{Y}{2}B_\mu)R\,, \end{aligned} \tag{2.13}$$

where L are the left-handed lepton and quark doublets and R the right-handed lepton and quark singlets.

[4]The anti-fermions have opposite sign quantum numbers and the same masses.

[5]The electron number is $+1$ for e^- and ν_e, -1 for e^+ and $\bar{\nu}_e$, and 0 for all other particles, analog for muon and tau number.

2.2. Strong Interaction

QCD was constructed to explain the structure of hadrons. For example the existence of the Δ^{++}-baryon, the bound state of three u-quarks, could not be explained. A "strong" force was demanded, that overrules the repulsion of the three u-quarks due to its electromagnetic charge. Another ambiguity was, that the wave function of the Δ^{++}-baryon is symmetric under permutations of two quarks, although quarks have spin $1/2$.

This lead to the introduction an additional "hidden" quantum number, to fulfill the Pauli principle[6]. The $SU(3)$ symmetry group was introduced, such that the symmetry for the SM can be written as

$$U(1)_Y \times SU(2) \times SU(3)_C \,. \tag{2.14}$$

$SU(3)$ gives the quarks three additional degrees of freedom, the colors red, blue, and green. One says quarks carry a color-charge. The color is mediated by gluons g, characterized by the gluon-fields G_j^μ. Their name originates from the confinement of the QCD: Quarks do not exist as free particles but only as colorless compositions and are thus "glued".

The generators of the $SU(3)$ are the eight Gell-Mann-matrices λ_i which are the 3-dimensional equivalents of the Pauli matrices, the generators of the $SU(2)$. As in Sec. 2.1, we consider the Dirac equation for free quarks. The wave function is now the product of the Dirac wave function ψ and a 3-dimensional color-spinor χ_C

$$\Psi = \psi \cdot \chi_C \,, \tag{2.15}$$

and the Dirac equation becomes

$$(i\gamma_\mu \partial^\mu - m)\Psi = 0 \,. \tag{2.16}$$

The $SU(3)$ transformation can then be written as

$$\Psi' \to \Psi \exp\left(i\frac{g''}{2}\lambda_i \beta_j(x)\right) \,. \tag{2.17}$$

The Lagrangian is derived following again the ansatz already applied in the EW theory. This yields to the Lagrangian of the QCD

$$\mathcal{L} = \bar{\Psi}(i\gamma_\mu D^\mu - m)\Psi - \frac{1}{4} F_{j,\mu\nu} F_j^{\mu\nu} \,, \tag{2.18}$$

where $F_j^{\mu\nu}$ is the field strength tensor

$$F_j^{\mu\nu} = \partial^\mu G_j^\nu - \partial^\nu G_j^\mu - g'' f_{jkl}\, G_k^\mu G_l^\nu \,. \tag{2.19}$$

The structure constants of the $SU(3)$ are f_{jkl}. Gluons, the bosons of the QCD, are massless and thus stable particles. They have spin 1 and carry neither electromagnetic charge nor hyper-charge or isospin.

[6] Two fermions having the same quantum numbers may not occupy the same quantum state simultaneously.

The coupling[7]

$$\alpha_S = \frac{g''^2}{4\pi}\,, \tag{2.20}$$

of the strong interaction depends on the momentum scale Q^2 of the interaction. This is characterized in a leading order approximation by the parametrization[8]

$$\alpha_S(Q^2) = \frac{12\pi}{(33 - 2n_f)\cdot \ln(Q^2/\Omega^2)}\,, \tag{2.21}$$

with $\Omega \ll Q^2$ and n_f is the number of flavors, i. e. quarks. Since the coupling decreases towards zero for $Q^2 \to \infty$, the quarks can propagate as if they were free (asymptotic freedom).

In contrast the coupling α_S diverges for low Q^2, a phenomenon which is called confinement. This is the case for distances larger then roughly 1 fm. Thus, a quark anti-quark pair is energetically preferred compared to single quarks. The quarks fragment into hadrons and the typical structure of a jet emerges.

2.3. The Higgs Mechanism

It is known from measurements that both the W-boson and the Z-boson are massive particles. The non-zero masses yield their short interaction length ($\approx \hbar c/M_V^2 c^2$). These characteristics are known since their discovery in the early 1980ies [15, 16].

Since only massless vector fields fulfill the gauge invariance under local transformations, the gauge theory predicts massless gauge bosons, which contradicts experimental observations. A possible solution is a background field that couples with the electroweak field. It allows an infinite range of the EW interaction which is shielded by the background field, the Higgs-field [17]. This generates the masses.

The complex Higgs-doublet

$$\phi = \begin{pmatrix} \phi^+ \\ \phi^0 \end{pmatrix} = \frac{1}{\sqrt{2}} \begin{pmatrix} \phi_1 + i\phi_2 \\ \phi_3 + i\phi_4 \end{pmatrix}\,, \tag{2.22}$$

with the, under $SU(2)$ transformations invariant, potential

$$V(\phi) = -\mu^2|\phi|^2 + \lambda^2|\phi|^4\,, \tag{2.23}$$

is chosen.

The Higgs-potential has its minimum ϕ_0 at $|\phi|^2 = \frac{\mu^2}{2\lambda^2} =: \frac{v}{\sqrt{2}}$, the vacuum state. This yields to a circle of ground states

$$(\phi_1^2 + \phi_2^2 + \phi_3^2 + \phi_4^2) = -\frac{\mu^2}{2\lambda} \tag{2.24}$$

[7] The coupling of the EW theory is $\alpha_{EW} = \sqrt{e/4\pi}$.

[8] Ω is often written as Λ which was not chosen here to avoid confusions with compositeness scale Λ in Ch. 3.

By choosing one, for example

$$\phi_0 = \frac{1}{\sqrt{2}} \begin{pmatrix} 0 \\ v \end{pmatrix} , \tag{2.25}$$

the invariance under the $SU(2)$ is not longer valid. The symmetry is spontaneously broken and the gauge invariance is hidden.

The vacuum state is expanded, e. g. due to quantum fluctuations, such that

$$\phi(x) = \frac{1}{\sqrt{2}} \begin{pmatrix} 0 \\ v + \eta(x) + i\zeta(x)) \end{pmatrix} . \tag{2.26}$$

Then the Lagrangian for the three gauge bosons of the EW theory can be written as

$$\begin{aligned} \mathcal{L} \;=\; & \frac{1}{2}[(\partial^\mu \eta)(\partial_\mu \eta) - 2\mu^2\eta^2] + \frac{1}{2}[(\partial^\mu \zeta)(\partial_\mu \zeta)] - \frac{1}{4}F^i_{\mu\nu}F^{i,\mu\nu} - \frac{1}{4}f_{\mu\nu}f^{\mu\nu} + \\ & + \frac{1}{2}\frac{g^2v^2}{4}\left(W^{(+)}_\mu|^2 + |W^{(-)}_\mu|^2\right) + \frac{1}{2}\frac{g^2v^2}{\cos^2\theta_W}|Z_\mu|^2 . \end{aligned} \tag{2.27}$$

The result is a neutral scalar boson, the Higgs-boson H with mass $m_H = \sqrt{2}\mu$, that is described by the Higgs-field η. As one can read off from Eq. 2.27, the W-boson and the Z-boson obtain mass terms, namely

$$m_W = \frac{gv}{2} \qquad \text{and} \qquad m_Z = \frac{gv}{2\cos\theta_W} . \tag{2.28}$$

However, the photon remains massless.

The Lagrangian can be extended such that the fermions obtain masses, too. It contains the so-called Yukawa couplings g_i and can be written as

$$\mathcal{L}_{Yukawa} = -\frac{v+\phi}{\sqrt{2}}(g_\nu\nu\nu + g_l ll + g_u uu + g_d dd) \tag{2.29}$$

where u and d means up-type and down-type fermions, respectively. The v-proportional terms induce the mass terms $m_f = {}^{v g_f}/\sqrt{2}$

The Higgs-boson has not been discovered yet and its mass is not predicted by the theory. Limits have been set for example by direct searches at the Large Electron and Positron Collider (LEP) [1, 15], $m_H > 114.4\,\text{GeV}$.

2.4. Shortcomings of the Standard Model

Although the SM is well tested at several experiments like the Tevatron, the LEP, and the SLAC[9] Linear Collider (see Fig. 2.1), some shortcomings remain. For example the origin of Dark Matter is not known yet. It is predicted to explain the almost constant rotation velocity of spiral galaxies up to large radii. The Supersymmetric Theory (SUSY) is an extension of the SM able to resolve this problem. SUSY associates every SM fermion with a SUSY boson and every SM boson with a SUSY fermion. Depending on the SUSY Model the Lightest

[9]Stanford Linear Accelerator Center

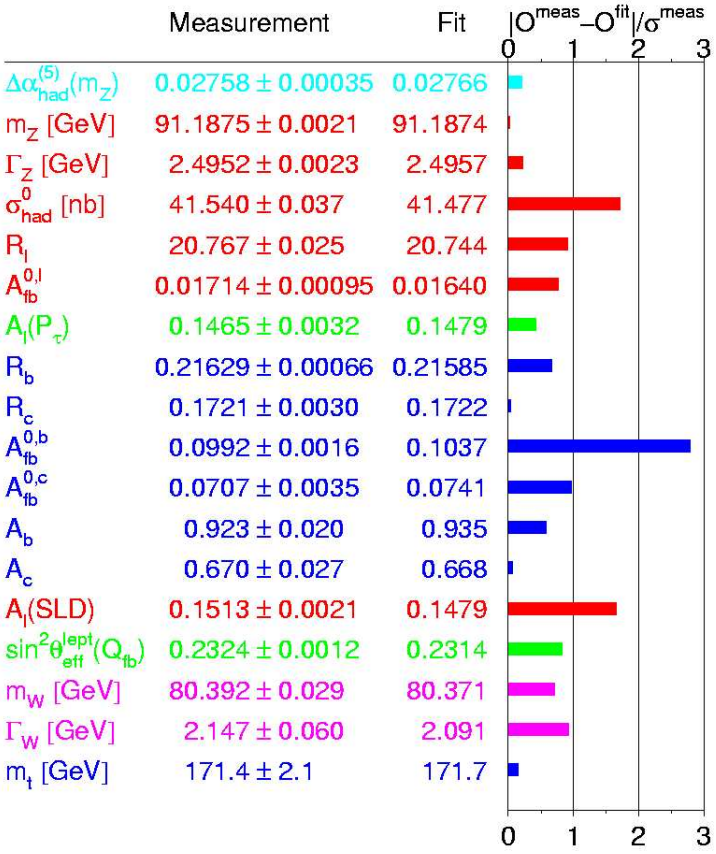

Figure 2.1.: Measurements of 18 free parameters of the Standard Model that are not a priori determined. The nineteenth is the Higgs mass. The differences between the measured values and the fit using Standard Model predictions divided by the measurements error are shown. The measured values are obtained from a fit to all measurements [1]. Since the deviation of the measurements is for almost all parameters within its uncertainties, the Standard Model is in agreement with its expectations.

Supersymmetric Particle (LSP) is stable, neutral, and only weakly interacting, and is therefore a good Dark Matter candidate.

Also a unification of the EW theory and QCD is aspired by physicists to obtain a Grand Unification Theory or even a Theory of Everything, by involving also the Gravitation. This is not provided by the SM. However, some SUSY models allow the unification of the Electroweak Theory, the QCD and the Gravitation.

Furthermore, the mass of neutrinos in the SM is set equal to zero. This arises from the absence of right-handed neutrino fields. But measurements for example at Kamiokande [18] led to the interpretation of differences between the mass eigenstates of the neutrinos ($\Delta m_{\nu_l} \neq 0$) [19]. For these measurements the oscillation between the different weak eigenstates of the neutrinos were

analyzed. The mixing is characterized by the Maki-Nakagawa-Sakata matrix[10].

In addition, the Higgs-boson which is supposed to generate the mass of the SM particles (see Sec. 2.3) was not discovered yet. An exclusion of the Higgs-boson would require a new mechanism for generation of particle masses.

Also the hierarchical mass structure of the SM fermions is not understood. A substructure of fermions would solve this problem. The search for such a substructure, hence resulting excited states is the subject of this analysis. Ch. 3 introduces the theoretical framework for excited leptons and fermions.

[10] analog to quark mixing, see Sec. 2.1

3. Excited Electrons

In this chapter a brief introduction is given to the theory of excited quarks and leptons, especially to excited electrons. Such excited states would occur due to a compositeness of these particles. As an attractive feature, this could explain the hierarchical structure of quarks and leptons, one of the shortcomings of the SM.

At first, the idea of those excited states is motivated. A substructure of "preons" with its new strong interaction is introduced. This is followed by an explanation of the model of single excited electrons (Sec. 3.1) and effective Lagrangian techniques (Sec. 3.2). In Sec. 3.3 the production of singly excited electrons is explained for two different kinds of interaction, the gauge-mediated interaction (GM) and the contact interaction (CI). Then the subsequent electron decay is discussed in Sec. 3.4, which is a GM decay into an electron and a photon.

The decision for the consideration of the particular channel $q\bar{q} \to e^*e \to ee\gamma$ in the rest of this work is motivated in this chapter. In Sec. 3.5 the most recent results for excited leptons are presented.

3.1. The Model of Excited States of Quarks and Leptons

The origin of the hierarchical structure of the quark and lepton $SU(2)$ doublets in the SM, i. e. the SM fermions, cannot be explained within the SM. The mass ratios between different generations reach up to $\mathcal{O} \sim 10^3$ for m_τ/m_e and $\mathcal{O} \sim 10^5$ for m_t/m_u. Also the motivation for the mixing angles is unknown.

This peculiarity of the SM can be taken as an evidence for a substructure [20–25]. The so-called Compositeness Model (CM) predicts for quarks and leptons a substructure of new particles. These supposed constituents are generally called Preons. They are bound by a new strong "precolor" interaction, which is characterized by the compositeness scale Λ. It is often compared to the non abelian QCD strong force (see Ch. 2). The compositeness scale Λ corresponds to the scale factor Ω of QCD. Analog, quarks and leptons are composite at the energies below Λ. Thus the SM would be only the low energy limit of a more fundamental theory. Even if the new strong precolor interaction is unknown, a model-independent effective Lagrangian technique can be used to describe it.

A substructure would lead to a large spectrum of excited states of SM fermions f^*, where quarks and leptons are assigned the lowest state of excitation. This implies that the preons are scalar and spin-1/2 particles (bosons

and fermions) or only spin-1/2 particles (fermions). In this analysis the more widespread use [20–23] of bosonic and fermionic preons was chosen. This choice is motivated by the fact that in this case the excited quarks and leptons get their masses prior to $SU(2) \times U(1)$ breaking [22].

The exchange of preons would lead to a new interaction between quarks and leptons. This interaction can be approximated by two different effective interactions, the gauge-mediated interaction (GM) (see Ch. 2) and the contact interaction (CI). Both are described in the following Sec. 3.2.

The excited SM fermions can be written down as $SU(2)$ doublets, such that for example the lightest lepton spectrum is

$$\begin{pmatrix} \nu_e \\ e^- \end{pmatrix}_L, e^-_R \qquad \begin{pmatrix} \nu_e^* \\ e^{-*} \end{pmatrix}_L, \begin{pmatrix} \nu_e^* \\ e^{-*} \end{pmatrix}_R . \tag{3.1}$$

In the following only excited electrons are considered. The results for all other leptons and quarks can be derived in complete analogy.

3.2. Effective Lagrangians

As already mentioned in Sec. 3.1, effective Lagrangian techniques are used to handle the unknown preon interaction. In both cases, i. e. GM and CI, the couplings depend on the compositeness scale Λ. Historically rooted, Λ is often set equal to the masses of the excited SM fermions [24, 26]. Also a value of $\Lambda = 6\,\text{GeV}$ was chosen in other studies, motivated by the fact that the case of $\Lambda = m_{e^*}$ seems unnatural from the theoretical point of view [23]. In this analysis, Λ is chosen equal 1 TeV and thus independent of the excited lepton or quark mass.

The mass of excited leptons and quarks is expected to be larger than their SM counter parts. This is reasonable because a substructure of leptons and quarks would lead to an additional contribution to the anomalous magnetic moment [27] of

$$\delta g \sim \mathcal{O}\left(\frac{m_{l,q}}{m_{l^*,q^*}}\right) . \tag{3.2}$$

Those contributions can be realized by additional vacuum polarization terms, e. g. a loop of an excited electron and a boson (see Fig. 3.1). The anomalous magnetic moment g for electrons and muons was measured precisely in the $(g-2)$ experiments [28]. Thus, m_{l^*,q^*} has to be large respective to $m_{l,q}$.

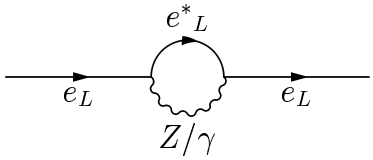

Figure 3.1.: Vacuum polarization due to a loop of an excited electron and a neutral gauge boson.

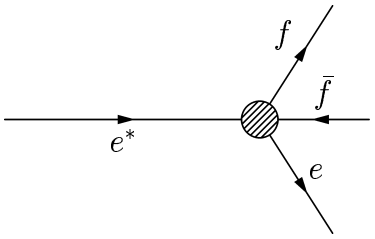

Figure 3.2.: Feynman diagram for the transition via contact interaction coupling of an excited electron to an electron and a fermion antifermion pair.

3.2.1. Contact Interaction

Contact Interaction (CI) between excited electrons as well as between excited and SM electrons can be seen analog two the four-fermion coupling introduced by Fermi. A yet not observed exchange of preons due to the new strong interaction would lead to this CI for energies below the compositeness scale Λ.

The effective Lagrangian for CI is [24]

$$\mathcal{L} = \frac{g_*^2}{\Lambda^2}\frac{1}{2} j^\mu j_\mu \,, \tag{3.3}$$

with

$$j_\mu = \eta_L \, \bar{f}_L \, \gamma_\mu \, f_L + \eta'_L \, \bar{f}^*_L \, \gamma_\mu \, f^*_L + \eta''_L \, \bar{f}^*_L \, \gamma_\mu \, f_L + h.c. + (L \to R) \,. \tag{3.4}$$

The arbitrary coupling constant[1] g^* is chosen to be equal 4π and η is set equal one for left-handed currents. Right-handed currents for simplicity are neglected, such that $\eta_R = 0$ [24]. Λ is the above introduced compositeness scale. The Feynman graph of this coupling is shown in Fig. 3.2.

For the signature $q\bar{q} \to e^*e \to ee\gamma$, the effective Lagrangian is reduced to

$$\mathcal{L} = \frac{g_*^2}{\Lambda^2}\frac{1}{2} \left(\bar{q}_L \gamma^\mu q_L\right) \left(\bar{e}^*_L \gamma_\mu e_L\right) \,. \tag{3.5}$$

3.2.2. Gauge Mediated Interaction

The transitions between SM and excited electrons can also be mediated by gauge bosons (see Tab. 2.2) as shown in Fig. 3.3. The effective and gauge invariant Lagrangian thus is [24]

$$\mathcal{L} = \frac{1}{2\Lambda} \bar{f}^*_R \, \sigma^{\mu\nu} \left(g'' f_s \frac{\lambda^a}{2} G^a_{\mu\nu} + g f \frac{\boldsymbol{\tau}}{2} \mathbf{W}_{\mu\nu} + g' f' \frac{Y}{2} B_{\mu\nu} \right) f_L + h.c. \,, \tag{3.6}$$

where $G^a_{\mu\nu}$,$W_{\mu\nu}$, and $B_{\mu\nu}$ are the field-strength tensors of the gluon, the $SU(2)$ and the U(1) gauge field. In contrast to the EW theory (see Sec. 2.1), the gauge

[1] It is chosen analogously to the $SU(2)_L$ and $U(1)_Y$ coupling constants g and g', see Sec.2.1

fields are derived to keep the Lagrangian gauge invariant[2]

$$W^i_{\mu\nu} = \partial_\mu W^i_\nu - \partial_\nu W^i_\mu - g\,\varepsilon_{ijk} W^j_\mu W^k_\nu\,, \tag{3.7}$$

$$B_{\mu\nu} = \partial_\mu B_\nu - \partial_\mu B_\nu\,. \tag{3.8}$$

Y gives the hyper-charge of the considered particle (see Ch. 2), which is the

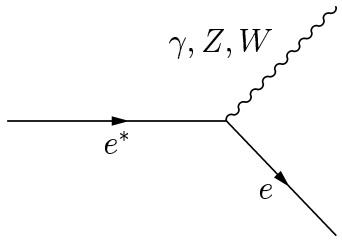

Figure 3.3.: Feynman graph of the coupling of an excited electron to a boson and an electron.

same as for ground states. g, g', and g'' are the three $U(1)$, $SU(2)$, and $SU(3)$ gauge couplings, respectively, $\sigma^{\mu\nu}$ is a commutator of γ-matrices, such that

$$\sigma^{\mu\nu} = \frac{i}{2}\left(\gamma^\mu\gamma^\nu - \gamma^\nu\gamma^\mu\right). \tag{3.9}$$

The parameters f and f' are determined by the composite dynamics. These parameters control the coupling between photons, excited electrons and excited neutrinos. For this analysis ($f = f'$) is chosen, which excludes the coupling between excited neutrinos and photons [22]. This becomes clear looking at the derivative of the action S over the fields for the particular coupling $\nu\,\nu^*\gamma$, which is

$$\sim \left(f \cdot \gamma^\nu_{ac}\gamma^\mu_{cb} - f \cdot \gamma^\mu_{ac}\gamma^\nu_{cb} + Y \cdot f' \cdot \gamma^\nu_{ac}\gamma^\mu_{cb} - Y \cdot f' \cdot \gamma^\mu_{ac}\gamma^\nu_{cb}\right). \tag{3.10}$$

It is explained in more detail in App. A.2.

3.3. Production Mechanism

The focus in on the production of only single excited electrons, since the cross section for excited electron-pair production is smaller and the required center-of-mass energy is larger.

The cross section for excited electron production via GM is only about 0.1 % of the cross section for production via CI (see Fig. 3.4). The values were taken from PYTHIA [29] in the case of CI and from the COMPHEP [30] implementation of excited electrons (see App. A.2) in the case of GM. The results for GM agree with those from other searches [21] within the theoretical uncertainties as well as the results for CI [20].

The CI cross section term is given by [24]

$$\hat{\sigma}\left(q\bar{q} \to e\bar{e}^*, e^*\bar{e}\right) = \frac{\pi}{6\,\hat{s}}\left(\frac{\hat{s}}{\Lambda^2}\right)^2\left(1+\frac{v}{3}\right)\left(1-\frac{m^2_{e^*}}{\hat{s}}\right)^2\left(1+\frac{m^2_{e^*}}{\hat{s}}\right), \tag{3.11}$$

[2]Note that the compositeness scale Λ has dimension mass.

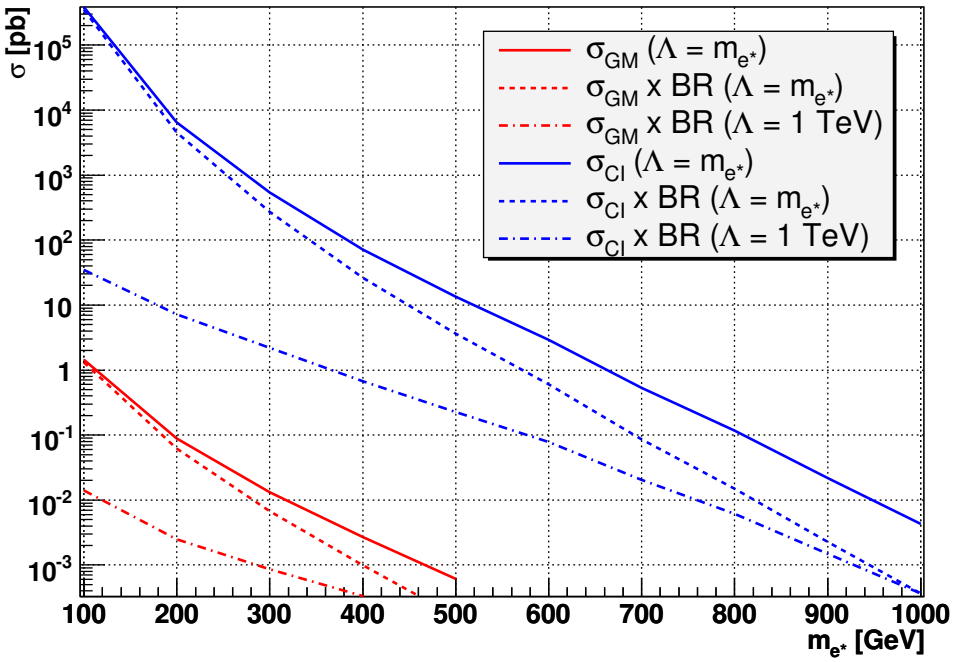

Figure 3.4.: Cross sections for single excited electron produced via gauge-meditated and contact interaction, and for different compositeness scales calculated with COMPHEP (see Appendix A.2).

were

$$v = \frac{\hat{s} - m_{e^*}^2}{\hat{s} + m_{e^*}^2}, \tag{3.12}$$

and $\hat{s}$ is the squared center-of-mass energy. As mentioned in Sec. 3.1 the underlying interaction is unknown and it is still not clear which interaction model describes it. This means that though CI cross sections are larger, GM production should be analyzed as well.

3.4. Decay

The partial width are for the gauge-mediated interaction [24]

$$\Gamma_{GM}\left(e^* \to lV\right) = \frac{1}{8}\frac{g_V^2}{4\pi} f_V^2 \frac{m_{e^*}^3}{\Lambda^2}\left(1 - \frac{m_V^2}{m_{e^*}^2}\right)^2\left(2 + \frac{m_V^2}{m_{e^*}^2}\right), \tag{3.13}$$

where V is the gauge boson (γ, Z, or W). The constant f_V is for the particular boson

$$f_\gamma = f\,T_3 + f'\,\frac{Y}{2},\,, \tag{3.14}$$

$$f_Z = f\,T_3\cos^2\theta_W - f'\frac{Y}{2}\sin^2\theta_W\,, \tag{3.15}$$

$$f_W = \frac{f}{\sqrt{2}}\,. \tag{3.16}$$

T_3 is the third component of the weak isospin of the excited electron. It has the same value as for the ground state. The constant g_V is the coupling constant for the gauge bosons, namely $g_\gamma = \alpha$, $g_W = e/\sin\theta_W$, and $g_Z = g_W/\cos\theta_W$.

The impact of the two constants f and f' becomes clear again looking for example at Eq. 3.14. By choosing $f = f'$ we obtain $f_\gamma = -1$. The partial width for the decay via γ radiation would be zero for $f = -f'$.

This analysis concentrates on the decay by radiating a photon, such that the final state is $ee\gamma$, see Fig. 3.5. This is the preferred decay mode if a leptonic

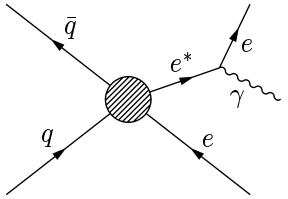

Figure 3.5.: Feynman graph for the analyzed process $q\bar{q} \to e^*e$.

final state is demanded, more exactly a decay into an electron or a muon, since for both the signal is clearer. Fig. 3.6 shows the BRs for the the possible final states. One can see that the renormalized BR for the chosen channel ($e^* \to e\gamma$) is nearly constant for high e^* masses at about 0.68. The BR is renormalized for all possible decays with electron or muon final states, for example for the $ee\gamma$ channel

$$BR(e^* \to e\gamma) = \frac{\Gamma(e^* \to e\gamma)}{\sum_{V=\gamma,Z,W}\Gamma_{GM}\,(l^* \to lV)}\,. \tag{3.17}$$

The partial with for the three-body-decay via contact interaction is [23]

$$\Gamma_{CI}\,(e^* \to ef\bar{f}) = \frac{1}{96\pi}N_C\,S\,\frac{m_{e^*}^5}{\Lambda^4}\,, \tag{3.18}$$

where N_C denotes number of light fermions, i. e. three. S is an additional combinatorial factor depending on f and f'

$$S' = \quad 1 \quad \text{for} \quad f \quad \neq f'\,, \tag{3.19}$$

$$S' = \quad 4/3 \quad \text{for} \quad f \quad = f' \quad \text{and quarks}\,, \tag{3.20}$$

$$S' = \quad 2 \quad \text{for} \quad f \quad = f' \quad \text{and leptons}\,. \tag{3.21}$$

This means, single production (via CI or GM) of an excited electron followed by the decay via CI produces a final state of at least two leptons, i. e. two

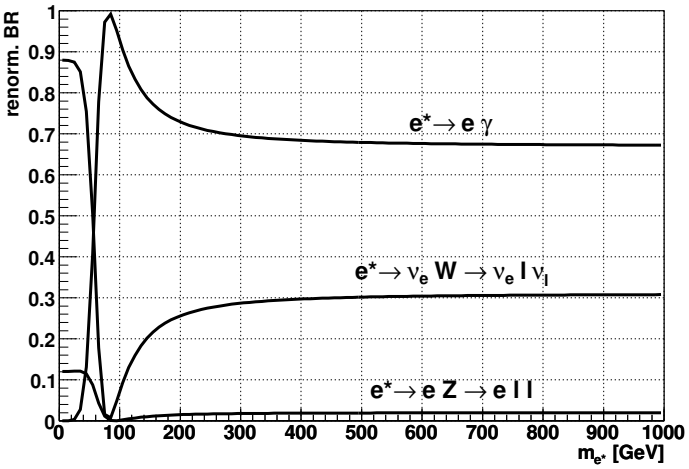

Figure 3.6.: Branching ratios for the different decay modes of excited electrons via gauge-meditated interaction. The branching ratios are renormalized for the leptonic decay into electrons and muons. The peak of the BR for $e^* \to e\gamma$ at the masses of the Z and the W-boson originates from the penultimate term in Eq. 3.13.

electrons, and two SM fermions. The latter ones can also be quarks which then would result in two jets. Such a final state ($ee + jet + jet$) is not as easy to analyze as the above mentioned $ee\gamma$ final state from decay via GM, since several SM processes with the same signature complicate a separation of the signal.

Comparing the BRs of the two interactions for different mass-to-Λ ratios in Fig. 3.7, one can see that for ratios larger than 0.3 the CI is clearly favored. However, even for very low BR, the decay via GM is experimentally easier to handle because of the easy to detect photon in the final state.

3.5. Recent Results

So far there is no discovery of an excited electron, nor of another excited lepton or quarks. Experimental limits were set of which the latest results are listed below:

- pair production of excited leptons ($l = e, \mu, \tau$) by the process ($e^+e^- \to l^*l^* \to l\gamma l\gamma$) by the OPAL collaboration [25]: $m_{l^*} > 103.2\,GeV$ with $\Lambda = 1\,\text{TeV}$ and both production and decay via GM.

- single production of excited electrons by the process ($q\bar{q} \to ee^* \to ee\gamma$) by the CDF collaboration [21]: $126\,\text{GeV} > m_{e^*} > 430\,\text{GeV}$ with $\Lambda = m_{e^*}$ and both production and decay via GM. For the production via CI and decay via GM the lower mass limit was set to 879 GeV.

  In both cases, only the analyzed interaction was considered, i. e. the branching fraction BF(GM) (see Fig. 3.7) was set to one.

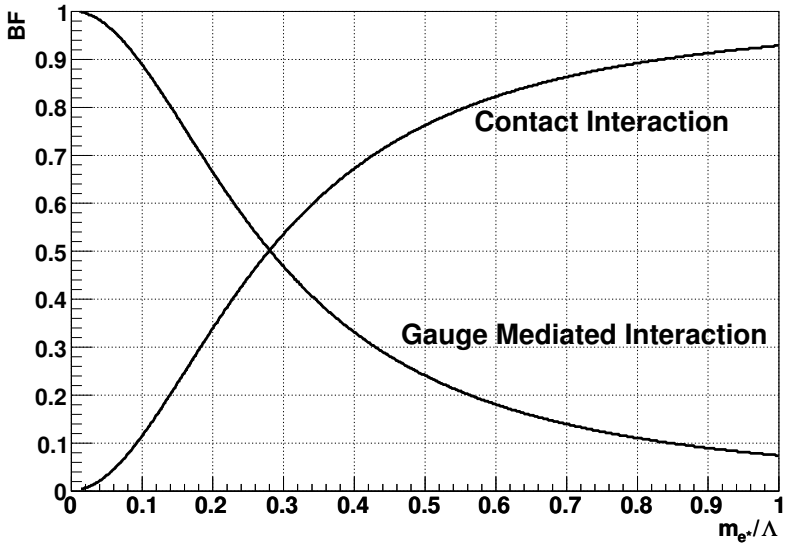

Figure 3.7.: Branching fraction for the decay of excited electrons via gauge-meditated (BF(GM)) and contact interaction (BF(CI))for different ratios of mass to compositeness scale.

- single production of excited muons by the process ($q\bar{q} \to \mu\mu^* \to \mu\mu\gamma$) by the DØ collaboration [20, 31]: $m_{\mu^*} > 618\,\text{GeV}$ (688 GeV) with $\Lambda = 1\,\text{TeV}$ ($\Lambda = m_{\mu^*}$) with production via CI and decay via GM.

For more details see the Particle Data Group listings [7] or the cited references therein.

4. Collider Physics

The theoretical issues were already introduced in the previous chapters. However, to understand and handle the data delivered by a detector some physical and mathematical tools are needed.

This chapter is supposed to explain the definition and the motivation of the quantities like for example the pseudo-rapidity. The terms luminosity and cross section are explained to confirm their importance for the description and the characterization of high energy physics. Also physical quantities that typically appear due to collisions of particles with a substructure, i. e. protons and anti-protons, are introduced briefly.

4.1. High Energy Physics Quantities

4.1.1. Natural Units

Particle physicists introduced the system of natural units. These allow an easy way to handle particle physics calculations.

The definition of natural units starts with setting two elementary quantities equal to one, the speed of light and Planck constant

$$c := 1 \qquad \text{and} \qquad \hbar := 1\,. \tag{4.1}$$

This yields that energy, mass, and momentum have the same unit, i. e. Electron-Volt (eV). Time and length have the inverse unit of energy (eV^{-1}). One eV is the energy of one electron, accelerated by an electrical field of 1 V.

4.1.2. Coordinates

To describe a phenomenon in a certain space one needs to define a coordinate system. In the case of the DØ experiment a cylinder coordinate system is used. Thus a particular point in the three dimensional space in the detector is uniquely characterized by

- z, its distance along the beam line from the nominal origin[1], the center of the detector,
- ϕ, its azimuthal angle measured counterclockwise beginning at the top, and
- θ, the opening angle respective the z axis.

[1] In the case of the Tevatron, positive z values denote the direction of motion of the proton.

Instead of θ the pseudo-rapidity

$$\eta := -\ln(\tan(\theta/2))\,, \tag{4.2}$$

is used, because it is invariant under Lorentz transformations along the beam line. The same is valid for ϕ, obviously. Tab. 4.1 shows the η values corresponding to those of θ. This makes life easier when transforming from the laboratory

η	0	1	2	3	4	5	6
$\theta\,[^\circ]$	90	40,4	15.4	5.7	2.1	0.8	0.3

Table 4.1.: Values of θ corresponding to η.

frame to the center-of-mass frame. There are two possibilities to determine η, respective the geometrical center of the detector and respective the interaction vertex. In this analysis the prior method is used.

In such a coordinate system the distance in the $\phi - \eta$ space of two objects is characterized by their separation

$$\Delta R = \sqrt{(\Delta\phi)^2 + (\Delta\eta)^2}\,. \tag{4.3}$$

Instead of the momentum p the transverse momentum

$$p_T = \sqrt{p_x^2 + p_y^2}\,, \tag{4.4}$$

is used more often. It is invariant under boosts along the beam line, too.

Since the initial particles in collisions are supposed to have a transverse momentum almost equal to zero[2], the same should be valid for the total of transverse momenta in one event, too. Otherwise a non-detectable particle, e. g. a neutrino, is supposed to have participated in the process. It is characterized by the missing transverse energy $\not{E}_T$.

4.1.3. Luminosity

One distinguishes between the instantaneous and the integrated luminosity. The instantaneous luminosity is is a quantity for the number of collisions in a certain area. The integration of the instantaneous luminosity over a certain time scale

$$\mathcal{L}_{int} = \int_{t_i}^{t_e} \mathcal{L}_{inst}\, dt\,, \tag{4.5}$$

is called integrated luminosity. It is a quantity for the amount of processes with a certain cross section recorded by the detector. The integrated luminosity is often called in high energy physics luminosity. This analysis adapted this nomenclature.

When assuming a Gaussian transverse beam profile for the bunches, the luminosity is approximately

$$\mathcal{L} = \frac{f\,B\,n_p\,n_{\bar{p}}}{4\pi\sigma_x\sigma_y}\,, \tag{4.6}$$

[2]The partons of protons may have a non-zero p_T of the particles.

where f is the revolution frequency of the B bunches of n_p protons and $n_{\bar{p}}$ anti-protons. σ_x and σ_y are the beam width in x and y-direction, respectively. Because a large probability is desired for hard processes, the collisions have to take place in an area as small as possible and with a high frequency.

The luminosity is given in units of $\mathrm{cm}^{-2}\mathrm{s}^{-1}$. Because it tends to be a large number, the luminosity is usually given in units of inverse barn[3], for example $1\,\mathrm{fb}^{-1} = 10^{39}\,\mathrm{cm}^{-2}$.

4.1.4. Center-of-mass Energy

Another important characterizing property of a particle accelerator is in addition to the instantaneous luminosity the center-of-mass energy $\sqrt{s}$. For two particles of masses m_1 and m_2 the center-of-mass energy can be written in the form

$$\sqrt{s} = \sqrt{(E_1 + E_2)^2 - (\mathbf{p}_1 + \mathbf{p}_2)^2}\,, \tag{4.7}$$

where $E_i = \sqrt{p_i^2 + m_i^4}$ and p_i is the momentum of the i-th particle. For a hadron collider like the Tevatron the situation is not that easy. Due to the substructure of protons, it is not known which particles scatter in a certain bunch crossing. To deal with this problem physicists use the Parton Density Functions (see Sec. 4.2).

4.1.5. Cross Section

The cross section of a process characterizes the probability of this particular process to happen.

To calculate the cross section for a process three quantities are necessary, the center-of-mass energy $\sqrt{s}$, the matrix element, and Lorentz invariant phase space [10]. The absolute squared matrix element $|\mathcal{M}|^2$ is a quantity to describe the transition from an initial to a final state. The Lorentz invariant phase space is obtained from the number of possible final states and a delta-function, to satisfy the energy and momentum conservation for the transition process

$$d\mathrm{Lips} = \delta^4(p_{f,1} + p_{f,2} - p_{i,1} - p_{i,2}) \cdot \frac{d^3p_{f,1}}{(2\pi)^3\, 2\, E_{f,1}} \cdot \frac{d^3p_{f,2}}{(2\pi)^3\, 2E_{f,2}}\,, \tag{4.8}$$

where $E_{f,1}$ is the energy and $p_{f,1}$ is the momentum of the first particle of the final state.

The differential cross section can be written as

$$d\sigma = \frac{1}{4s^2p} \cdot |\mathcal{M}|^2 \cdot dLips\,. \tag{4.9}$$

p is denotes the momentum of the center-of-mass system of the final state particles.

From Eq. 4.9, one can calculate differential cross sections for different quantities or the total cross section of a process.

[3] One barn is equal to $10^{-24}\,\mathrm{cm}^{-2}$.

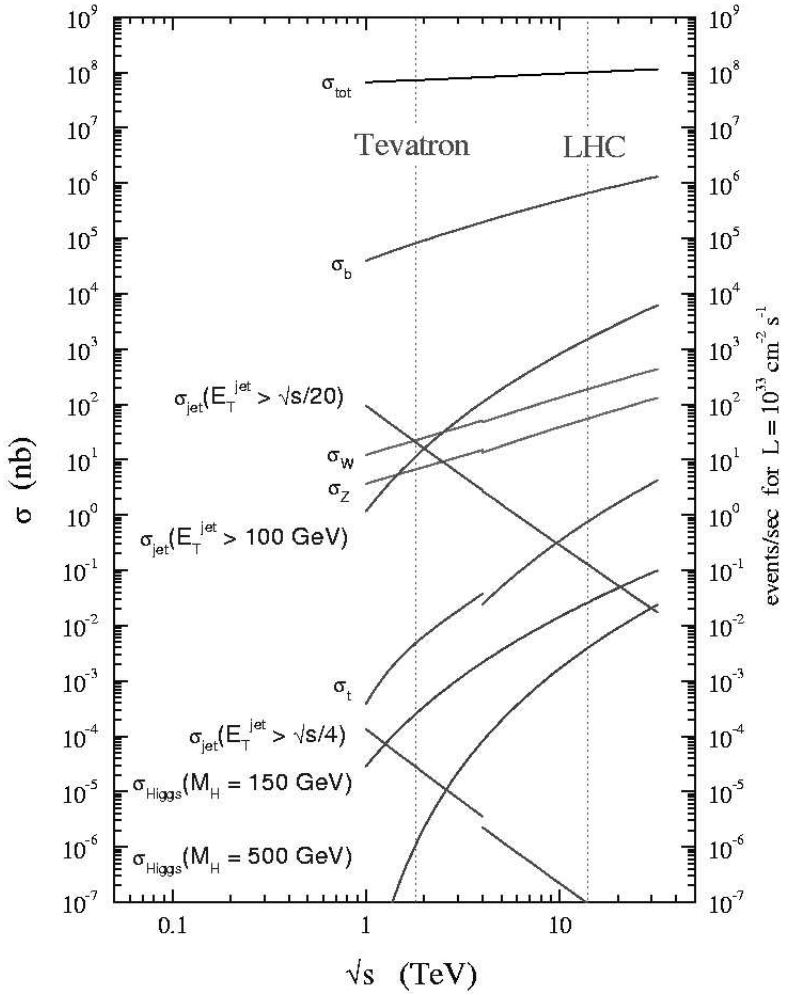

Figure 4.1.: Cross sections and event rate per second as a function of the center-of-mass energy for W, Z, b quark, and t quark production as well as QCD predictions, at the Tevatron and at the LHC [2].

Cross sections are given in the unit barn (see Sec. 4.1.3). In Fig. 4.1 the cross section of different processes at the Tevatron and the Large Hadron Collider (LHC) depending on the center-of-mass energy is shown. The gap between cross sections of some processes, e. g. the Z production, at the Tevatron and the LHC originates from the different initial particles[4] at the colliders.

Cross sections in leading order (LO) consider only tree-level[5] Feynman graphs. If terms are considered that are of one order higher in α_s than the LO, the cross section is determined of next-to-leading order (NLO). Higher corrections (NLO, NNLO) are applied to the leading order cross section with a so-called k-factor.

[4]Unlike the Tevatron, the LHC accelerates two protons. Thus, the probability for an anti-quark is lower.

[5]Feynman graphs without any loop or vertex correction term.

4.2. Proton Substructure

For hadron collider physics one has to leave behind the naive picture of a proton or anti-proton composed of two u and one d-quark, or $\bar{u}\bar{u}\bar{d}$, respectively. Instead a proton should be seen as a compound object of partons, i. e. valence quarks (uud) and sea-quarks, as well as of gluons. Furthermore not only gluon exchange between these quarks is a possible scenario. Also gluon splitting into a quark anti-quark pair inside a proton is realized as well as the processes $g \to gg$. Due to Heisenberg's uncertainty principle, all these particles can be generated for a certain, very small time scale, thus have a non-zero probability to participate in scattering process. The partons may have a transverse momentum different from zero.

Bjorken introduced the equation

$$k_{\mu,i} = x_i \cdot P^\mu \tag{4.10}$$

where $k_{\mu,i}$ is the i-th parton four-momentum and P^μ the four-momentum of the proton. x_i is called the Bjorken-x and gives the fraction of four-momentum carried by the i-th parton.

The parton density function (PDF) $f_i(x, Q^2)$ gives the probability for the parton i to carry the fraction x of the four-momentum of the proton. All fractions x have to add up to one, summed over all partons i

$$\sum_i \int dx\, x \cdot f_i(x, Q^2) = 1\,. \tag{4.11}$$

To predict the cross section for a partonic[6] subprocess $q_i q_j \to X$, one has to fold the partonic hard scatter cross section $\hat{\sigma}$ for this particular process with the PDF, such that

$$\frac{d\sigma_X(s, Q^2)}{dv_{kin}} = \sum_{i,j} \int dx_i dx_j\, f_i(x, Q^2)\, f_j(x, Q^2)\, \frac{d\hat{\sigma}^{ij}_X(x_i, x_j, Q^2)}{dv_{kin}}\,, \tag{4.12}$$

where $\sigma_X(\sqrt{s}, Q^2)$ is the cross section for the process $q_i q_j \to X$, v_{kin} a kinematic variable.

The theoretical QCD calculations, which are necessary to determine the PDFs, are very complicated. For example long-distance processes cannot be calculated in perturbation QCD. Thus, the PDFs are obtained by fits to experimentally measured structure functions and other observables. The structure function is defined as

$$F_2(x) = x \cdot \sum_i Q_i^2 \cdot f_i(x, Q^2)\,, \tag{4.13}$$

summed over all partons i. The structure function $F_2(x)$ is proportional to the structure function $F_1(x)$. The difference is made due to the anomalous magnetic moment of the proton (for more information see [9, 10]).

From measurements of $F_2(x)$ the Bjorken-x can be derived. This is performed for example at the Deutsches Elektron Synchrotron (DESY) ep Collider HERA[7] [32]. Fig. 4.2 illustrates the dependency of the structure function $F_2(x)$

[6] Keep in mind that here q_i denotes all SM quarks and also gluons.
[7] Hadron Elektron Ring Anlage

on the transverse momentum transfer Q^2. As shown, F_2 does not only depend

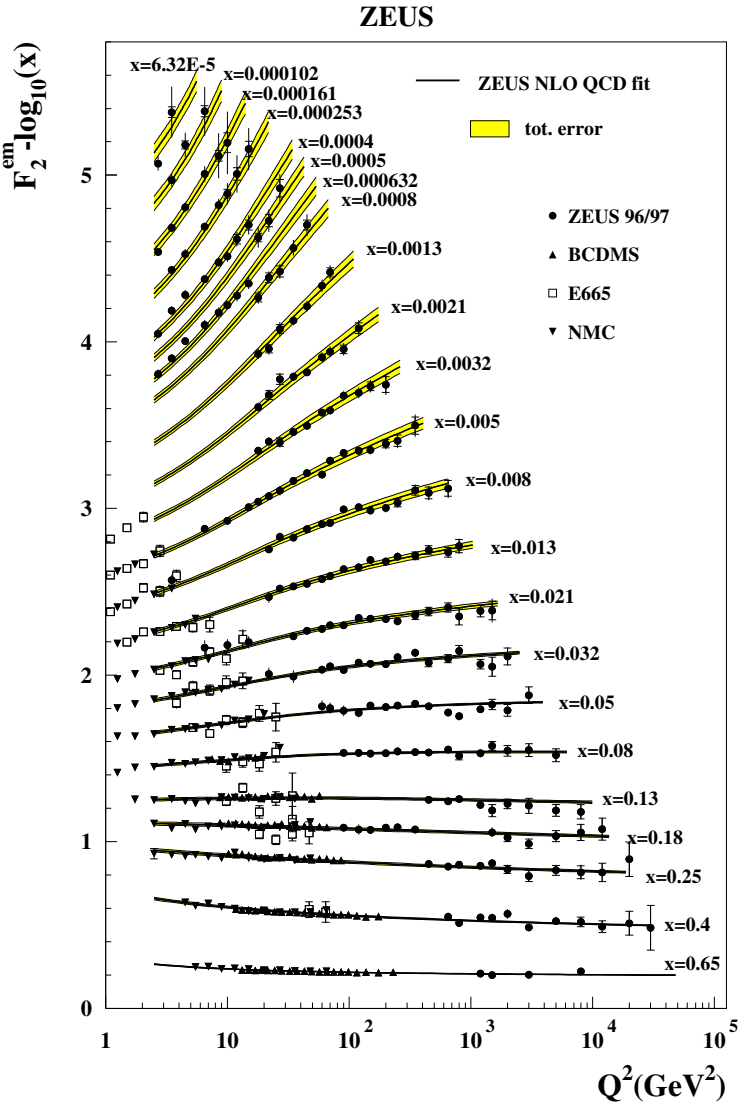

Figure 4.2.: The ZEUS-S NLO QCD fit for a proton fixed target. Here the PDF for the proton is denoted as F_2.

on x but also on the transverse momentum transfer Q^2. For high x values, $F_2(x)$ is nearly constant for different Q^2 values. Towards lower x the dependency on Q^2 increases, which is called "scaling violation".

Fig. 4.3 illustrates the results from ZEUS[8] NLO QCD fits for $Q^2 = 10\,\mathrm{GeV}^2$. Different parameterizations of the data are used, as for example CTEQ and MRST. Shown are also the distributions of CTEQ6M and MRST2001, both next-to-leading order [3]. One can see that at small x, the probability for

[8]Zearch to Elucidate Underlying Symmetry (ZEUS) is one of the experiments at DESY.

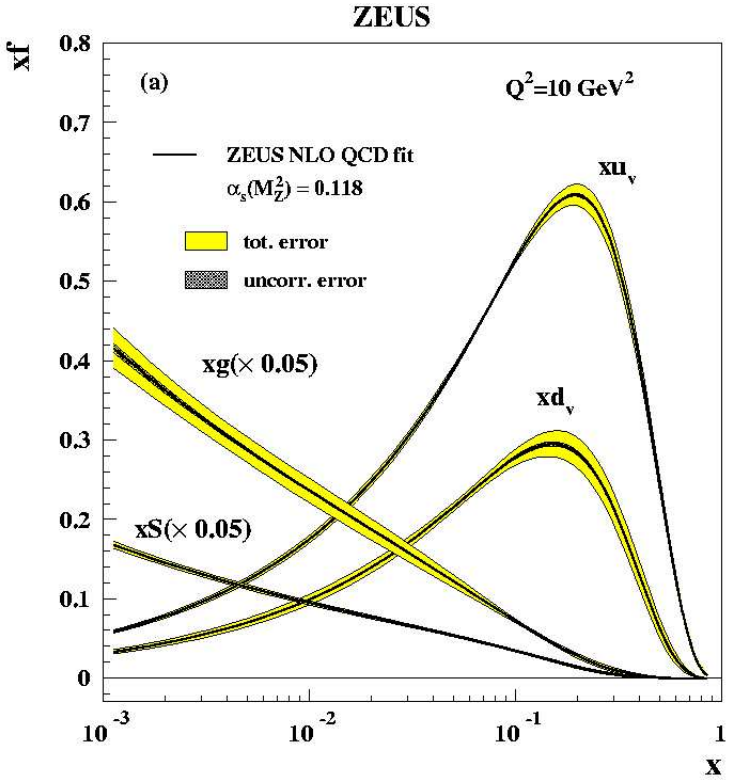

Figure 4.3.: The two PDF CTEQ6M and MRST2001 in comparison with ZEUS NLO QCD fits [3] at $Q^2 = 10\,\text{GeV}$. Shown is the fraction of the proton momentum times the PDF xf as a function of the momentum fraction x. xf is plotted for the valence quarks u_v and d_v, the gluon density g, and the sea quarks S.

valence quarks to participate in the hard scattering process is much lower than for sea quarks or gluons.

To fully describe events hadron colliders using Monte Carlo simulations (see Sec. 7.1), both the hard scatter cross section of the participating partons and the PDFs are required.

5. The Accelerator Complex and the DØ Experiment

The data used in this analysis was recorded by the DØ detector. The DØ experiment is situated at Fermilab. Its purpose is the measurement of proton anti-proton collisions at the interaction point D0. Both the proton and the anti-proton are accelerated by the Fermilab accelerator chain which is composed of several components, e. g. three different synchrotrons with the Tevatron as the largest.

Fermilab, named after the Nobel Price laureate Enrico Fermi, was founded in 1967. It is located about 60 km west of Chicago, Illinois (USA). The Fermilab Tevatron collider is with a center-of-mass energy of 1.96 TeV the particle collider with the highest energy currently running on earth.

Three important discoveries and a large amount of measurements that support the predictions of the SM were made at Fermilab. The first discovery was the bottom-quark [33] in 1977 and then followed in 1995 by the discovery of the top-quark [34, 35]. In the year 2000 the tau-neutrino as the third and last expected neutrino was directly observed [36].

The Tevatron is host of two experiments, DØ, named after interaction point, and CDF, Collider Detector at Fermilab. An aerial photo is shown in Fig. 5.1.

The data taking period between 1992 and 1996 is called Run I. Before starting Run II in 2001, the Tevatron collider as well as the experiments were upgraded, e. g. the center-of-mass energy was increased from 1.8 TeV to 1.96 TeV. In Run IIa (from March 2001 to February 2006) the DØ detector took about 1.2 fb^{-1} data.

In this chapter the accelerator chain of the Tevatron (Sec. 5.1) and the DØ detector (Sec. 5.2) are described.

5.1. The Tevatron Accelerator Chain

The accelerator chain consists of several components, schematically shown in Fig. 5.2 and described in more detail in [37, 38].

First H^- ions are produced via streaming of H_2 gas through free electrons. The ions then are accelerated to 750 keV in the Cockcroft Walton accelerator. During this step the ions are bunched. From this pre-accelerator the ions are induced into a 150 m long Linear Collider (Linac). There drift tubes accelerate the ions with oscillating electric fields to 400 MeV and launch them through a carbon foil. This filters the protons out of the H^- ions.

Figure 5.1.: Aerial photograph of Fermilab. The Main Injector is visible in the front. The Tevatron lies in the back [4].

Then the protons are injected in the booster, the first of the three synchrotrons. The protons are accelerated to 8 GeV. Because the radius of the booster is fixed with about 75 m, the protons are kept in their orbit by increasing the magnetic field. Protons are delivered by the booster in 84 bunches spaced by 18.9 ns and accelerated in the main injector, a synchrotron of 500 m radius, to 120 GeV.

A quite tricky business is the production of anti-protons. This is done by launching the proton beam delivered by the main injector every 1.5 s to a nickel target that acts as an anti-proton source. To produce one anti-proton about 10^5 protons are needed. The produced anti-protons are debunched and their energy increased to 8 GeV via stochastical cooling. The accumulator then collects the anti-proton bunches. The production rate of anti-protons decreases with the increasing of the number of anti-protons stored in the accumulator. To provide an efficiency as high as possible anti-protons from the accumulator are buffered in the recycler[1].

The anti-protons are not immediately accelerated in the main injector. First protons are delivered again to the Main Injector and from there into the Tevatron. Then the anti-protons are injected. Both the protons and the anti-protons are accelerated to about 150 GeV in the main injector.

In the Tevatron both the protons and the anti-protons are accelerated to 0.98 TeV clockwise and counterclockwise, respectively. The Tevatron has a circumference of 6.28 km. To keep the protons and anti-protons in their orbit a magnetic field of 4.2 T is provided. To obtain such a strong magnetic field

[1] The envisaged function of the recycler was to collect the anti-protons at the end of a store.

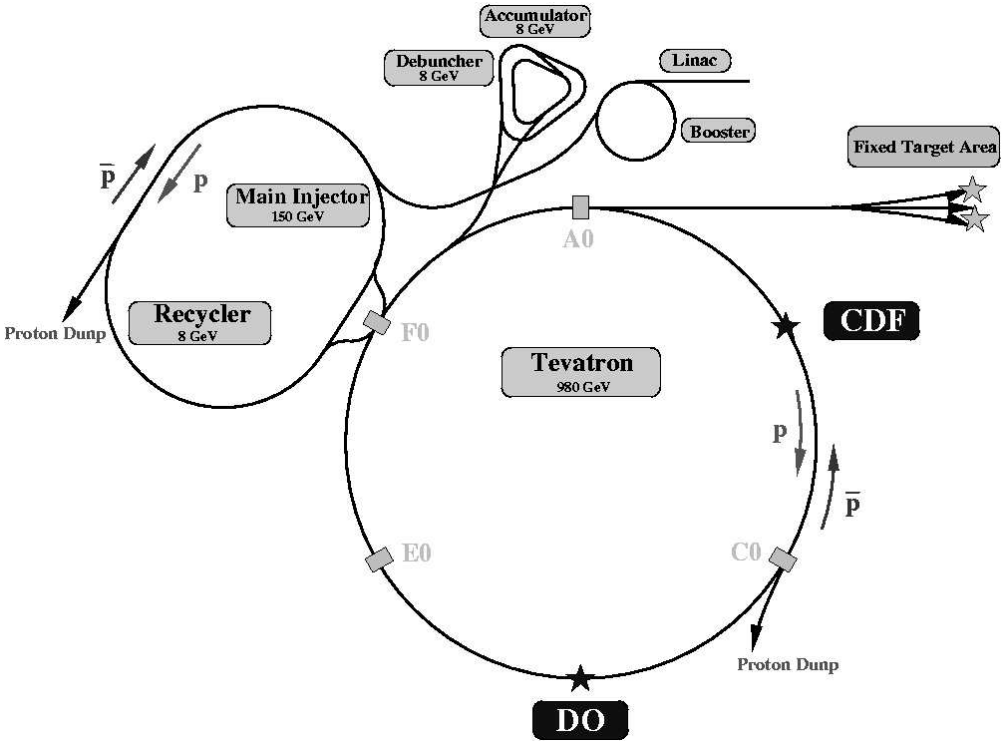

Figure 5.2.: The Tevatron accelerator Chain [5].

over 1000 superconducting dipole magnets were installed. All have to be cooled to 4.2 K by liquid helium. It was the first time that superconducting magnets were used at a synchrotron.

Both the protons and the anti-protons are injected to the Tevatron in 3 trains, each consisting of 12 bunches revolving with a frequency of about 47.7 kHz. The bunches collide at the two interaction points D0 and B0[2]. At the DØ interaction point the interaction rate per crossing is on average about 1.8. At the beginning of a store with for example an instantaneous luminosity of $5 \cdot 10^{31}\,\mathrm{cm}^{-1}\mathrm{s}^{-1}$ the rate would be 2.3.

Data measured with the DØ detector is recorded until the instantaneous luminosity is decreased to 1/3 of its initial value. This is called a store and lasts about 15 up to 20 hours. A store is subdivided into runs. One run lasts maximal 4 hours or ends if a modification of the luminosity parameters is necessary.

5.2. The DØ Detector

The design of the DØ detector was proposed in 1983 to analyze physics in $p\bar{p}$-collisions at high energies (1.8 TeV). The main interest was to study higher mass states and phenomena with large transverse momentum.

Constructed in the beginning of the 1990s the detector performed well during Run I from 1992 to 1996. After a shutdown and an upgrade of both the

[2]Location of the CDF experiment

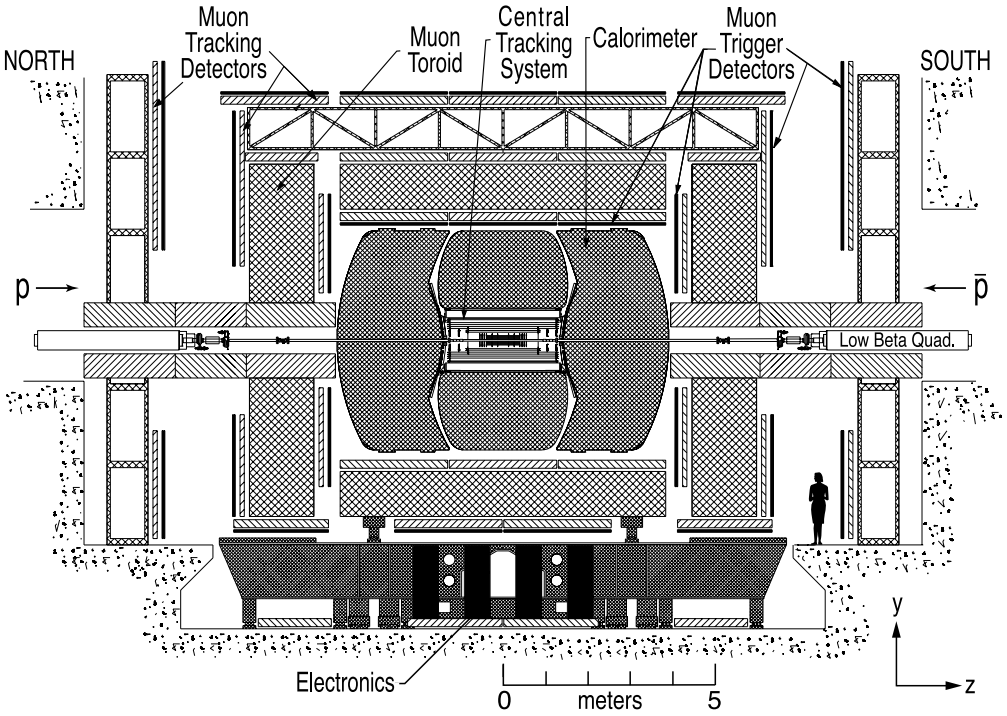

Figure 5.3.: The cross-sectional profile of the DØ detector viewed from inside the Tevatron Accelerator.

detector and the collider Run IIa started in March 2001.

In the beginning of 2006 again an upgrade was maintained. Run IIb just started at the end of July 2006.

As the data analyzed in this search is taken only during Run IIa the detector is discussed in its state during this particular data taking period. The original detector is described in [39].

The DØ detector was designed as a multi-purpose detector. It was supposed to be able to detect the final states of all known particles arising from high energy collisions and of possibly new particles, as for example excited states of SM fermions.

The detector consists of different subsystems mounted around the innermost point, the interaction point, to cover most of its surroundings. A schematic drawing of the DØ detector is shown in Fig. 5.3.

Starting at the interaction point, the detector consists of a tracker system, followed by a preshower detector. These are surrounded by a solenoidal magnet. The calorimeter is divided in the electromagnetic calorimeter and the hadronic calorimeter, where the latter consists of the Fine and the Coarse Hadronic Calorimeter. The outermost component, the muon system consists of an additional toroidal magnet. In the forward direction[3], next to the beam pipe, a forward proton detector as well as the luminosity monitor is installed. Three different stages of triggers are used to filter the large amount of data which

[3]The expression "forward direction" is used for regions with high $|\eta|$.

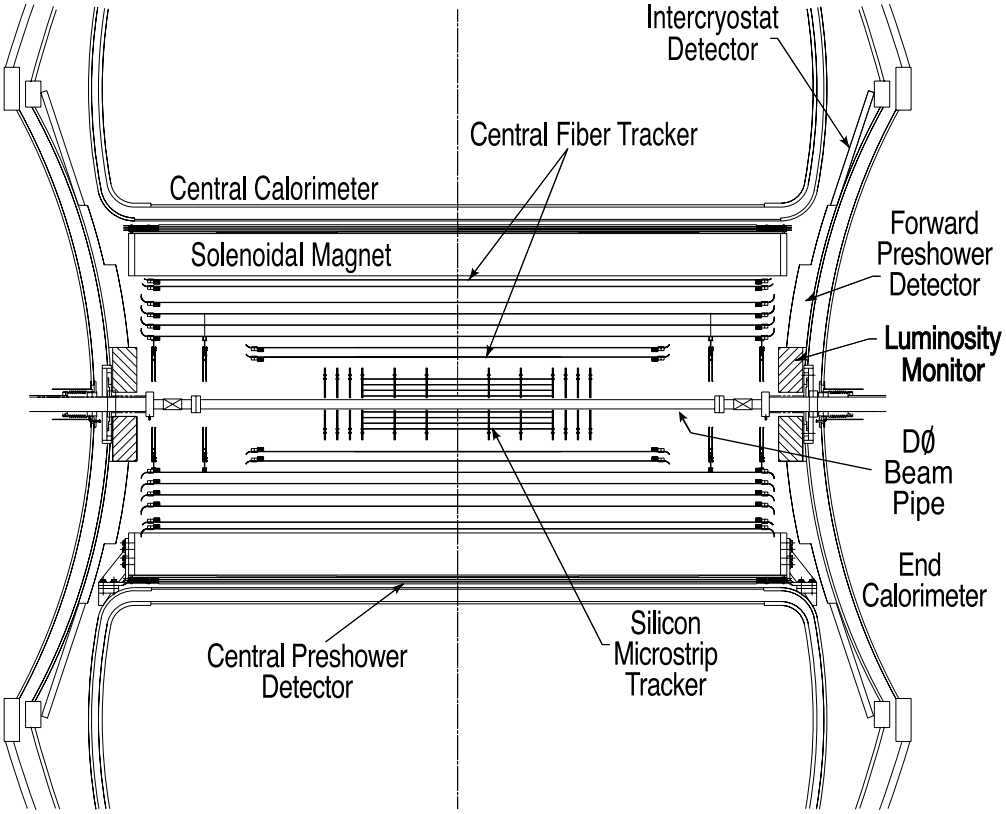

Figure 5.4.: The complete tracking system of the DØ detector with the silicon microstrip tracker, the central fiber tracker, and the solenoidal magnet.

appears in high energy collisions.

All components are explained in the following sections. Unless otherwise mentioned the information and figures are taken form [40].

During the shutdown before Run IIb a new component, the layer 0 was installed between the beam line and the tracking system. It is not discussed here.

5.2.1. Tracking System

The old tracking system was completely replaced for Run II due to higher requirements on radiation hardness with increasing instantaneous luminosity and the introduction of the solenoidal magnet. The new tracking system provides an excellent tracking in the central region of the detector. It is illustrated in Fig. 5.4.

It consists of two trackers, the silicon microstrip tracker (SMT) and the central fiber tracker (CFT). These are surrounded by a solenoidal magnet with a field strength of about 2 T (in the central region, $|z| \approx 0$).

The two trackers are able to measure the position of the primary interaction vertex along the beam pipe with a resolution of 35 μm.

5.2.1.1. Silicon Microstrip Tracker

The SMT (see Fig. 5.5) was constructed with regard to vertexing and tracking over the full coverage of the region covered by the calorimeter and the muonsystem. It was designed taking into account the length of the interaction region, which is about $\pm 30\,\mathrm{cm}$ along the beam line (see Sec. 5.2.6). This set the length scale for the SMT.

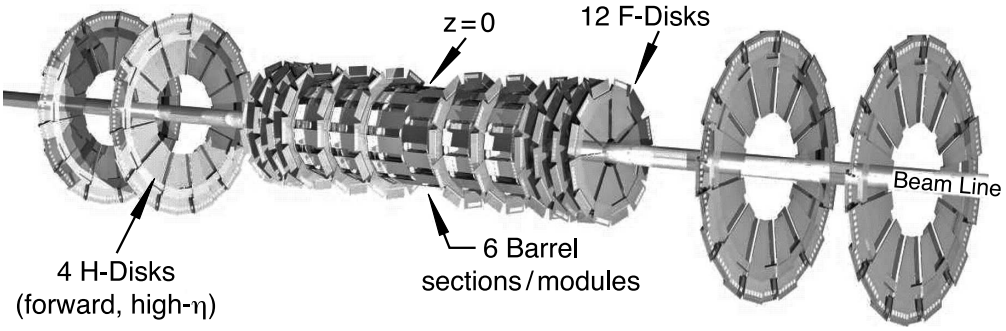

Figure 5.5.: The silicon microstrip tracker composed of disks and barrels along and around the beam line, respectively.

A structure of barrels and disk form the SMT. In the central region six barrels measure the $r-\phi$ component. These are subdivided by 12 disks, so-called F-Disks, for $r-z$ and $r-\phi$ measurement. In forward direction 4 bigger disk (H-Disks) provide a three dimensional determination of tracks at high $|\eta|$.

Four silicon readout layers are added to a barrel. Six of of those barrels surround the beam line. The two inner layers are built of 12 silicon modules, so-called ladders. Layer three and four consists of 24 of those silicon modules.

Every barrel is cabbed by a F-Disk at $|z| = 12.5, 25.3, 38.2\mathrm{cm}$. Six more F-Disks are located at $|z| = 43.1, 48.1, 53.1\mathrm{cm}$. A F-Disk is pieced together of twelve double-sided wedge-detectors.

In the far forward region ($|z| = 100.4, 121.0\mathrm{cm}$) the four H-disks were mounted to provide tracking at high $|\eta|$. The H-Disk have a larger diameter and are composed of 24 full wedges.

The temperature of the SMT is limited to reduce bulk damage to the silicon. Water (30% ethylene glycol mixture) supplied at $-10^\circ\,\mathrm{C}$ is the coolant. The SMT region is additionally chilled with dry air at $-40^\circ\,\mathrm{C}$.

In $r-\phi$ the SMT provides a resolution of about $10\,\mu\mathrm{m}$. Informations from the SMT are used for Level 2 and 3 triggers (see Sec. 5.2.7).

5.2.1.2. Central Fiber Tracker

The CFT (see Fig. 5.6) consists of scintillating fibers which are mounted on 8 concentric support cylinders made of carbon. It is located in the region from $r = 20\,\mathrm{cm}$ to $r = 52\,\mathrm{cm}$ around the beam line. The inner two cylinders support also the H-Disks of the SMT. The cylinders are loaded with two doublet layers of fiber. Two layers are located along the beam line and the outer two with a stereo angle of $\pm 3^\circ$.

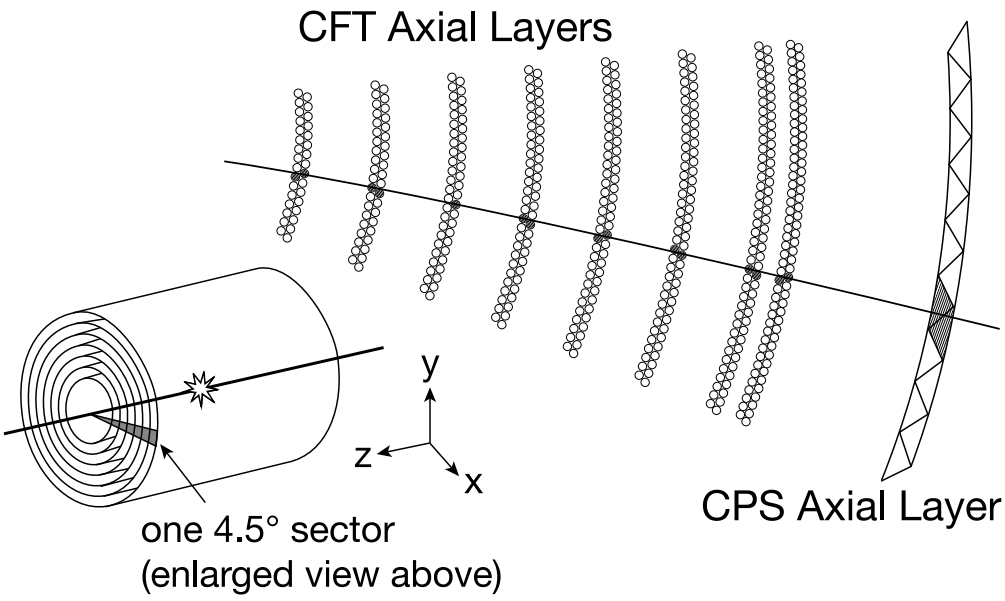

Figure 5.6.: The central fiber tracker with hypothetical track.

Coupled to waveguides the scintillating fibers lead the light to visible light photon counters (VLPC). Only one side of the fibers holds a readout. The counterpart is mirrored with a reflection of 90%. The VLPCs have a high quantum efficiency of about 75% when cooled to 9 K.

In contrast to the calorimeter (see Sec. 5.2.4) the trackers were constructed as thin as possible. Thus, the particles only depose an amount of their energy that just allows the measurement of the tracks. The thickness of the CFT and its support cylinder in radiation length X_0 is listed in Tab. 5.1.

Component	Radiation Length X_0
scintillating fibers	$2.8 \cdot 10^{-3}$
carbon fiber support cylinder	$3.2 \cdot 10^{-3}$
glue	$3.0 \cdot 10^{-3}$

Table 5.1.: Thickness of CFT components in radiation length.

Due to the small diameter of the fibers ($\varnothing = 835\,\mu$m) the resolution is about $100\,\mu$m.

The information of every fiber is supplied as input for level 1 trigger and is sent every 132 ns. Level 2 triggers use the complete track candidates and level 3 triggers the complete information provided by the CFT.

Together the SMT and the CFT have a transverse momentum resolution of

$$\frac{\Delta p_T}{p_T^2} = 0.002\,\mathrm{GeV}^{-1}$$

5.2.2. Solenoidal Magnet

This magnet was introduced for Run II to allow a momentum resolution of the momentum measurements in the tracker and the calorimeter. Its conception was constrained by the space inside the central calorimeter. A tracker volume as large as possible was considered, too.

The central magnet field amounts to 2 T which is equivalent to a stored energy of about 5.3 MJ. With a thickness of one radiation length the solenoidal magnet already causes for example photons to shower. This fact was the motivation for the preshower detector.

5.2.3. Preshower Detector

The preshower detector (PSD) was implemented to aid to identify electrons and photons as well as to reduce background rejection during triggering and offline reconstruction. It acts as both tracker and calorimeter. Also offline correction of energy measured by the calorimeter (see Sec. 5.2.4) can be corrected with PSD information.

The fast measurement of energy and position allows the use of PSD information for Level 1 Triggers.

5.2.4. Calorimeter

The calorimeter was designed to provide an energy measurement for electrons, photons, and jets in absence of a magnetic field. The calorimeter is the same as in Run I[4].

Also the identification of those objects as well as of muons is assisted by the calorimeter. The balance of the transversal energy is measured, too. This allows the reconstruction of events with involvement of non or very weakly interacting particles like neutrinos that cannot be measured in the detector.

As the tracker was supposed to be as thin as possible the calorimeter was constructed to force the showering of particles so their energy can be determined. This is provided by the active medium which is mainly liquid argon. The particles deposit all[5] their energy in the calorimeter. This happens due to showering, means the deceleration of electrons and photons due to bremsstrahlung and of hadrons due to inelastic scattering.

As Fig. 5.7 shows, the calorimeter is split into the central calorimeter (CC) and the end calorimeters (EC), the end calorimeter north (ECN) and end calorimeter south (ECS). All three are embedded in their own cryostat. The CC ranges to $|\eta| \approx 1.2$ and the EC up to $|\eta| \approx 4.0$. Both the CC and EC are divided into the electromagnetic section, the fine-hadronic, and the coarse-hadronic section.

A typical calorimeter cell consists of two metal absorber plates of depleted uranium and a signal board with a resistive surface. The absorber plate is grounded whereas the signal board is on positive high voltage of about 2 kV.

[4] The magnet was only implemented for Run II (Sec. 5.2.2)

[5] depending on the particle, e. g. muons do not

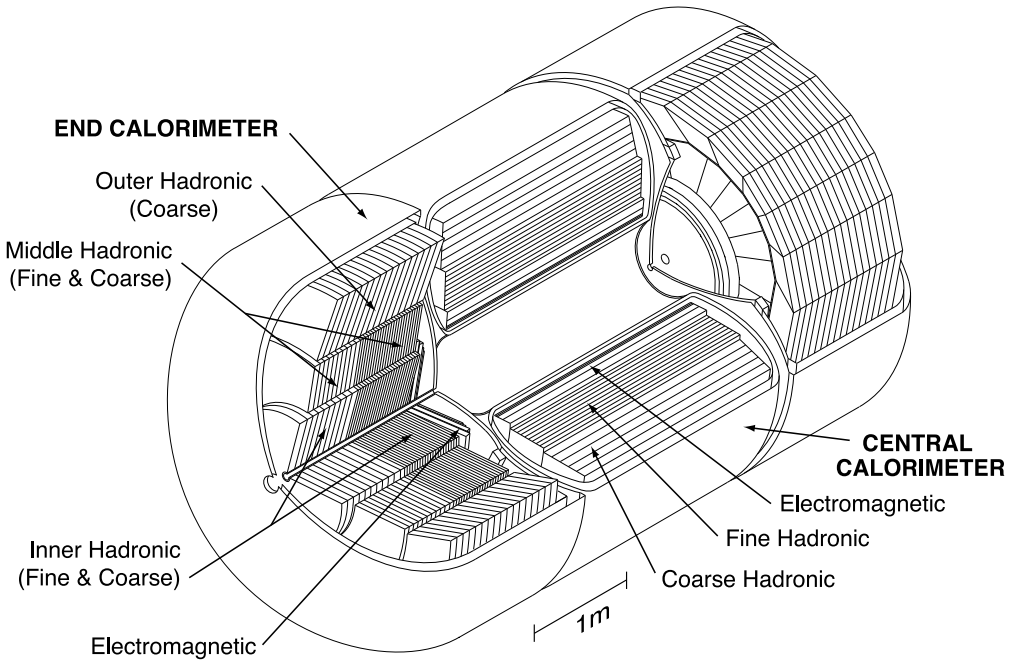

Figure 5.7.: The calorimeter of the DØ detector. Shown are the three cryostats and the layers of the electromagnetic, the fine and the coarse-hadronic calorimeter.

The acceleration versus the signal board supports the showering in the active medium. The drift time of electrons in the 2.3 mm liquid argon gap is about 450 ns.

The readout cells are combined to so-called towers of $\Delta\eta = 0.1$ and $\Delta\phi = {}^{2\pi}/_{64} \approx 0.1$. These towers are located at rays projected from the interaction point ($|z| = 0$) and are subdivided in depth.

The electromagnetic calorimeter consists of four depth layers, i. e. EM1, EM2, EM3, and EM4. The fine-hadronic calorimeter frames 3 depth in the CC and the coarse-hadronic calorimeter one. In the EC the fine hadronic calorimeter consists of 4 depth and the coarse-hadronic of again one. The thickness of the calorimeter components is listed in Tab. 5.2

The third layer of the electromagnetic calorimeter, i. e. EM3, is twice as fine in both η and ϕ. This choice was motivated by the fact that the shower

component	CC	EC
Electromagnetic Calorimeter	$1.4, 2.0, 6.8, 9.8\,\mathrm{X}_0$	$1.6, 2.6, 7.9, 9.3\,\mathrm{X}_0$
Fine-hadronic Calorimeter	$1.3, 1.0, 0.76\,\lambda_\mathrm{A}$	$1.1, 1.1, 1.1, 1.1\lambda_\mathrm{A}$
Coarse-hadronic Calorimeter	$3.2\,\lambda_\mathrm{A}$	$4.1\,\lambda_\mathrm{A}$

Table 5.2.: Thickness of the different calorimeter components in radiation length or absorption length for the electromagnetic calorimeter and the hadronic calorimeter, respectively.

maximum of electromagnetic objects is located in the region of the third layer. This allows a precise location of electromagnetic shower centroids in the case that no track was reconstructed.

The energy resolution of the calorimeter is calculated via

$$\left(\frac{\Delta E}{E}\right)^2 = C^2 + \frac{S^2}{E/\mathrm{GeV}} + \frac{N^2}{(E/\mathrm{GeV})^2} \tag{5.1}$$

The terms are called constant, sampling, and noise term, respectively. The constant term regards to systematical uncertainties for example caused by the calibration. It does not depend on the energy. The sampling term is based on statistics due to fluctuations of the energy deposition. It becomes smaller with increasing energy. The noise term originates from the calorimeter noise which can not be suppressed and uranium decays. It decreases quadratically with the energy. Tab. 5.3 shows the values for the resolution parameters for electrons [41].

resolution parameter	CC	EC
C	0.004	0.003
S	0.15	0.206
N	0.29	

Table 5.3.: The calorimeter energy resolution parameters.

Due to the incomplete coverage of the calorimeter of the $0.8 < |\eta| < 1.4$ region an additional detector, the so-called intercryostat detector (ICD), was introduced. The ICD consists of scintillating tiles. Also a single cell structure called massless gap is mounted between the two calorimeters. Both the ICD and the massless gap were not used in this analysis.

5.2.5. Muon System

The muon system was installed to provide a precise measurement of muons. The energy of muons can not be measured by the calorimeter, because they do not depose their complete energy in it. An additional magnetic field bends the trajectory of the muons in the muon system so their momenta and thus their energy can be measured independent of the tracker.

The central muon system includes proportional drift tubes, central scintillating counters, and the toroidal magnet and covers the region of $|\eta| < 1.0$. The toroidal magnet has an internal field of about 1.9 T. The forward muon system is settled up to $|\eta| \approx 2.0$ and consists of mini drift tubes and trigger scintillating counters. So-called cosmic cap and cosmic bottom were implemented to discriminate muons from cosmic radiation. Between the calorimeter and the toroidal magnet additional scintillating counters that form the Aϕ-Layer were mounted and act as a fast detector to reject out-of-time background.

This muon system as a stand-alone momentum measurement allows to enable a low-p_T cutoff in level 1 muon triggers, a cleaner matching with central

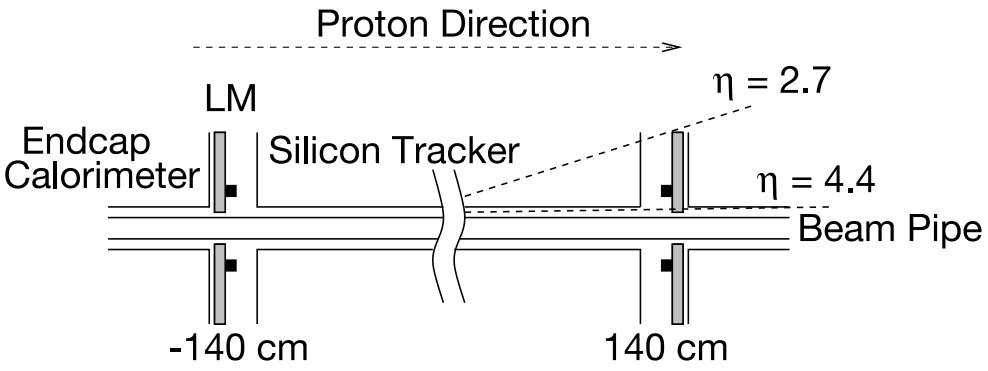

Figure 5.8.: The luminosity monitor (LM) is located in front of the EC, in forward direction.

detector tracks, to reject π/K decays, and to improve the momentum resolution for high momentum muons.

5.2.6. Luminosity Monitor

The aim of the luminosity monitor (LM) is the determination of the luminosity of the interactions at this experiment via detecting inelastic $p\bar{p}$-collisions. Its schematic drawing in Fig. 5.8 shows its location.

The LM consists of 24 plastic scintillation counters with eight PMT readouts. It is settled at $|z| = 140\,\text{cm}$ in front of the EC and covers the region of $2.7 < |\eta| < 4.4$.

The luminosity is calculated from the average number of inelastic collisions per beam crossing $\tilde{N}_{LM}$. Further the beam crossing frequency f and the effective cross section σ_{LM} is need. The latter includes the acceptance and the efficiency of the LM.

$$\mathcal{L} = f \frac{\tilde{N}_{LM}}{\sigma_{LM}} \tag{5.2}$$

With the aid of time-of-flight measurements it is possible to distinguish between $p\bar{p}$ interactions and beam halo backgrounds. This is accomplished by regarding only interactions with $|z| < 100\,\text{cm}$. Those measurements deliver the interaction region for most of the collisions at $|z| < 30\,\text{cm}$.

The luminosity is associated with triggers. The triggers are grouped together such that they have a common source dead-time, which means a common source of enabled, disabled, and readout. Thus the luminosity includes instantaneous luminosity[6], common trigger dead-time, and losses in the data acquisition system.

The fundamental unit is the luminosity block (LB). Every LB is characterized by a unique luminosity block number (LBN). The LBNs are incremented

[6]possible interactions per time unit

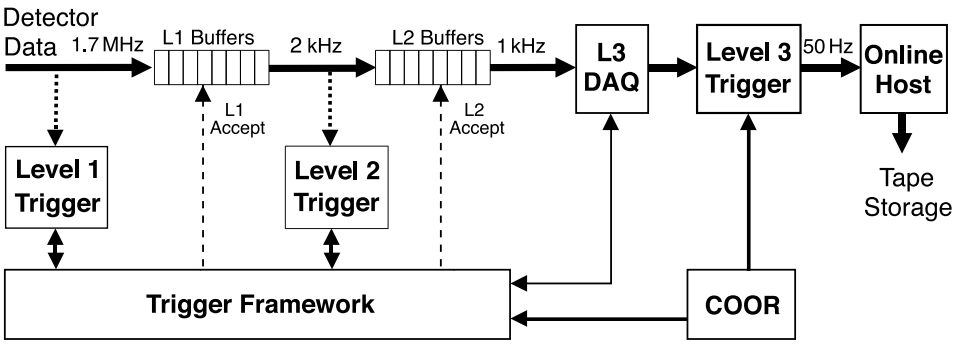

Figure 5.9.: The trigger and data acquisition systems of the DØ detector.

upon run or store transition[7]. The luminosity is calculated independently for each LB and is averaged over each LB.

5.2.7. Triggers and Luminosity Calculation

To distinguish desired events from background, triggers are used. The trigger system is formed of level 1 (L1), level 2 (L2), and level 3 (L3) triggers. A schematical drawing of the trigger system demonstrates Fig. 5.9.

The L1 trigger represent the first stage of filtering data and is a collection of hardware trigger elements. The acceptance rate is 2 kHz. The readout of L1 every 3.5 μs is limited by readout of the participating subsystems. All events awaiting the L1 decision are pipelined. For example the signals from the calorimeter are kept for 4 μs until a level 1 trigger has fired and 2 ms more for a level 2 triggering. This minimizes the dead-time.

The second stage are L2 triggers. It is a combination of hardware engines and microprocessors associated with specific sub-detectors. With a rate of 1 kHz it provides information to the global processor. Also trigger decisions by objects as well as by object correlations across all detector subsystems are made. The L2 triggers form physics objects from information provided by L1 and front-ends. Only events that pass a L2 trigger are tagged for full readout and L3 trigger analysis.

L3 Triggers are high level, fully programmable software triggers and build the third stage. Information is only supplied to L3 triggers when successfully triggered by L1 and L2. If triggered on L1 and L2 the information is processed by the L3 microprocessor farm. There sophisticated algorithms are applied that deliver events with a rate of about 50 Hz. The rate is restricted by the computing and the data storage capabilities. Every decision made by L3 triggers is based on complete physics objects.

The so-called trigger framework (TFW) gathers the information of L1 triggers and decides whether an event is to be accepted for further examination. It coordinates vetoes, the prescaling, and coordinates triggers and readout functions. To assure a maximum rate of about 50 Hz for information delivered from

[7] at least every 60 s

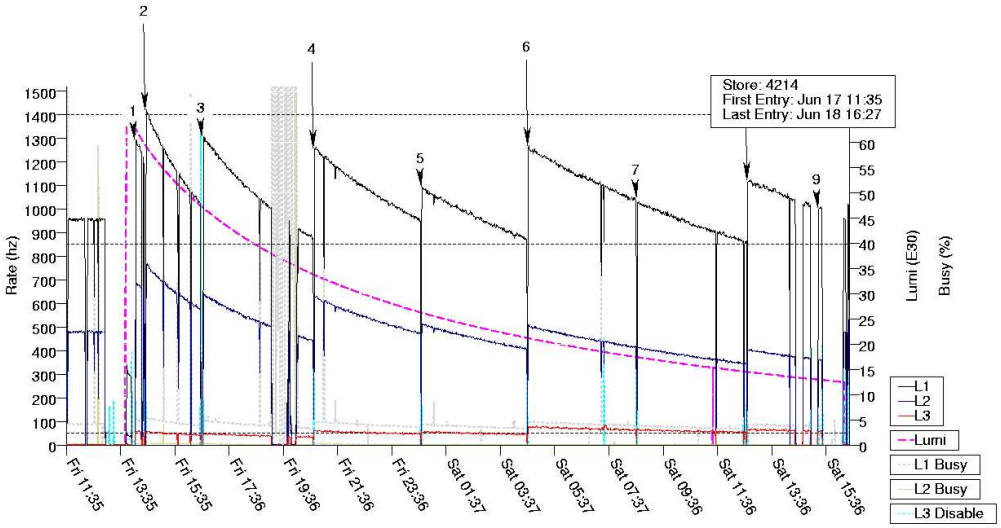

Figure 5.10.: Store 4214 statistics for the three trigger levels. The right ordinate shows the luminosity and the left the output rate of the triggers [6].

L3 a prescaling is applied on special L1 triggers. The prescaling factors vary and are managed by the TFW. Also a lot of scalers are provided. These allow accounting of trigger rates and dead-times.

Fig. 5.10 shows the trigger rates for one store (4214). This store contains 9 runs, from run number 207569 to 207578. The left axis shows the rate of the trigger output. For the L3 trigger the rate is maximal about 50 Hz as required. On the right axis, the instantaneous luminosity is shown, which decreases during the store from 65 to $13 \cdot 10^{30}\,\mathrm{cm}^{-2}\mathrm{s}^{-1}$.

The triggers used in this analysis are listed in Tab. 5.4. These are single-electron and di-electron triggers from the trigger versions v 8.2 to v 14, respectively, the time when the data was recorded. The version denotes the configuration of a trigger for a certain run period. All triggers are or-ed, that means at least one trigger had to fire to accept an event.

To select as many events as possible and thus to have an efficiency as large as possible, a large number of triggers is chosen. However, the information of three triggers is of substantial interest, because they are used for the luminosity calculation (see below).

- EM_MX : L1: One trigger tower[8] in the electromagnetic calorimeter with a transverse energy $E_T > 15\,\mathrm{GeV}$. L2: none. L3: An electron has to be reconstructed in the region $|\eta| < 3$ with $E_T > 30\,\mathrm{GeV}$.

- E1_SH30 : L1: One trigger tower in the electromagnetic calorimeter with $E_T > 11\,GeV$. L2: A single tower EMO[9] that is isolated ($iso < 0.2$ and has $E_T > 11\,\mathrm{GeV}$. L3: An electron with $E_T > 30\,\mathrm{GeV}$ has to be reconstructed.

[8]The difference between calorimeter and trigger tower in the electromagnetic calorimeter is the segmentation. A trigger towers has $\Delta\eta \times \Delta\phi = 0.2 \times 0.2$.

[9]Electromagnetical object, see Sec. 6.2

Trigger Version	Triggers
v 8.2 – v 11	EM_MX EM_MX_SH EM_HI_SH EM_HI 2EM_HI 2EM_HI_SH EM_MX_EMFR8 EM_HI_EMFR8 2EM_2MD7 2EM_2MD12 2EM_MD12_CEM10
v 12	E1_SHT20 E2_SHT20 E3_SHT20 E1_SH30 E2_SH30 E3_SH30 E1_L50 E1_VL70 E1_2SH8 E2_2SH8 E3_2SH8 E1_2L15_SH15 E1_2L15_SH15 E1_2L15_SH15
v 13	E1_SHT22 E2_SHT22 E3_SHT22 E4_SHT22 E1_2L20 E2_2L20 E3_2L20 E4_2L20 E1_SHT20 E2_SHT20 E3_SHT20 E4_SHT20 E1_SH30 E2_SH30 E3_SH30 E4_SH30 E1_L50 E1_NC90 E1_L70 E1_2SH8 E2_2SH8 E3_2SH8 E4_2SH8 E20_2SH8 E21_2SH8 E22_2SH8 E23_2SH8 E24_2SH8 E25_2SH8 E20_2L20 E21_2L20 E22_2L20 E23_2L20 E24_2L20 E25_2L20
v 14	E1_SHT25 E3_SHT25 E4_SHT25 E1_SH35 E3_SH35 E4_SH35 E1_L70 E1_2L15_SH15_L20 E2_2L15_SH15_L20 E3_2L15_SH15_L20 E4_2L15_SH15_L20 E5_2L15_SH15_L20 E6_2L15_SH15_L20 E1_2L20_L25 E2_2L20_L25 E3_2L20_L25 E4_2L20_L25 E5_2L20_L25 E6_2L20_L25

Table 5.4.: The single electron and di-electron triggers from version v 8.2 to v 14 that are used for this search. The denotation is explained in detail in [8].

- E1_SH35 : Like E1_SH30, only with L1 condition $E_T > 12\,\text{GeV}$ and L3 condition $E_T > 35\,\text{GeV}$.

For more details of the denotation see in [8].

The integrated luminosity is calculated for the period of data taking and the triggers listed in Tab. 5.4. As mentioned before, some triggers are prescaled to guarantee the maximal data delivering frequency of 50 Hz from L3 triggers. Only un-prescaled triggers are used to determine the luminosity. That means, the calculation is performed for one un-prescaled trigger that was fully functional and enabled during data recording period.

The information provided from the data quality group is also considered for the calculation [42]. The tool for the calculation is explained in [43]. Its output is shown in Tab. 5.5.

However, the luminosity has to be corrected due to several changes of system devices, that were not considered yet [44]:

- The central magnetic field strength was changed following a reduction of the current from 4750 to 4550 A.

- A pedestal shift of the summed LM signal occurred.

Trigger	Trigger version	Luminosity [fb^{-1}]
v8.0	EM_MX	5.60 ± 0.35
v9.0	EM_MX	23.91 ± 1.51
v10.0	EM_MX	10.35 ± 0.65
v11.0	EM_MX	62.84 ± 3.96
v12.0	E1_SH30	221.25 ± 13.94
v13.0	E1_SH30	52.32 ± 3.30
v13.3	E1_SH30	317.96 ± 20.03
v14.0	E1_SH35	302.32 ± 19.05
Sum		996.56 ± 62.78

Table 5.5.: Luminosity calculated for every trigger version with respect to one un-prescaled trigger. The correction factor is considered.

- Switch from NIM to VME electronics[10].
- Necessary correction for dead-time in the NIM.
- Replacement of the LM scintillators and reduction of the preamp noise.

This leads to a global correction factor for the luminosity of 1.151.

Also the inefficiency of rejecting events flagged by the data quality group has to be considered. Thus, a decrease of $3.2 \pm 1.0\%$ was included [45]. Both corrections are applied in Tab. 5.5. A total of $996.56 \pm 62.78\,fb^{-1}$ was analyzed in this work.

[10]NIM and VME are bus standards, where NIM is the older one.

6. Data Acquisition and Particle Identification

To analyze the data recorded by the detector one does not use directly the raw data delivered from the single detector components. The amount of information would be too big and only a fraction of it is used in the analysis. Rather reconstructed physical objects are handled. For every event in addition, important information is provided that is not specifically connected to a physical object.

The steps of acquiring data delivered from the detector as well as the identification of the physics objects are explained in this chapter.

6.1. Data Acquisition

As explained in Sec. 5.2.7, L1 and L2 triggers decide whether an event is going to be reconstructed by L3 triggers or not. If so, L3 triggers reconstruct the complete physical objects.

Via global monitoring, the data, and thus also the detector, can be controlled on-line. Events are tagged to contain events of physical reasonable processes or noise events. The data quality group [42] provides tools to check the events for these tags offline, during the actual analysis. These tags are also taken in account for the determination of the luminosity (see Sec. 5.2.7). Decisions made by data quality group are based on global monitoring information.

If at least one L3 trigger fired, the data of the event is completely reconstructed on the farms [46] and then written in thumbnail format (tmb) on tape, compressed by factor of 10. This data is distributed by sequential data access via meta-data (SAM) [47]. This system provides the reconstructed event information directly to physicists, selected by, for example, trigger information, event variables, e. g. noise and run number, and physical objects, e. g. EMobjects[1], muons, jets.

The data is also available in the Common Analysis Format (CAF), see [48], which has the form of ROOT trees [49]. It is an object orientated analysis framework that provides the use of commonly utilized tools in a standardized way as well as processors programmed by the users. CAF was used in this analysis to receive the information for further applications.

[1] CAF internal notation for electromagnetic objects, i. e. electrons and photons

6.2. Identification of Physical Objects

The different physical objects have to be distinguished. This is described here only for electromagnetic objects (EMOs), i. e. electrons and photons, because no other objects are required for this search.

The actual identification occurs by evaluating the information delivered by the electromagnetic calorimeter. To distinguish between electrons and photons tracker information is required. For more details see [50].

EMOs depose their energy due to showering in clusters in the electromagnetic calorimeter. The position of such clusters is determined by the "simple cone algorithm" for an cone radius

$$R = \sqrt{\phi^2 + \eta^2} < 0.4 \tag{6.1}$$

This means, the width of the cluster in the $\phi - \eta$ space should not exceed 0.4. The transverse fraction of the energy deposed in such a cone has to exceed 1.5 GeV for EMOs.

Also for jet reconstruction a cone algorithm is used with a cone radius $R_{Jet} < 0.5$. Hence, additional quantities have to be considered to identify EMOs. The combinations, the values and the efficiency of theses quantities are certified by the EM group [51, 52]. This will be discussed in more detail in Ch. 8.

6.2.1. Electromagnetic Fraction

One more criterion to distinguish between signals from jets and from EMOs is the electromagnetic fraction (emfrac) of the energy depositions in the calorimeter

$$emfrac = \frac{E_{0.4}^{EMCal}}{E_{0.4}^{Cal}} > 0.9 \tag{6.2}$$

The fraction of the total energy deposed in a cone of $R < 0.4$ in the electromagnetic part of the calorimeter has to be more than 90% of the energy deposed in the whole calorimeter, i. e. the electromagnetic and the hadronic calorimeter.

6.2.2. Isolation

An EMOs is called isolated (iso) if

$$iso = \frac{E_{0.4}^{Cal} - E_{0.2}^{EMCal}}{E_{0.2}^{EMCal}} < 0.15 \tag{6.3}$$

$$\Leftrightarrow \quad \frac{E_{0.2}^{EMCal}}{E_{0.4}^{Cal}} > 0.869 \tag{6.4}$$

That means, more than 86% of the energy in the calorimeter inside a cone of $\Delta R = 0.4$ has to be located inside a cone of $\Delta R = 0.2$ in the electromagnetic calorimeter. Jets have a smaller fraction and would thus not pass the isolation request.

6.2.3. Shower Shape

Another quantity is the shape of these electromagnetic showers. To characterize the shower shape, the χ^2 of a 8×8 covariance matrix, the H-matrix (HMx), is calculated. χ^2 does not follow a true χ^2-distribution. Thus, the values for the HMx are chosen to optimize background versus efficiency [50].

The eight correlated variables in the HMx are the energy fractions of the four layers of the electromagnetic calorimeter, the total energy of the EMO, the $|z|$-position of the associated vertex and the transverse shower width in $\phi - z$. The matrix is compared to the values obtained from Monte Carlo studies. This H-matrix is called HMx8 and is used for EMO in the EC.

For objects in the central region only a matrix of 7 correlated variables is used, i. e. the HMx8 without the transverse shower shape. It is called HMx7.

6.2.4. Track Matching

Up to this point electrons and photons can not be distinguished, thus are treated as electromagnetically interacting objects with the same calorimeter reconstruction (emfrac, iso, H-matrix). Both show almost the same behavior in the calorimeter. To distinguish between them a track is requested for electrons and a track veto has to be fulfilled for photons. Because a photon does not carry an electromagnetic charge (see Tab. 2.2), it only hardly interacts[2] with the tracker material (see Sec. 5.2.1). Thus no track can be associated to a photon.

Two different track matching algorithms are provided. In both cases the track matching is determined by a χ^2 probability

$$Prob\,(\chi^2_{trk}) > 0.01 \tag{6.5}$$

where the two probabilities are given by

$$\chi^2_{trk} = \left(\frac{\delta\phi}{\sigma_\phi}\right)^2 + \left(\frac{\delta z}{\sigma_z}\right)^2 + \left(\frac{E_T/p_T - 1}{\sigma_{E/p}}\right) \tag{6.6}$$

$$\chi^2_{spatialtrk} = \left(\frac{\delta\phi}{\sigma_\phi}\right)^2 + \left(\frac{\delta z}{\sigma_z}\right)^2 \tag{6.7}$$

In Eq. 6.6, the distance in ϕ between the extrapolated track from the third layer of the electromagnetic calorimeter and the cluster position is $\delta\phi$. The difference between the two vertex position calculations, from the track and from the cluster, is described by δz. σ_ϕ, σ_z, and $\sigma_{E/p}$ are the root-mean-squares of the experimental distributions of the quantities ϕ, z and E/p [53], respectively. In the last term, E_T/p_T is the ratio of the transverse energy deposited in the electromagnetic calorimeter and the transverse momentum from the track measurement.

The second possibility is the so-called spatial-track-match (Eq. 6.7). Here only the spatial distances are considered. The spatial-track-match is used in

[2] for example photon conversion $\gamma \to ee$

this analysis. This is motivated by the fact that the transverse momentum resolution of the tracker is not well understood. However, for high transverse momenta the fraction E/p becomes almost one. Thus, the last term in Eq. 6.6 becomes negligible.

7. Simulation of Physics Processes

Physicists try to validate their complex models of nature using Monte Carlo simulation techniques.

In this chapter a brief explanation of the generation of simulated events at the DØ experiment (Sec. 7.1) is given.

SM processes are introduced (Sec. 7.3) that yield the same final state like the signal signature, i. e. $ee\gamma$. These processes are called background processes (BG). Information like cross sections and number of generated events are presented for background processes as well as for the generated signal processes (the latter in Sec. 7.4).

7.1. Physics Event Generation

Two different event generators were used to produce the Monte Carlo events (MCs) for the signal and the SM background for this search, PYTHIA and COMPHEP.

7.1.1. PYTHIA

The concept of PYTHIA is the generation of high energy physics events based on analytical results and QCD-based models [29]. It allows the simulation of collisions of two particles like for example a proton-anti-proton pair, an electron-positron pair, as well as a proton and an electron. Considered are hard and soft interactions, parton distributions, initial and final state parton showers, multiple interactions, fragmentation and decay.

PYTHIA offers a large amount of SM processes as well as supersymmetric processes, technicolor, fourth-generation fermions and compositeness.

Extensive information is provided to the user, as well as full user control of the process. PYTHIA also acts as an extension for other event generators, e. g. to provide the fragmentation.

PYTHIA version 6.313 [29] was used for the signal production. The applied PDF was CTEQ6L1 [54, 55].

7.1.2. COMPHEP and LANHEP

Since in PYTHIA only the production of excited electrons via CI was implemented, COMPHEP was used to generate events through GM (see Ch. 3). COMPHEP was conceived to calculate cross section in the lowest order of perturba-

tion theory directly from a known Lagrangian[1], but was extended to offer also event generation [30, 56].

The Feynman rules, which have to be implemented in CompHEP, were generated with LanHEP [57]. LanHEP was conceived to compile Feynman rules in momentum representation especially for the use in CompHEP. The Lagrangian is written in LanHEP (version 2.0.7), e. g. Eq. 3.6.

This was performed for the production of excited electrons via GM (see App. A.1). The resulting Feynman rules were used in CompHEP (version 41.10) to generate events for GM production, containing an excited and a SM electron (see App. A.2).

Pythia can be used to decay the excited electron, generated by CompHEP, and to accomplish the hadronization for the events. However, this was not applied in this search[2].

7.2. DØ Detector Simulation

The physics event generators deliver events seen by a perfect observer. In the case of real detectors various factors yield an imperfect detection and thus imperfect reconstruction of an event. First of all, the detector has only a certain resolution. Another factor is the response of particles to the detector components. For example neutrinos can not be detected by the DØ detector. Also pions are difficult to separate from EMOs because they decay similarly.

The detector is simulated, in other words the behavior of the detector components in occurrence of such an event is simulated. This is the purpose of the DØ GEANT simulation of the total apparatus response (D0gstar) [58]. Only triggers are not simulated. Thus trigger efficiencies have to be measured and MC events corrected, respectively.

The electrical response of the DØ detector is simulated by D0sim [59] which uses the output from D0gstar. It simulates for example noise of the calorimeter, the SMT, and the muon system. Also calorimeter pileup from previous crossings is simulated with zero bias events. These take the interaction rate per bunch crossing into account (see 5.1).

The D0reco program reconstructs the data, either simulated or reconstructed by the detector.

The signal Monte Carlo events for the production via CI were produced with the DØ RunII release version p17.09.06. For the SM background, Monte Carlo events were produce with p17.06.02 (Drell-Yan) and p17.09.01 (WW incl., ZZ incl., WZ incl.).

7.3. Standard Model Background Processes

Since the signal signature is not the only process with the final state $ee\gamma$, also processes realized in the SM can contribute. Hence, all these processes have to be considered when the data is analyzed for signal events.

[1] More precisely, from known Feynman rules.

[2] Due to a lack of time.

One distinguishes between physics backgrounds with genuine $ee\gamma$ final states and instrumental backgrounds, in which at least one object is misidentified or missed.

Relevant background processes are elucidated in the following sections. The background events were simulated with PYTHIA (see Sec. 7.1).

7.3.1. Z/γ^* Drell-Yan channel

The main contribution is expected to come from the Drell-Yan process. A quark and an anti-quark annihilate into a virtual boson, i. e a photon or a Z-boson, which then decays into an electron-positron pair. An additional photon

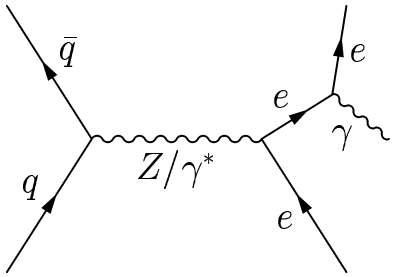

Figure 7.1.: Feynman graph of a Z-boson decay to an electron anti-electron pair with bremsstrahlung.

may result from initial state radiation (ISR) or final state radiation (FSR). That means one of the incoming partons (ISR) or the outgoing electrons (FSR) emits a photon, in the latter case due to bremsstrahlung. The Feynman graph for FSR is shown in Fig. 7.1.

In Tab. 7.1 the LO cross sections σ_{LO} are listed for $Z/\gamma^* \rightarrow ee$ for different invariant masses of the boson. The given cross sections include the BR for the

Boson mass [GeV]	$\sigma_{LO} \times BR$ [pb]	# events
$15 - 60$	336	313250
$60 - 130$	181	417500
$130 - 250$	1.37	207000
$250 - 500$	0.115	52750
> 500	0.0046	36000

Table 7.1.: Cross section for $Z \rightarrow ee$ inclusive for LO.

decay into an electron-positron pair ($BR(Z*/\gamma \rightarrow ee) = 0.03363$) [7]. In the right column the numbers of generated inclusive[3] Drell-Yan events are listed.

The k-factors for next-to-next-to-leading order corrections (NNLO) (see Sec. 4.1.5) are listed in Tab. 7.2 and have to be applied to the cross section [60]

Since the Z-bosons were generated with the wrong momenta distribution [61], a reweighting was performed [62]. This yields a larger weighting of events with higher transverse momentum of the Z-bosons. A high transverse momentum

[3]Inclusive means initial and final state radiation are provided in this sample.

Mass of Z [GeV]	NNLO k-factor	Mass of Z [GeV]	NNLO k-factor
10 – 20	$1.233\ ^{+0.057}_{-0.052}$	200 – 250	$1.411\ ^{+0.034}_{-0.052}$
20 – 30	$1.254\ ^{+0.051}_{-0.047}$	250 – 300	$1.409\ ^{+0.037}_{-0.056}$
30 – 40	$1.277\ ^{+0.048}_{-0.045}$	300 – 400	$1.400\ ^{+0.042}_{-0.067}$
40 – 50	$1.297\ ^{+0.046}_{-0.044}$	400 – 500	$1.391\ ^{+0.047}_{-0.081}$
50 – 75	$1.341\ ^{+0.047}_{-0.043}$	500 – 600	$1.382\ ^{+0.053}_{-0.095}$
75 – 91.1	$1.361\ ^{+0.048}_{-0.043}$	600 – 700	$1.375\ ^{+0.062}_{-0.111}$
91.1 – 100	$1.369\ ^{+0.047}_{-0.043}$	700 – 800	$1.370\ ^{+0.073}_{-0.128}$
100 – 150	$1.397\ ^{+0.043}_{-0.045}$	800 – 900	$1.368\ ^{+0.087}_{-0.146}$
150 – 200	$1.408\ ^{+0.031}_{-0.048}$	900 – 1000	$1.371\ ^{+0.105}_{-0.167}$

Table 7.2.: NNLO k-factor for the Drell-Yan process.

arises because the Z-bosons recoils against jets. Thus, the ratio of jets in this sample is expected to increase. This is reasonable because higher transverse momenta appear due to gluon radiation of the incoming partons.

7.3.2. WW Di-boson channel

FSR or ISR can occur in the WW production (Feynman graph in Fig. 7.2) in the same way as in a Drell-Yan process. If the two W-bosons decay in the

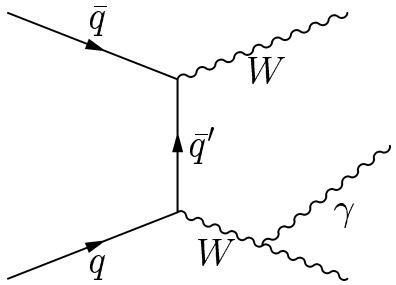

Figure 7.2.: Feynman graph of a WW production with FSR of a photon.

electron channel, the signature can be, together with ISR or FSR of a photon, the same as for the signal process, i. e. $ee\gamma$. But also radiation of a quark or a gluon by one of the initial partons, resulting in a jet, can fake the signature, if the jet was misidentified as a photon.

The NLO cross section for $p\bar{p} \to WW$ is

$$\sigma_{NLO} = 8.137\,\text{pb} \cdot 1.416 = 11.521\,\text{pb} \tag{7.1}$$

For this sample 200750 events have been generated.

7.3.3. WZ Di-boson channel

An instrumental background is the process $q\bar{q} \to WZ$. A possible Feynman

graph is shown in Fig. 7.3. This process has the same signature as the signal process, in the case of W and Z decaying in the electron channel and one electron being misidentified as a photon. The measured final state is also $ee\gamma$, because the neutrino is not detectable in the DØ detector.

If no track match is required, photons and electron are both identified as EMO (see Sec. 6.2.4). Then this process would be physics background.

The cross section as well as the k-factor (NLO) and the number of generated events are listed in Tab. 7.3. The correction factors for this process as well as

Process	σ_{LO} [pb]	k-factor (NLO)	# events
W^-Z	1.227	1.4611	
W^+Z	1.228	1.458	
	σ_{NLO} [pb]		
WZ	3.584		95500

Table 7.3.: Cross sections , k-factors and number of generated events for the process ($q\bar{q} \rightarrow WZ$).

for the WW production (Sec. 7.3.2) and ZZ production (Sec. 7.3.4) are taken from [63].

7.3.4. ZZ Di-boson channel

In the case of ZZ production the decay of both bosons into an electron-anti-electron pair is possible. This fakes the signal signature if one electron was not detected and, like in the case of WZ production, one of the three remaining electrons was mis-identified as a photon.

102750 Events were generated with a cross section of

$$\sigma_{NLO} = 1.026\,\text{pb} \cdot 1.387 = 1.423\,\text{pb} \tag{7.2}$$

The Feynman graph for the ZZ production is displayed in Fig. 7.4.

7.3.5. QCD

QCD Background are jets faking EMO. This can occur in different modes of which two are considered in this search, jets faking photons or electrons.

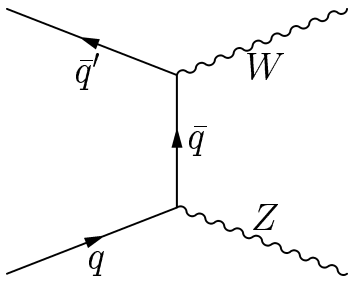

Figure 7.3.: Feynman graph of a WZ inclusive production.

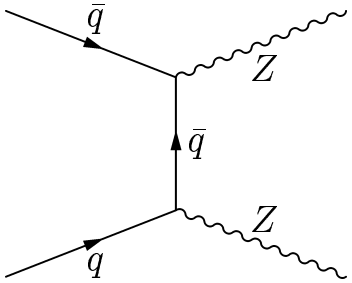

Figure 7.4.: Feynman graph of a ZZ inclusive production.

The first possibility is a process with two jets and a photon, where the jets fake the electrons. There are no MC events available to consider those processes. Thus, a QCD sample is extracted from the data to estimated the contributions to the background (see Sec. 8.2.1). This is realized by an inverse H-matrix requirement, which is reasonable since the H-matrix is a sophisticated quantity to distinguish Jets and EMO in the electromagnetic calorimeter. The obtained sample is then fitted with χ^2-fit to the data, with respect to the shape (see Sec. 8.2.1).

Another QCD background process is a final state containing two electrons, arising for example from the Drell-Yan channel, with an additional jet from ISR. If the jet fakes a photon, the final state is the same as for the signal. The simulated Drell-Yan inclusive events already provide the ISR and FSR of partons, hence jets. To estimate the amount of events, where a jet fakes an electron, the Drell-Yell MCs were scanned on parton level (see Sec. 8.2.2.1).

7.4. The Signal Processes

MCs were produced for the signal of excited electrons. The full MC generation chain was run through only for the production via CI.

Masses from 100 GeV up to 1 TeV, in steps of 100 GeV for the signal process ($e^* \to e\gamma$) were generated. In Tab. 7.4 the signal cross sections are listed for every mass point including the BR for the decay into a photon and an electron. The number of generated events are listed for each mass. Also the branching fractions BF(GM) (see Fig. 3.7) are listed. It considers the two possible decay modes, via GM and CI.

The cross section already takes into account the branching ratio for the chosen decay $e^* \to e\gamma$ (via GM). The compositeness scale was chosen to be $\Lambda = 1\,\text{TeV}$. In Fig. 3.4 the cross sections are shown graphically. For the NNLO correction (for α_s^i, $i = 0, 1, 2$) the same k-factor like for the Drell-Yan process are used [64]. This is reasonable because both processes differ only in their outgoing particles. It is supposed, that for such corrections the excited electron behaves like an SM electron.

mass [GeV]	$\sigma^{CI}_{prod}(NNLO)$ [pb]	BF(GM)	# events
100	27.55	0.903	4250
200	7.37	0,700	5000
300	3.11	0.510	4250
400	1.31	0.396	5000
500	0.60	0.272	3750
600	0.28	0.206	3750
700	0.094	0.160	3250
800	0.035	0.128	5000
900	0.011	0.104	5000
1000	0.0031	0.086	4500

Table 7.4.: Cross section for the signal, the branching fraction for the decay via GM, and the number of generated signal events.

8. Analysis

In this chapter the selection and the analysis of data and Monte Carlo events is presented. Data corresponding to an integrated luminosity of $996.56 \pm 62.78\,\mathrm{fb}^{-1}$ was analyzed.

The pre-selection criteria are explained in Sec. 8.2.1. Plots are presented to show good agreement of data and the Standard Model MCs. In Sec. 8.2.2.1, the final sample for this search, i. e. two electrons and a photon, is discussed. The estimated systematic uncertainties of the search algorithm are discussed in Sec. 8.3 All quantities in conjunction with the signal are given for a compositeness scale of $\Lambda = 1\,\mathrm{TeV}$.

A brief elucidation of the MC events for excited electrons produced via GM is given in Sec. 8.4.

8.1. Data

The common sample group (CSG) [65] provides the data and creates data subsamples. These "skims" are sets of data events pre-classified for different purpose, e. g. at least one muon, or at least two electrons of certain qualities. The skim used in this analysis is CSG_CAF_2EMhighpt_PASS3_p17.09.03. At least two electromagnetic objects [50] with a transverse momentum larger than 12 GeV are required. The luminosity calculation for this skim yield $997 \pm 63\,\mathrm{pb}^{-1}$ (see Sec. 5.2.7).

8.2. Event Selection

To check the understanding of the data, a pre-selection sample is created (Sec. 8.2.1) and studied. At least two electrons that satisfy various requirements are demanded. The results of these cuts are presented.

In order to search for the signal signature $ee\gamma$, an additional photon is required. This selection is called the final sample. It is presented in Sec. 8.2.2. Consistency controls are applied.

8.2.1. Pre-Selection

A pre-selection is applied first, to check the description of data by the MCs. At least two electrons were asked, that fulfill the following certified requirements for tight_hmx_trk [51] electrons:

- |EM-ID| = 10 or |EM-ID| = 11 ($p_T > 1.5\,\mathrm{GeV}$ or $p_T > 1.5\,\mathrm{GeV}$, depending on the used reconstruction algorithm, $emfrac > 0.9$) and $iso <$

0.2. The two objects have to satisfy the requirements for electromagnetic objects (see Sec. 6.2) [50].

- $|\eta| < 1.1$ or $1.5 < |\eta| < 2.5$
  Only the well instrumented regions of the calorimeter (see Sec. 5.2.4) are used.

- $p_T > 15\,\text{GeV}$
  This requirement was tightened compared to the certification cut ($p_T > 3\,\text{GeV}$.) This is reasonable because the electrons tend to have transverse momenta higher than 15 GeV, due to the high mass of the excited electron. Also the trigger efficiency is about 100% for electrons that satisfy this requirement.

- HMx7<12 for CC and HMx8<20 for EC
  The shower shape should be electromagnetic to suppress background from jets (see Sec. 6.2.3).

- $Prob\,(\chi^2_{trk}) > 0.01$
  To distinguish between electrons and photons a track match is required (see Sec. 6.2.4).

- $\Delta R > 0.4$
  The two electrons have to be separated to assure a good reconstruction inside the electromagnetic calorimeter (see Eq. 6.2).

In Tab. 8.1, the cut flow is shown for the search for excited electrons with a mass of 300 GeV and 800 GeV. For the signal the acceptance ϵ is listed. In the case of data as well as of the SM background, the number of events that passed the requirements are listed. The first requirements in Tab. 8.1 are only listed

cut	Data [# events]	SM BG [# events]	Signal ϵ [%] (300 GeV)	Signal ϵ [%] (800 GeV)
Object ID = 10, 11			0.999	0.999
$iso \leq 0.2$			0.999	0.999
$emfrac \geq 0.9$			0.999	0.999
$p_T \geq 3\,GeV$			0.999	0.998
# EMO ≥ 1			0.999	0.998
# EMO ≥ 2			0.965	0.959
$p_T > 15\,GeV$	5116300	91578	0.690	0.725
track matched	95639	66748	0.455	0.491
HMx7/8 < 12/20	65266	61477	0.401	0.445
$\Delta R > 0.4$	64984	61462	0.392	0.424

Table 8.1.: Cut flow to obtain the pre-selection sample. For the data and the SM background, the number of events that passed the requirements are listed. For the signal the acceptance is given exemplary for masses of 300 GeV and 800 GeV. The contribution by QCD is not listed here.

in detail for the signal, because these requirements have already been applied in the generation of MC events. The cut flow is exemplary shown for a low (300 GeV) and a high (800 GeV) excited electron mass.

The SM background is weighted to the luminosity of the data, so both correspond to the same integrated luminosity. Also a correction by a factor ϵ_{corr} was applied, to consider inefficiencies of the cuts (see below). Hence, the SM background and the measured data can be compared, taking into account the contribution of QCD events (3763), which are obtain by a fit (see below). This yields

data events: 64984

SM background: $65225 \pm 6048 \pm 230$

Here, the SM background events includes QCD events. The uncertainties for the QCD events acquired from data are not given (see Sec. 8.3).

The invariant mass of the two selected electrons is plotted in Fig. 8.1. It was distinguished between the three different combinations of regions in the electromagnetic calorimeter where the EMOs where detected, i. e. CC/CC, CC/EC, and EC/EC. One can notice that not only the total number of data and SM background events match well. Also the shapes in Fig. 8.1 (a) and (b) show a very good agreement for data and SM background, taking into consideration the scaled QCD sample.

The invariant mass for both objects being detected in EC is not illustrated. However, it shows a similar agreement.

The measurement of the different requirements suffers from certain inefficiencies. The response of the detector is not simulated perfectly in the MC. The correction factor

$$\epsilon_{corr} = \frac{\text{efficiency}_{\text{MC}}}{\text{efficiency}_{\text{data}}} \tag{8.1}$$

takes this into account and is provided by a CAF processor [51]. It is shown in Fig. 8.2 in dependency of η.

The triggers for electromagnetic objects (see Sec. 5.2.7) are almost 100% efficient. Since other DØ searches have confirmed this value [66, 67], also in this analysis 100% efficiency was assumed.

As mentioned above, the contribution from QCD was not considered in the cut flow of the SM background. To obtain the QCD sample, the shower shape cut for two EMOs was inverted. This yields a rejection of electrons which satisfy all above listed cuts. However, it provides a sample with an invariant mass spectrum shape of mis-identified electrons and genuine QCD background. This QCD sample was scaled with a factor f_{QCD}, which was obtained from a χ^2-fit on the data. The QCD contribution increases to lower invariant masses. Thus, the fit is applied in the lower mass region, from 44 GeV to 100 GeV. In this region, the signal contribution is negligible and is thus not affected by the fit.

The QCD sample is obtained separately for the two region, because the shower shape requirements are different for CC (HMx7) and EC (HMx8). Thus, this was performed for the three possible combinations of detection regions,

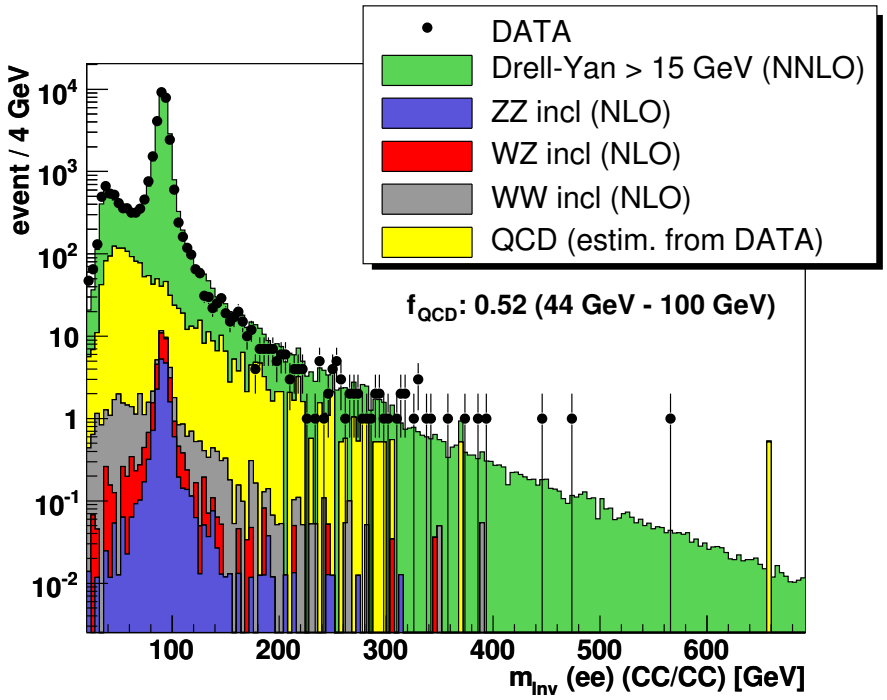

(a)

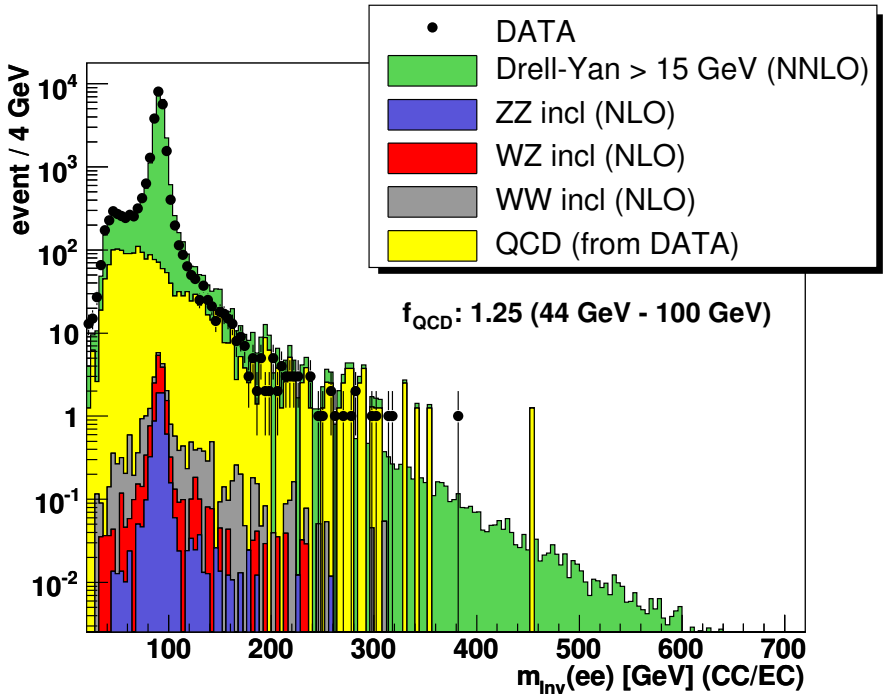

(b)

Figure 8.1.: The invariant mass of the two pre-selected electrons. (a) shows the invariant di-electron mass in the case, that both were detected in the central region of the electromagnetic calorimeter. In (b) one electron is asked to be detected in the central region, a second in the end region.

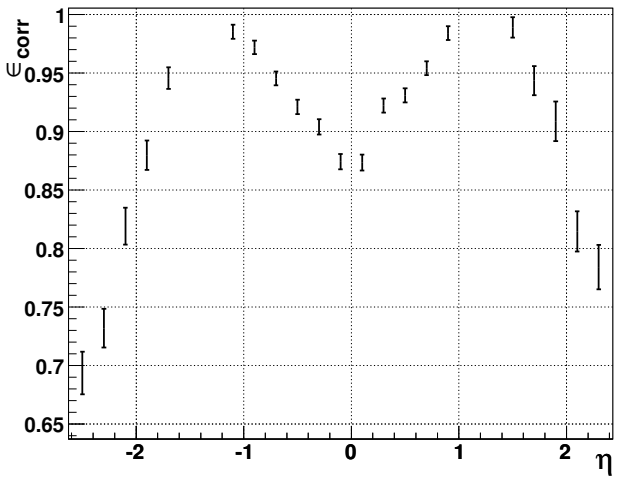

Figure 8.2.: Correction factor ϵ_{corr} in dependency of η, shown for the region used in this analysis.

i. e. CC/CC, CC/EC, and EC/EC. The fit parameters f_{QCD} for the three regions are listed in Tab. 8.2.

Region	CC/CC	CC/EC	EC/EC
f_{QCD}	0.52	1.25	2.53

Table 8.2.: Scale factor for the QCD sample divided in the three possible combination of detection region.

8.2.2. Final Sample

From the pre-selection sample the final sample is obtained by requiring an additional photon (Sec. 8.2.2.1). To demonstrate the agreement of the SM background and data control plots are shown in Sec. 8.2.2.2.

8.2.2.1. $ee\gamma$ Selection

The following requirements are applied on the pre-selection ee sample to obtain an additional photon and thus the searched signature. The additional requirements for the photon were taken from a $Z\gamma$ [68] and a $W\gamma$ [69] analysis at DØ and have also been used in the search for excited muons [31] at DØ. Cuts that are not commented were already explained in Sec. 8.2.1.

- # EMO ≥ 3 with $p_T > 15\,\text{GeV}$ and $Prob\,(\chi^2_{trk}) < 0.01$
  A third EMO, the photon, is required with a transverse momentum larger than 15 GeV and with a track veto.

- σ_ϕ_EM3 $< 14\,\mathrm{cm}^2$
  The ϕ width in the third layer[1] of the electromagnetic calorimeter acts as an additional requirement to distinguish between EMOs and QCD background.

- track isolation
  For the third object, i. e. the photon, a track veto is required. To avoid objects that were produced by mis-assignments of tracks, a track isolation is required. The sum of transverse momenta of all tracks within a hollow cone of $0.05 \leq \Delta R < 0.4$ has to be smaller than 2 GeV.

- $\Delta R > 0.7$ to both EMOs
  For the signal process, the photon tends to be well separated from both electrons of the pre-selection sample. Hence, the separation cut, which was already performed on the two electrons, was tightened for the third object.

- HMx7/8 $< 12/20$
  The shower shape should be the one of electromagnetic objects to avoid QCD events.

The cut flow for the final selection is shown in Tab. 8.3. The acceptance is again listed for an excited electron masses of 300 GeV and 800 GeV.

cut	Data [# events]	SM BG [# events]	Signal ϵ [%] (300 GeV)	Signal ϵ [%] (800 GeV)
3^{rd} EMO ($p_T > 15$ GeV & track veto)	942	609	0.377	0.417
σ_ϕ_EM3$< 14\,\mathrm{cm}^2$	643	431	0.375	0.416
track isolation	629	362	0.360	0.403
$\Delta R > 0.7$	337	257	0.295	0.312
Hmx7/8 $< 12/20$	251	211	0.261	0.262

Table 8.3.: Cut flow to obtain the final sample, for the search of an excited electron with a mass of 300 GeV and 800 GeV. For the data and the SM background, the number of events that passed the requirement are listed. For the signal, the acceptance is given. The contribution of QCD was not considered here.

The contribution from the QCD sample amounts to 23 events that fulfill all requirements. Thus, in the final sample the SM background MC and the QCD describe the data with very good agreement within uncertainties:

data events: 251

SM background: $234 \pm 28 \pm 13$

[1] The shower shape can be resolved twice as good in the fine segmented third layer (see Sec. 5.2.4).

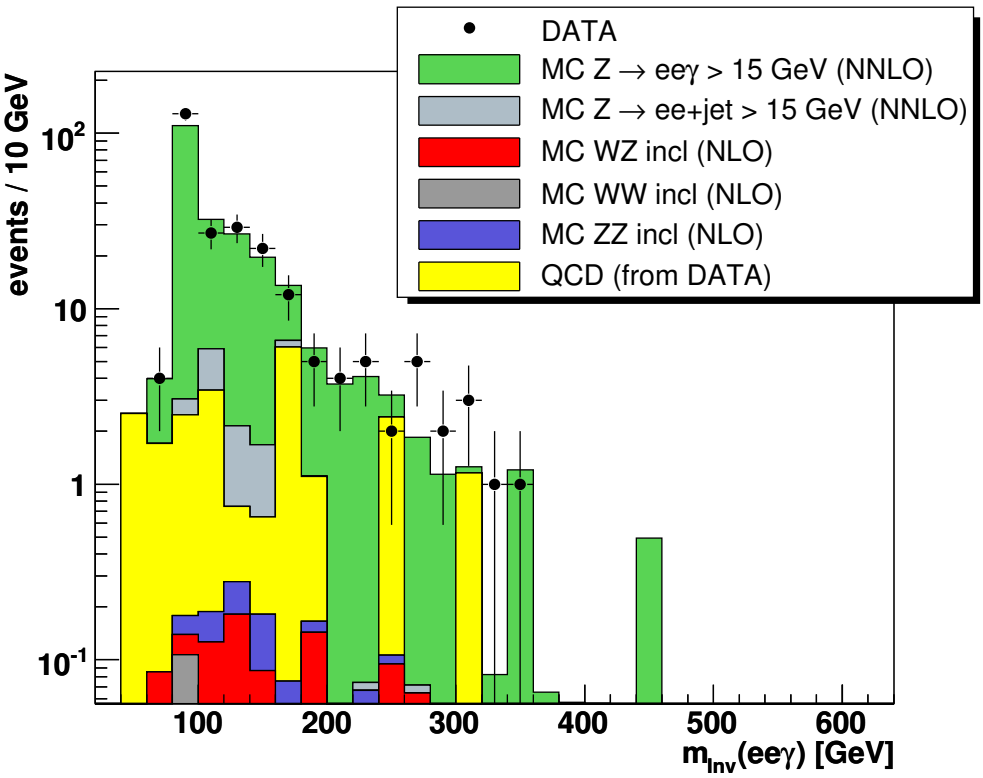

Figure 8.3.: The invariant mass of $ee\gamma$.

The uncertainties are explained in detail in Sec. 8.3.

The invariant mass of the final $ee\gamma$ sample is plotted in Fig. 8.3. Like for the pre-selection sample, the data is described well by the SM background MCs and the scaled QCD sample.

The in-efficiencies of the requirements for photons are considered in Tab. 8.3 by a global correction factor $\epsilon^{\gamma}_{corr} = 0.95 \pm 0.05$. This value is adopted from an other DØ analysis, which searched for the same final state [70].

To estimate the contribution of jets faking photons[2], the Drell-Yan sample was scanned on parton level. More precisely, a photon was demanded that satisfies tight photon requirements, i. e. $p_T > 12\,\text{GeV}$, inside the instrumented region of the electromagnetic calorimeter ($|\eta| < 1.15$ or $1.45 < |\eta| < 2.55$). Events that fulfill this requirement were tagged. On detector level, events with an $ee\gamma$ final state are probed. If untagged, it is traded as an $ee + jet$ event, where the jet fakes a photon. The fake rate was estimated to be 2.9 %.

In the following, the Drell-Yan sample is split into physics background ($Z \to ee\gamma$) and instrumental background ($Z \to ee + jet$). Their uncertainties are estimated separately (see Sec. 8.3.6). They originate in the case of physics background from the correction factor ϵ^{γ}_{corr} for the photon requirements, and in the case of instrumental background from the imperfect simulation of jets faking photons.

[2] although cuts to suppress such effects were applied

8.2.2.2. Consistency Check

To check the agreement of data and MC events for the final sample, the invariant mass of the final state is plotted in Fig. 8.3. Only statistical uncertainties were considered. The data is described very well by the SM background. The few discrepancies are within the systematical uncertainties. The main contribution originates from the Drell-Yan process.

Some kinematic quantities are shown in Fig. 8.4 to check their distributions. In Fig. 8.4 (a-c) the transverse momenta of the three final state particles $ee\gamma$ are plotted. The two electrons were sorted by their transverse momentum, such that Fig. 8.4 (a) shows the distribution for the leading p_T electrons of each event and (b) for the second leading p_T electrons. The photon was identified by the track veto. It tends to have lower transverse momentum than the two electrons. All three momentum distributions show a very good description of data by the SM background.

Fig. 8.4 (d) shows the η distribution for the leading p_T electron. In Fig. 8.4 (e) and (f) the separation between one of the electrons and the photon is plotted. This is for Fig. 8.4 (e) the leading p_T electron and for (f) the second leading. Also for the three distributions (d-f) the agreement of data and SM background is very good.

8.3. Systematic Uncertainties

8.3.1. Correction Factors

Correction factors [51] are applied to consider differences between data and MC in the efficiencies of all cut requirements (see Sec. 8.2.1). These factors suffer from uncertainties, which, in the case of the two electrons, were included in Fig. 8.2. The maximum uncertainty occurs at high η-regions. For the region considered in this analysis, for each electron the maximum uncertainty, i. e. 2.5%, is considered for a conservative estimation.

For the photon the uncertainty due to the correction factor is given with 5.3% [70].

8.3.2. Trigger

As mentioned in Sec. 8.2.1, the triggers are almost 100% efficient. This was measured in other DØ analyzes [66, 67, 71] by the tag-probe method. For this method one electron was required in $Z \to ee$ events. Then cuts were performed on this electrons and for a second the trigger turn-on curves and efficiencies are determined. The uncertainties on this method are concluded conservatively to $^{+0\%}_{-3\%}$.

8.3.3. Luminosity

Also the luminosity calculation is effected by uncertainties. The main contributions originate from uncertainties of the inelastic cross section and the

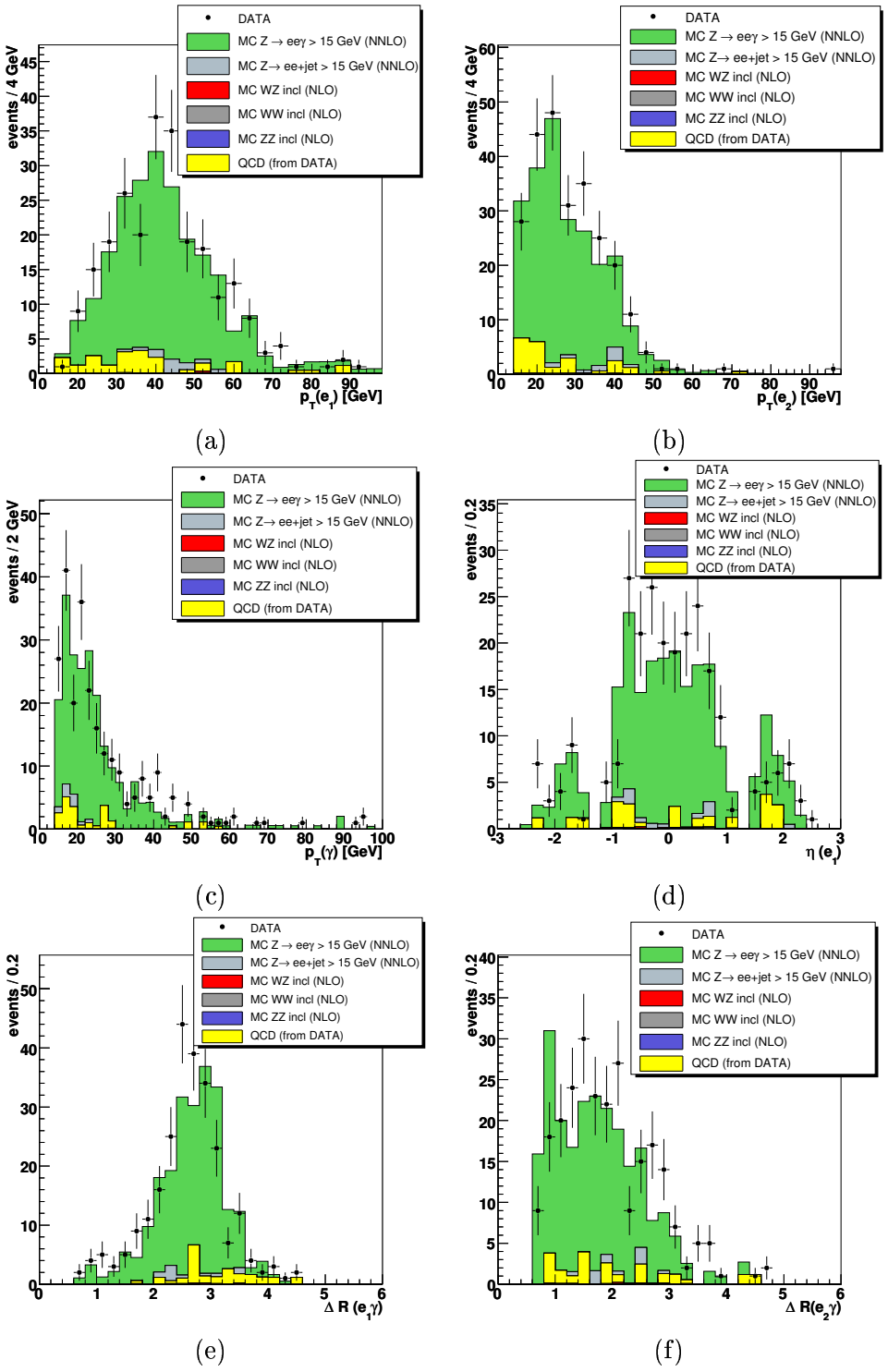

Figure 8.4.: Control plots for the final sample. (a) shows the transverse momenta for the leading p_T electron, (b) for the other electron, and (c) for the photon. In (d) the η distribution of the leading p_T electron is plotted. (e) illustrates the separation between the photon and the leading p_T electron, (f) between the photon and the second leading one.

acceptance of the luminosity monitor (see Sec. 5.2.6). The sum in quadrature over all contributions yields a total uncertainty for luminosity of 6.3% [44].

8.3.4. NLO and NNLO Corrections

The NLO and NNLO corrections are included by the k-factor which also suffers from uncertainties. These are listed in Tab. 7.2. The relative uncertainties are shown in Tab. 8.4 for the different masses of the excited electron.

mass [GeV]	k-factor uncert. [%]	PDF accpt. uncert. [%]
100	3.3	0.83
200	2.8	0.29
300	3.3	2.30
400	3.9	1.74
500	4.6	0.12
600	5.4	0.39
700	6.3	0.34
800	7.3	0.40
900	8.5	0.12
1000	9.9	0.56

Table 8.4.: Uncertainties on the total cross section of the Drell-Yan and the signal process due to NLO and NNLO corrections. In the right column the uncertainties due to the PDFs is shown.

8.3.5. QCD scaling

Uncertainties originating from the method used to obtain the QCD sample are not considered. This is motivated by the fact that in the final sample the contribution of QCD events is expected to be negligible, especially after applying the cut for the limit calculation (see Sec. 9.1). It also is expected to be small in comparison to the uncertainties of the correction factors (see Sec. 8.3.1).

The QCD sample was scaled with a χ^2-fit to the shape for the three regions of the electromagnetic calorimeter. The uncertainties to this fit with respect to the ratio of QCD to SM background events are listed in Tab. 8.5. The linear

CC/CC	CC/EC	EC/EC
0.52%	0.55%	1.3%

Table 8.5.: Errors on f_{QCD} due to the χ^2-fit for the QCD sample with respect to the complete SM background.

addition of these errors yield an uncertainty of 0.15%. This value is negligible with respect to the other uncertainties.

8.3.6. Jet Faking a Photon

The rate of jets faking photons in the Drell-Yan sample was obtained from comparison of generator and detector level information. Conservatively, an uncertainty of 100% is estimated. This yields an additional uncertainty for the signal acceptance equal the faking rate, i. e. 2.9%.

8.3.7. Parton Density Function

Uncertainties due to the PDFs affect the theoretical production cross sections as well as the acceptance for the signal.

The uncertainty on the cross section is considered in the limit calculation (see Sec. 9.2).

The PDF uncertainties affected by the k-factor are listed in Tab. 8.4 [60]. These are the same values as for the Drell-Yan process. This is reasonable because the higher order sub-processes are almost the same for both, the production of excited electrons and the Drell-Yan process (compare with [64]).

To determine the uncertainties on the signal acceptance, information delivered by the "pdf_reweighting" processor [48] is used. With this processor the events are reweighted from CTEQ6L (LO) to CTEQ6M (NLO) with respect to their Bjorken-x (see Sec. 4.1.4). For every incoming proton 20 error functions were determined. The acceptance aberration from every of the 20 error functions to CTEQ6M cross section is determined for every function. The quadratical summation of all aberrations yields the acceptance uncertainty for the signal. This acceptance uncertainty for CTEQ6M is now assumed for the generated signal events (CTEQ6L) [72]. The resulting values are listed in Tab. 8.4. Conservatively, the uncertainty for the acceptance due to the PDF is estimated to 2.3%.

8.4. The Gauge-Mediated Production Sample

For the production via GM, the generation of MC events was only performed on parton level. Nonetheless, some estimations can be used to forecast results for this production channel.

As discussed in Ch. 3, the cross section for GM is much lower than for CI (see Fig. 3.4). Thus, less events are expected to occur in the data. However, the acceptance of the requirements listed in Sec. 8.2.2.1 and Sec. 8.2.1 is supposed to be larger, because the transverse momenta of the produced excited electron and the associated electron, shown in Fig. 8.5, increase to higher masses. Hence, more events are expected to pass the cut $p_T > 15\,\text{GeV}$. More important, due to higher transverse momenta, the ratio of excited electrons that go towards the CC increases. This yields a larger ratio of decay remnants, i. e. an electron and a photon, in the low η region. Thus, the efficiency of all requirements increases while the uncertainties for these decreases, as Fig. 8.2 shows.

However, this is strongly depending on the value of the compositeness scale Λ. In Ch. 3 was already discussed, that the cross section and thus the expected number of events is much lower for the production of excited electrons

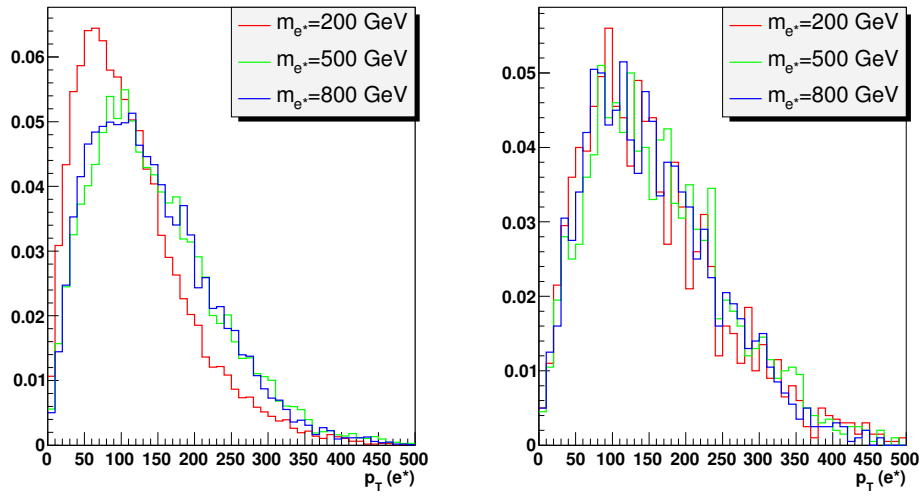

(a) (b)

Figure 8.5.: Fig. (a) shows transverse momenta distribution on generator level for excited electrons produced via GM. The distribution is plotted for three different masses (200 GeV, 500 GeV, 800 GeV). The transverse momenta increase for higher masses. Fig. (b) shows the transverse momentum for excited electrons produced via CI. The distribution remains similar for different masses.

via gauge-mediated interaction. Nevertheless one should keep in mind, that there is no indication for any of the two interactions to describe the underlying new strong interaction well. So both should be analyzed independently.

9. Results

In this chapter the results of this search are presented. Since the data and the SM background agree very well and no excess was observed (see Sec. 8.2), experimental limits were set to the contact interaction production cross section of excited electrons. For the production cross section via gauge-meditated interaction estimation for an expected limit are made. Also for the compositeness scale Λ limits were set.

9.1. Final Sample and Signal

The invariant mass distribution of the final $ee\gamma$ sample is shown in Fig. 9.1 for two different signal masses, 300 GeV and 800 GeV. The signal is clearly separated from data and the SM background. No excess in data is observed.

The invariant mass of the searched excited electron is reconstructed by selecting the photon and one of the two electrons out of the final sample (Fig. 9.3). This selection is performed with respect to the optimal reconstructed invariant mass. This means, that electron is chosen such that, together with the photon, the invariant mass is closest to the searched signal mass.

This method causes a certain bias on the invariant mass distribution of $e\gamma$. However, the effect is only crucial for low invariant masses (see Fig. 9.2 (a) and (b)). Comparing the different plots in Fig. 9.3 (a) and (b) one can see, that the distortion effect due to this selection on data as well as on the SM background is negligible for masses above 300 GeV. The maximum effect is reached for 300 GeV.

To gain competitive results, cuts are performed considering a ratio of signal to square root of background events as high as possible. This ratio affects the expected limit for the cross section as well as the signal purity. Good results are obtained by selecting a symmetric mass region around the searched signal mass that contains 99% of the integrated events. The range of this region was limited to 35% of the searched signal mass. The cut ranges for each signal mass point are listed in Tab. 9.1.

The selected data and SM background events as well as the signal efficiency after this cut are listed in Tab. 9.2. For the SM background events and the signal efficiency, systematical and statistical uncertainties are considered. Comparing the event numbers with respect to the uncertainties no excess is observed.

However, the above mentioned bias effect causes a relatively large number of data and SM background events in the cut region for 100 GeV and 200 GeV (see Tab. 9.2), which affects the limit for this mass region (see Tab. 9.3).

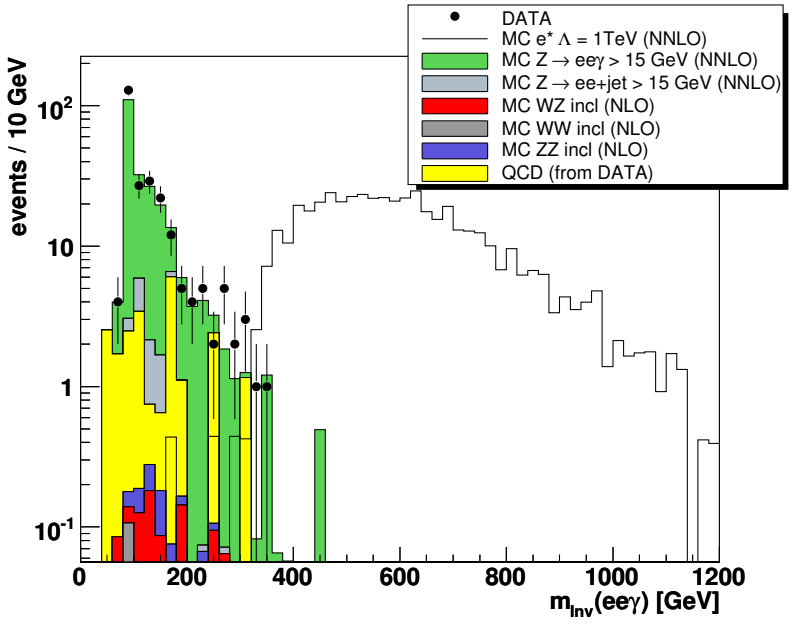

(a)

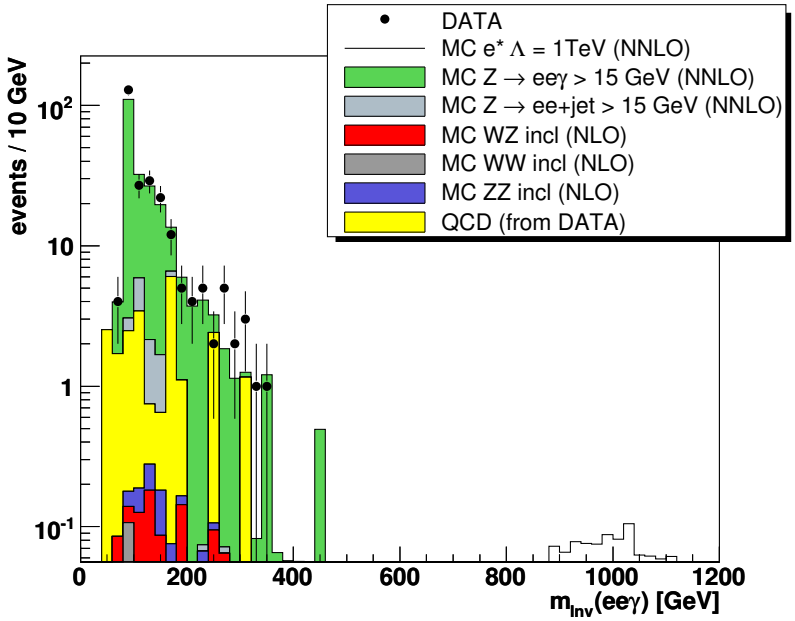

(b)

Figure 9.1.: The invariant mass of the final state $ee\gamma$ for excited electron masses of (a) 300 GeV and (b) 800 GeV.

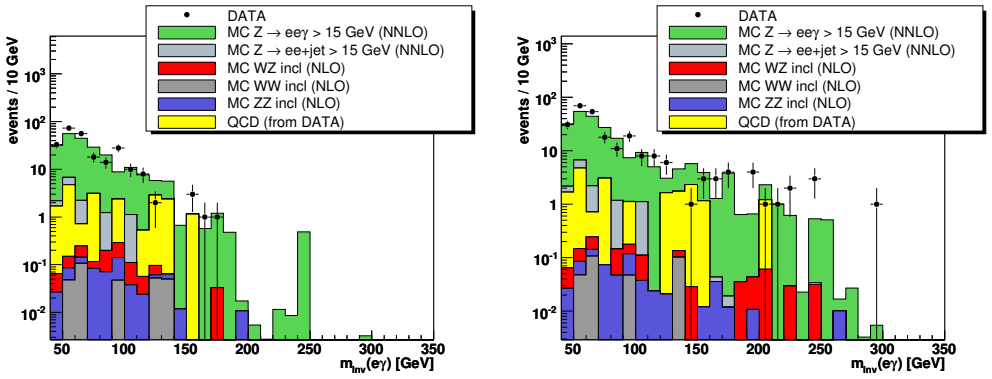

(a) (b)

Figure 9.2.: The invariant mass distribution of data and the SM background. Fig. (a) shows the distribution for the $e\gamma$ selection for a 100 GeV excited electron and (b) for 200 GeV. A shift to higher masses is obvious, when using higher excited electron masses for the electron selection.

9.2. Cross Section Limits

Since no excess in data is observed limits are set. For the production cross section of single excited electrons upper limits and for the mass lower limits are set. The limits are calculated using the Bayesian approach and Poisson statistics [73]. The program used ("limit_calculators") is provided by [74].

The results of the limit calculation with 95% confidence level are listed in Tab. 9.3. It shows also the limits without considering systematic uncertainties. One can see that for higher masses the limits are almost equal, with and without considering the systematic uncertainties. Thus, there is only a very small dependency of the limit on systematic uncertainties.

In Fig. 9.4 (a), the production cross sections for several values of the com-

e^* mass [GeV]	cut range [GeV]
100	80 - 120
200	170 - 230
300	260 - 340
400	270 - 530
500	420 - 580
600	460 - 740
700	590 - 810
800	520 - 1080
900	630 - 1170
1000	690 - 1310

Table 9.1.: For every signal mass point the range for the cut is given. Events inside this range were selected for the limit calculation.

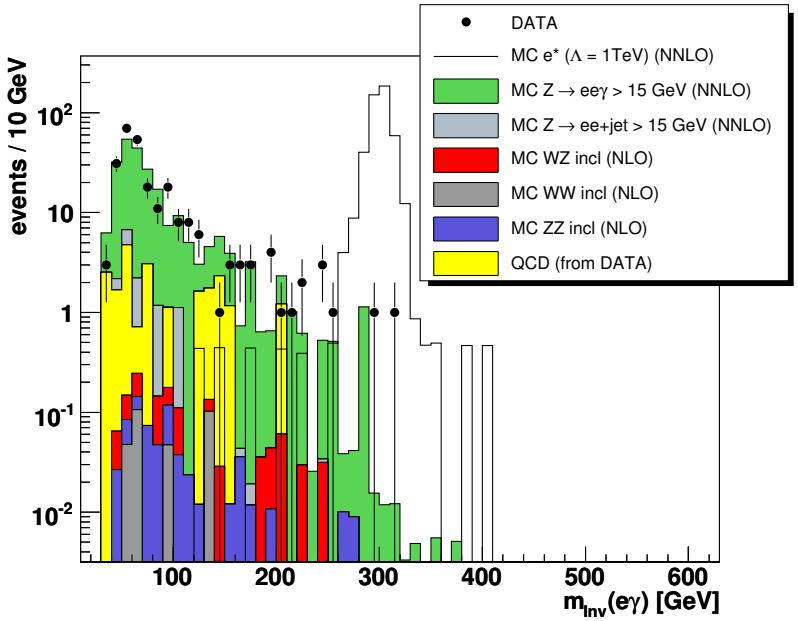

(a)

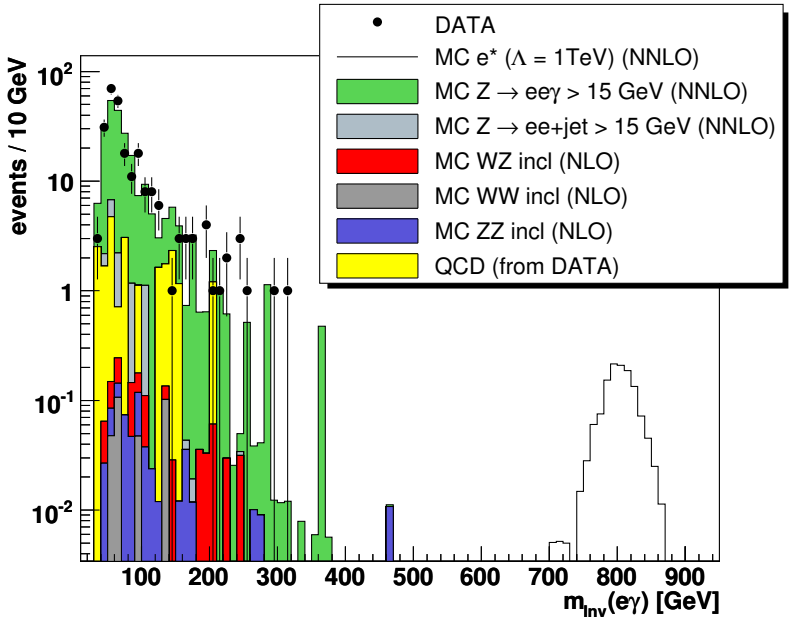

(b)

Figure 9.3.: The invariant mass for the excited electron remnant particles e and γ for masses of (a) 300 GeV and (b) 800 GeV. This distribution was obtained by selecting the best combination for the searched mass.

mass	Data [# events]	SM BG [# events]	Signal ϵ [%]
100	78	$77 \pm 9 \pm 8$	$19.3 \pm 2.1 \pm 0.7$
200	15	$11 \pm 1.3 \pm 2$	$24.2 \pm 2.7 \pm 0.7$
300	3	$1.8 \pm 0.2 \pm 0.6$	$25.9 \pm 2.9 \pm 0.8$
400	2	$1.8 \pm 0.2 \pm 0.6$	$26.8 \pm 3.0 \pm 0.8$
500	0	$0.2 \pm 0.02 \pm 0.18$	$28.2 \pm 3.1 \pm 0.9$
600	0	$0.02 \pm 0.003 \pm 0.01$	$27.3 \pm 3.0 \pm 0.9$
700	0	$0.001 \pm 0.0001 \pm 0.0004$	$28.0 \pm 3.1 \pm 1.0$
800	0	$0.001 \pm 0.0001 \pm 0.0004$	$25.9 \pm 2.9 \pm 0.8$
900	0	$0.0008 \pm 0.0001 \pm 0.0003$	$27.5 \pm 3.1 \pm 0.8$
1000	0	$0.0005 \pm 0.0001 \pm 0.0003$	$27.3 \pm 3.0 \pm 0.8$

Table 9.2.: Selected data and SM background events for every excited electron mass. The efficiency for the signal is listed in the right column.

mass [GeV]	$\sigma_{prod} \times BR(e^* \to e\gamma)$ [pb]	$\sigma_{prod}^{\text{w/o sys}} \times BR(e^* \to e\gamma)$ [pb]
100	0.214	0.132
200	0.064	0.055
300	0.026	0.024
400	0.020	0.019
500	0.011	0.011
600	0.012	0.011
700	0.011	0.011
800	0.012	0.012
900	0.012	0.011
1000	0.012	0.011

Table 9.3.: Upper cross section limits for the production of single excited electrons with 95% CL. In the right column, the limits with out considering systematic uncertainties are shown.

positeness scale ($\Lambda = m_{e^*}$, 1 TeV, 2 TeV, 3 TeV, 4 TeV, 5 TeV) are shown. The theoretical uncertainties are estimated to 10% (dashed lines in Fig. 9.4). It was adopted from Drell-Yan uncertainties [64]. The dependency of the production cross section limit is evident.

Limits for three different values of Λ are shown in Fig. 9.4 (b). The lower mass limit for excited electrons was determined to 739 GeV (806 GeV, 934 GeV) for $\Lambda = 1$ TeV ($\Lambda = m_{e^*}$ with and without BF(GM), .i .e. consideration of a decay via CI (see Fig. 3.7)).

The higher limits, i. e. for $\Lambda = m_{e^*}$ with and without BF(GM), are set to compare the results with recent ones from the CDF Collaboration[25]. In their work, the branching fraction BF(GM) (see Sec. 7.4) was set to one and a compositeness scale of $\Lambda = m_{e^*}$ was chosen. They set a lower mass limit on the excited electron of 879 GeV.

All results are with respect to $f = f'$ (see Sec. 3.2.2). Looking for example

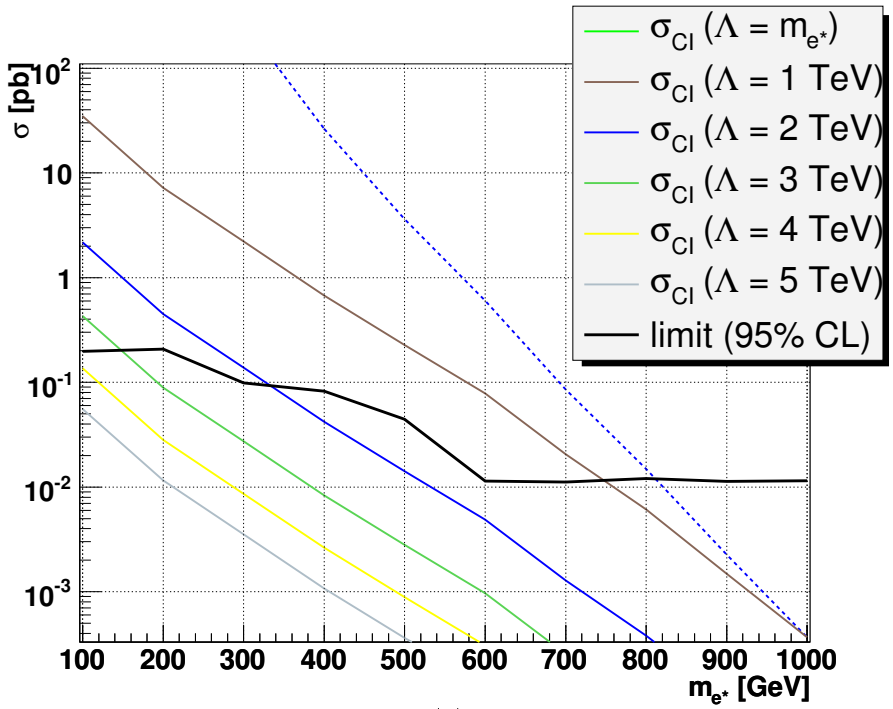

(a)

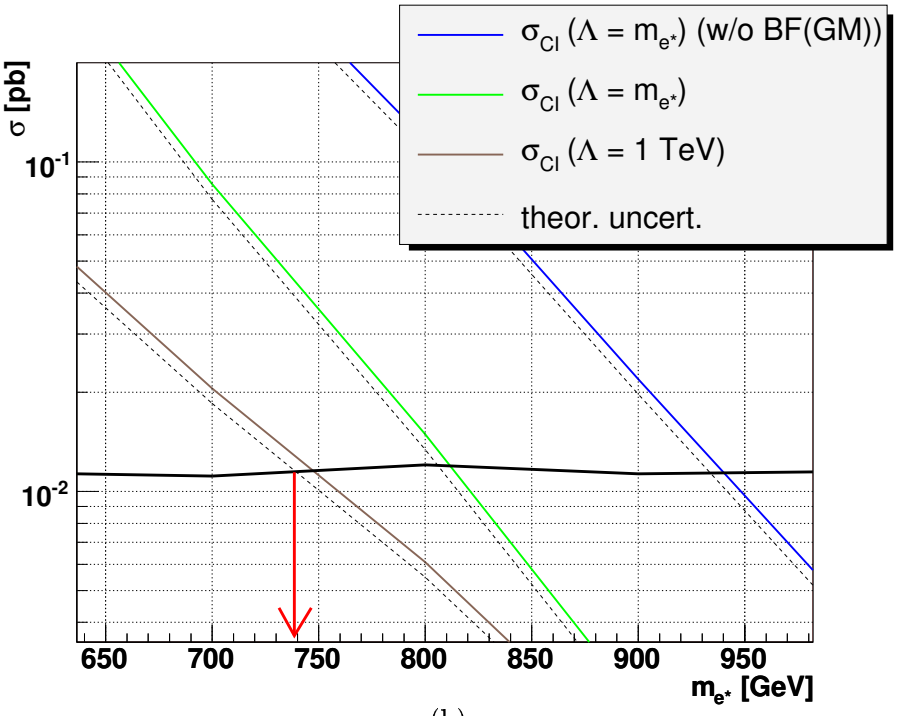

(b)

Figure 9.4.: (a) Limits for the production cross section of single excited electrons. (b) Limits on the production cross section for three different values of the compositeness scale. The arrow marks the lower mass limits for $\Lambda = 1$ TeV. The limits are at 95%CL.

at Fig. 9.4 (b), the dependency on the compositeness scale Λ becomes clear again, as well as the consideration of the two possible interaction.

9.3. Limits on the Compositeness Scale Λ

Limits on the compositeness scale are set. Those limits are as important and interesting as the limits on the cross section because Λ characterizes the interaction for all excited quarks and leptons (see Ch. 3). The choice for the compositeness scale $\Lambda = 1\,\text{TeV}$ is quite arbitrary, since the underlying interaction is not known.

The Limits on the cross section can be interpreted directly as limits on Λ. Therefore, the lower mass limit for different values of Λ is determined and plotted in Fig. 9.5.

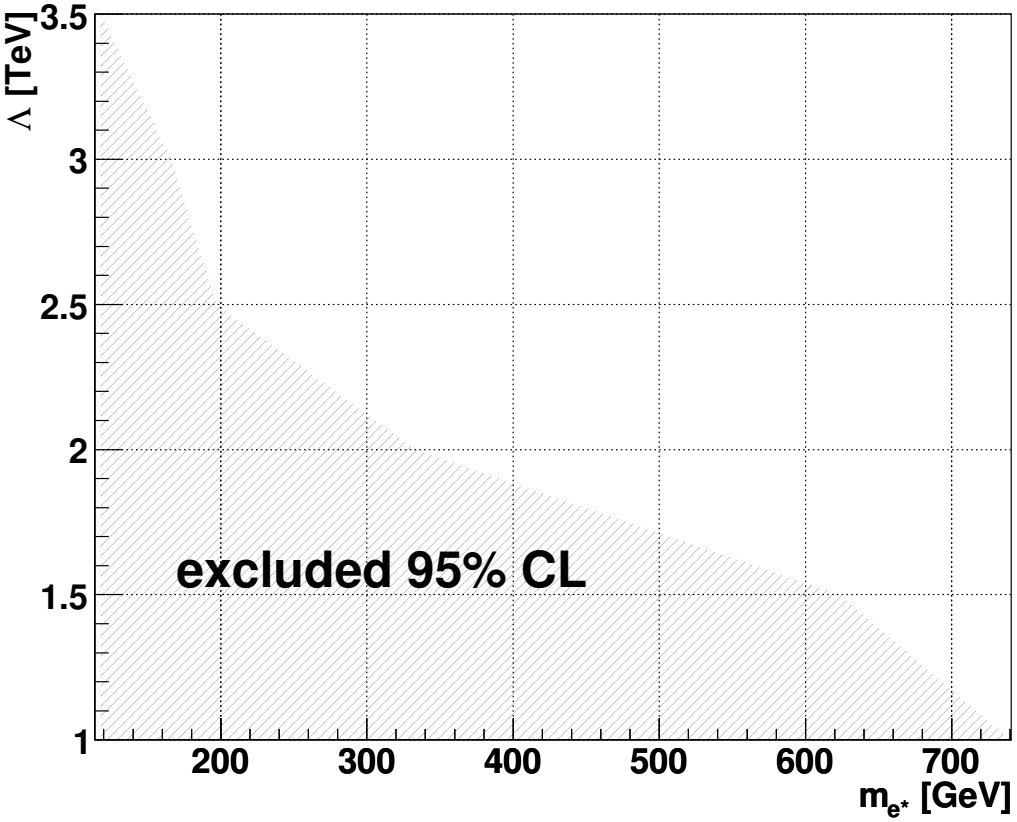

Figure 9.5.: The limit on the compositeness scale Λ 95% CL

9.4. Estimations for Gauge mediated Interaction

As explained in Sec. 8.4, estimations of limits for the production cross section via gauge meditated interaction (GM) can be obtained.

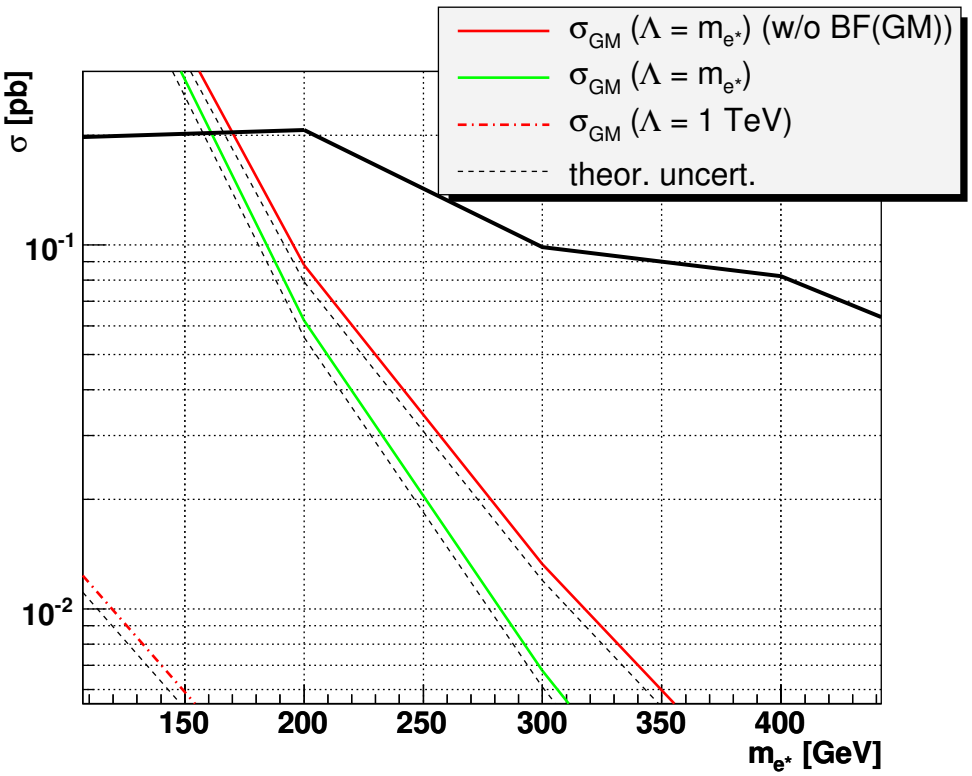

Figure 9.6.: Limits for the production cross section via contact interaction. For limit estimations, the production cross sections via gauge mediated interaction are shown.

Fig. 9.6 shows the lower mass part of Fig. 9.4 (a). Considering an acceptance for excited electrons produced via GM interaction at least as good as for those produced via CI, the limits obtained in this analysis can be used to estimate conservatively limits for GM production cross section.

The relatively large number of SM background and data events causes an increase of the limit for lower invariant masses of the $e\gamma$ sample. Thus, another method should be used to select the electron. This would make competitive limit on the production cross section via GM possible. However, another method was not used in this work.

10. Conclusions

The first search for the production of single excited electrons at the DØ experiment is presented in this analysis. Considered is the production of single excited electrons via contact interaction and their decay via gauge-mediated interaction ($q\bar{q} \to e^*e \to ee\gamma$).

The analyzed data was recorded during Run IIa and corresponds to an integrated luminosity of about $1\,\mathrm{fb}^{-1}$. Monte Carlo events for the Standard Model background are considered. However, its contribution decreases rapidly to higher invariant masses of the final state. The data agrees with the Standard Model background.

Studies for excited electron production via gauge-mediated interaction are presented, based on generator level information of Monte Carlo events generated with CompHEP. Furthermore, estimations on the limit for the production cross section via gauge mediated interaction were presented.

Since no excess in data was observed, upper limits on the production cross section via contact interaction and lower limits on the mass of excited electrons are set. Different values for the compositeness scale Λ are considered. The parameters f and f' that affect the coupling, are chosen equal one.

The lower mass limit for $\Lambda = 1\,\mathrm{TeV}$ is $m_{e^*} = 739\,\mathrm{GeV}$. For $\Lambda = m_{e^*}$ and without consideration of the contact interaction decay channel, a lower limit of $m_{e^*} = 934\,\mathrm{GeV}$ was obtained. These are the most stringent limits up to date set on excited electrons. Also in comparison to limits on the other two Standard Model leptons, this analysis sets the world best limits.

A. Implementation of Excited Electron Production via Gauge-Mediated Interaction into CompHEP

The generation of excited electrons produced via gauge-mediated interaction was performed on parton level with CompHEP. The necessary implementations are explained in this appendix. The Feynman rules, which are required in CompHEP (App. A.2), were obtained with LanHEP (App. A.1) from the Lagrangian that describes the interaction.

More information about LanHEP and CompHEP can be found at [56, 57], respectively.

A.1. LanHEP - The Generation of Lagrangians

LanHEP is a program which generates Feynman rules for CompHEP from a known Lagrangian. In this analysis, the Lagrangian for the production of excited electrons via gauge-mediated interaction $q\bar{q} \to V \to e^*e$ was implemented (see Fig. A.1)

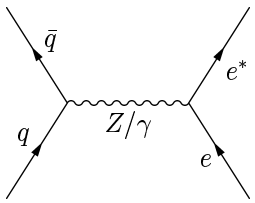

Figure A.1.: Feynman graph for the generated process $q\bar{q} \to Z/\gamma^* \to e^*e$.

$$\mathcal{L} = \frac{1}{2\Lambda}\bar{f}_R^*\sigma^{\mu\nu}\left(gf\frac{\tau}{2}W_{\mu\nu} + g'f'\frac{Y}{2}B_{\mu\nu}\right)f_L + H.c. \tag{A.1}$$

This implementation can be arranged analog for the other excited fermions.

At first, a main file was created, that accesses sub-files. These are explained respectively its implementation in the main file.

eStar.mdl:

```
% start LanHep for eStar gauge mediated interaction model
model eStar/1.
% read the different source files
% for variables
read eStar_var.
% for particles
read eStar_prt.
% for substitutions
read eStar_let.
% for Lagrangian
read eStar_lag.
```

Necessary parameters have to be declared. This includes the mass of the generated particles, as well as constants that are used in the Lagrangian. These constants are explained in more detail in Ch. 3.

eStar_var.mdl:

```
parameter
MESTAR     = 200 : 'excited electron mass',
EE         = 0.31333 : 'em coupling constant (<->1/128)',
GG         = 0.1187 : 'strong coupling constant (mZ)',
SW         = 0.4808 : 'sine of Weinberg angle',
CW         = sqrt(1-SW**2) : 'cosine of Weinberg angle',
LAMBDA     = 1000 : 'compositeness scale',
Wwidth     = 2.124 : 'width of the W boson,
Zwidth     = 2.4952 : 'width of the Z boson',
eStarwidth = 0.0521033 ; 'width of the excited electron',
Y          = -1.0 : 'weak hyper-charge',
f1         =  1.0 : 'fst composite dynamics parameter',
f2         =  1.0 : 'snd composite dynamics parameter'.

% TEX names
SetTexName([e1='e',E1='\\bar{e}']).
SetTexName([n1='\\nu^e',N1='\\bar{\\nu^e}']).
SetTexName([eS='e^*',Es='\\bar{e^*}']).
SetTexName([n1s='\\nu^*',N1S='\\bar{\\nu^*}']).
SetTexName([EE='e',SW='\\sin\\Theta_W',CW='\\cos\\Theta_W']).
SetTexName([LAMBDA='\\Lambda']).
```

Then the particles were introduced. For consistency reasons the complete isospin doublet is needed. Thus, the excited neutrino was implemented, too. Its characteristics were not specified, since they do not influence the production of the excited electron.

eStar_prt.mdl:

```
% particles

spinor e1/E1   : ('electron', mass me=0.000511).
spinor n1/N1   : ('neutrino', mass mN1 = 0.0).
spinor eS/Es   : ('ex el', mass MESTAR, width eSw = eStarwidth).
spinor n1s/N1S : ('ex e-neu').
vector
  A/A     : (photon, gauge),
  Z/Z : ('Z boson', mass MZ = 91.188, width Zw= Zwidth, gauge),
  'W+'/'W-':('W boson',mass MW = 80.425,width Ww= Wwidth,gauge).
```

LanHEP supports the feature to use substitutions. This was used to keep the code clear.

eStar_let.mdl:

```
% substitutions
% coupling constants
let g = EE/SW,
    g1= EE/CW.

% SU(2) gauge field strength
let W3         = CW*Z + SW*A,
    W          = {'W+', W3, 'W-'},
    FW^mu^nu^a = deriv^nu*W^mu^a
               - deriv^mu*W^nu^a
               + i*g*eps^a^b^c*W^nu^b*W^mu^c.

% U(1) gauge field strength
let B0       = -SW*Z + CW*A,
    FB^mu^nu = deriv^nu*B0^mu
             - deriv^mu*B0^nu.

let Sigma^a^b^mu^nu = i/2*(gamma^a^c^mu*gamma^c^b^nu
                    - gamma^a^c^nu*gamma^c^b^mu).
```

They main part is the Lagrangian (Eq. A.1). The usage of indices is not compulsory and not applied for more facility of inspection.

eStar_lag.mdl:

```
% Lagrangian for gauge mediated production of e*

lterm -1/(2*LAMBDA)*{N1S,Es}*Sigma*
      (g*f1*taupm/2*FW + g1*f2*Y/2*FB)
      *{n1,e1}
      + AddHermConj.
```

The resulting code was implemented in CompHEP and is explained in App. A.2.

A.2. CompHEP – Implementation of Feynman Rules

CompHEP allows the implementation of new models as well as extensions of existing ones, i. e. the QED, the electro-weak 4-fermion interaction, and the Standard Model[1]. Every particle interaction model in CompHEP is based on four files, which can be varied by the user. In this appendix only extensions of the SM (Feynman gauge), that were necessary for the implementation of excited electrons, are discussed.

In the file `vars.mdl` independent parameters are introduced. In the case of excited electrons the mass, the compositeness scale, the weak hyper-charge, and the to dynamics parameter are implemented.

vars.mdl:

```
Parameters
Name   | Value |> Comment                        <|
MESTAR|200     |excited electron mass
LAMBDA|1000    |compositeness scale
Y      |-1      |weak hyper-charge
f1     |1       |fst composite dynamics parameter
f2     |1       |snd composite dynamics parameter
```

Constraints for these parameters are listed in `func.mdl`. It is only the width of the excited electron.

func.mdl:

```
Constraints
Name   |> Expression                  <|> Comment            <|
eSw    |MESTAR^3/LAMBDA^2*0.00651292  | width of ex el
```

Each particle is characterized in `prtcls.mdl`. As mentioned in App. A.1, the excited neutrino was introduced additionally.

[1] for Feynman gauge as well as unitary gauge

prtcls.mdl:

```
Particles
Full name| A   | A+ |2*spin| mass | width| color| aux|>LaTex(A)<|
>LaTeX(A+)<|
ex el     | eS | Es | 1    |MESTAR| eSw  | 1    |    |e^*       |
\bar\{e^*\}
ex e-neu | n1s| N1S| 1    |0     | 0    | 1    |    |\nu^*     |
\bar\{\nu^*\}
```

The needed interaction vertices are listed in `lgrng.mdl`. It consists of the interacting particles, factor, and Lorentz part. Its meaning becomes clear looking at the derivative of the action S over the fields

$$\frac{S}{\delta A1_{[m1]}(p1)\,\delta A2_{[m2]}(p2)\,\delta A3_{[m3]}(p3)} = (2\pi)^2\delta(p1+p2+p3)[\gamma_0]\,Color\ Structur\cdot factor\cdot Lorentz\ part \quad \text{(A.2)}$$

where p and m are the 4-momenta and Lorentz indices. In Eq. A.2 the interaction of three particles was realized. This file is the main contribution of LanHEP and would be tedious to calculate manually.

lgrng.mdl:

```
Vertices
A1 | A2 | A3 | A4 |>         Factor                          <|
> Lorentz part                                      <|
E1 | eS | A  |    |-EE/(4*LAMBDA)                              |
f1*G(p3)*G(m3)-f1*G(m3)*G(p3)-Y*f2*G(p3)*G(m3)+Y*f2*G(m3)*G(p3)
E1 | eS | Z  |    |-EE/(4*CW*LAMBDA*SW)                        |
CW^2*f1*G(p3)*G(m3)-CW^2*f1*G(m3)*G(p3)+SW^2*Y*f2*G(p3)*G(m3)-SW
^2*Y*f2*G(m3)*G(p3)
E1 | n1s| W- |    |EE*Sqrt2*f1/(4*LAMBDA*SW)                   |
G(p3)*G(m3)-G(m3)*G(p3)
Es | e1 | A  |    |EE/(4*LAMBDA)                               |
f1*G(m3)*G(p3)-f1*G(p3)*G(m3)-Y*f2*G(m3)*G(p3)+Y*f2*G(p3)*G(m3)
Es | e1 | Z  |    |EE/(4*CW*LAMBDA*SW)                         |
CW^2*f1*G(m3)*G(p3)-CW^2*f1*G(p3)*G(m3)+SW^2*Y*f2*G(m3)*G(p3)-SW
^2*Y*f2*G(p3)*G(m3)
Es | n1 | W- |    |-EE*Sqrt2*f1/(4*LAMBDA*SW)                  |
G(m3)*G(p3)-G(p3)*G(m3)
N1 | eS | W+ |    |EE*Sqrt2*f1/(4*LAMBDA*SW)                   |
G(p3)*G(m3)-G(m3)*G(p3)
N1 | n1s| A  |    |EE/(4*LAMBDA)                               |
f1*G(p3)*G(m3)-f1*G(m3)*G(p3)+Y*f2*G(p3)*G(m3)-Y*f2*G(m3)*G(p3)
N1 | n1s| Z  |    |EE/(4*CW*LAMBDA*SW)                         |
CW^2*f1*G(p3)*G(m3)-CW^2*f1*G(m3)*G(p3)-SW^2*Y*f2*G(p3)*G(m3)+SW
^2*Y*f2*G(m3)*G(p3)
N1S| e1 | W+ |    |-EE*Sqrt2*f1/(4*LAMBDA*SW)                  |
G(m3)*G(p3)-G(p3)*G(m3)
```

```
N1S| n1 | A  |    |-EE/(4*LAMBDA)                                  |
f1*G(m3)*G(p3)-f1*G(p3)*G(m3)+Y*f2*G(m3)*G(p3)-Y*f2*G(p3)*G(m3)
N1S| n1 | Z  |    |-EE/(4*CW*LAMBDA*SW)                            |
CW^2*f1*G(m3)*G(p3)-CW^2*f1*G(p3)*G(m3)-SW^2*Y*f2*G(m3)*G(p3)+SW
^2*Y*f2*G(p3)*G(m3)
E1 | eS | W+ | W- |EE^2*f1/(4*LAMBDA*SW^2)                        |
G(m4)*G(m3)-G(m3)*G(m4)
E1 | n1s| A  | W+ |EE^2*Sqrt2*f1/(4*LAMBDA*SW)                    |
G(m3)*G(m4)-G(m4)*G(m3)
E1 | n1s| W+ | Z  |CW*EE^2*Sqrt2*f1/(4*LAMBDA*SW^2)               |
G(m4)*G(m3)-G(m3)*G(m4)
Es | e1 | W+ | W- |EE^2*f1/(4*LAMBDA*SW^2)                        |
G(m4)*G(m3)-G(m3)*G(m4)
Es | n1 | A  | W+ |EE^2*Sqrt2*f1/(4*LAMBDA*SW)                    |
G(m3)*G(m4)-G(m4)*G(m3)
Es | n1 | W+ | Z  |CW*EE^2*Sqrt2*f1/(4*LAMBDA*SW^2)               |
G(m4)*G(m3)-G(m3)*G(m4)
N1 | eS | A  | W- |EE^2*Sqrt2*f1/(4*LAMBDA*SW)                    |
G(m4)*G(m3)-G(m3)*G(m4)
N1 | eS | W- | Z  |CW*EE^2*Sqrt2*f1/(4*LAMBDA*SW^2)               |
G(m3)*G(m4)-G(m4)*G(m3)
N1 | n1s| W+ | W- |-EE^2*f1/(4*LAMBDA*SW^2)                       |
G(m4)*G(m3)-G(m3)*G(m4)
N1S| e1 | A  | W- |EE^2*Sqrt2*f1/(4*LAMBDA*SW)                    |
G(m4)*G(m3)-G(m3)*G(m4)
N1S| e1 | W- | Z  |CW*EE^2*Sqrt2*f1/(4*LAMBDA*SW^2)               |
G(m3)*G(m4)-G(m4)*G(m3)
N1S| n1 | W+ | W- |-EE^2*f1/(4*LAMBDA*SW^2)                       |
G(m4)*G(m3)-G(m3)*G(m4)
```

Bibliography

[1] The LEP Electroweak Working Group. URL: `http://lepewwg.web.cern.ch/LEPEWWG`, (24/09/06).

[2] Catani, S. Aspects of QCD, from the Tevatron to the LHC. 2000.

[3] S. Chekanov et al. A zeus next-to-leading-order qcd analysis of data on deep inelastic scattering. *Phys. Rev.*, D67:012007, 2003, hep-ex/0208023.

[4] Fermilab Visual Media Service. URL: `http://www-visualmedia.fnal.gov/VMS_Site_2/gallery/photography.shtml`, (24/09/06).

[5] M. Hohlfeld. *Suche nach Endzuständen mit zwei Leptonen und fehlender transversaler Energie in $p\bar{p}$ Kollisionen bei einer Schwerpunktsenergie von 1.96 TeV.* PhD thesis, Johannes Gutenberg Universität Mainz, 2004. In german.

[6] RunII Stores and D0 Global Physics Runs. URL: `http://www-d0.fnal.gov/runcoor/d0_private/operations/stores_runs.html`, (24/09/06). Not public.

[7] W.-M. Yao et al. Review of Particle Physics. *Journal of Physics G*, 33:1+, 2006.

[8] Trigger Meisters' Webpage. URL: `http://www-d0online.fnal.gov/www/groups/tm/tm_main.html`, (24/09/06).

[9] F. Halzen and A. D. Martin. *Quarks and Leptons: An Introductory Course in Modern Particle Physics.* J. Wiley & sons, Inc., 1984.

[10] P. Schmüser. *Feynman-Graphen und Eichtheorien für Experimentalphysiker.* Springer, 1995.

[11] Ch. Berger. *Elementarteilchenphysik: Von den Grundlagen zu den modernen Experimenten.* Springer, 1992.

[12] Glashow, S. L. Partial Symmetries of Weak Interactions. *Nucl. Phys.*, 22:579–588, 1961.

[13] Weinberg, S. A Model of Leptons. *Phys. Rev. Lett.*, 19:1264–1266, 1967.

[14] Salam, A. *Elementary Particle Theory.* 1968.

[15] R. Barate et al. Search for the standard model Higgs boson at LEP. *Phys. Lett.*, B565:61–75, 2003, hep-ex/0306033.

[16] P. Bagnaia et al. Evidence for $Z \to e^+e^-$ at the CERN anti-p p collider. *Phys. Lett.*, B129:130–140, 1983.

[17] Peter W. Higgs. Broken Symmetries and the Masses of Gauge Bosons. *Phys. Rev. Lett.*, 13:508–509, 1964.

[18] Super-Kamiokande Collaborators Page. URL: `http://www-sk.icrr.u-tokyo.ac.jp/sk/index-e.html`, (24/09/06).

[19] W.-M. Yao et al. Neutrino Physics. URL: `http://hitoshi.berkeley.edu/neutrino/ref2006.html`, (24/09/06).

[20] V. M. Abazov et al. Search for excited muons in $p\bar{p}$ collisions at $\sqrt{s} = 1.96\,\text{TeV}$. *Phys. Rev.*, D73:111102, 2006, hep-ex/0604040.

[21] D. Acosta et al. Search for excited and exotic electrons in the $e\gamma$ decay channel in $p\bar{p}$ collisions at $\sqrt{s} = 1.96\,\text{TeV}$. *Phys. Rev. Lett.*, 94:101802, 2005, hep-ex/0410013.

[22] O. J. P. Eboli, S. M. Lietti, and Prakash Mathews. Excited Leptons at the CERN Large Hadron Collider. *Phys. Rev.*, D65:075003, 2002, hep-ph/0111001.

[23] O. Cakir, C. Leroy, Rashid R. Mehdiyev, and A. Belyaev. Production and decay of excited electrons at the LHC. *Eur. Phys. J. direct*, C30:005, 2003, hep-ph/0212006.

[24] U. Baur, M. Spira, and P. M. Zerwas. Excited Quark and Lepton Production at Hadron Colliders. *Phys. Rev.*, D42:815–824, 1990.

[25] G. Abbiendi et al. Search for charged excited leptons in e+ e- collisions at $\sqrt{s} = 183\,\text{GeV} - 209\,\text{GeV}$. *Phys. Lett.*, B544:57–72, 2002, hep-ex/0206061.

[26] N. Cabibbo, L. Maiani, and Y. Srivastava. Anomalous Z Decays: Excited Leptons? *Phys. Lett.*, B139:459, 1984.

[27] Stanley J. Brodsky and S. D. Drell. The Anomalous Magnetic Moment and Limits On Fermion Substructure. *Phys. Rev.*, D22:2236, 1980.

[28] B. Lee Roberts. Muon (g-2): Past, Present and Future. *Nucl. Phys. Proc. Suppl.*, 155:372–374, 2006, hep-ex/0510056.

[29] Torbjorn Sjostrand, Leif Lonnblad, Stephen Mrenna, and Peter Skands. PYTHIA 6.3: Physics and manual. 2003, hep-ph/0308153.

[30] E. Boos et al. CompHEP 4.4: Automatic computations from Lagrangians to events. *Nucl. Instrum. Meth.*, A534:250–259, 2004, hep-ph/0403113.

[31] Coenen, J.W. *Search for Excited Muons in $p\bar{p}$-Collisions at $\sqrt{s} = 1.96\,\text{TeV}$.* Diploma Thesis, RWTH Aachen, 2005.

[32] HERA Home Page. URL: `http://adweb.desy.de/mpy/hera`, (24/09/06).

[33] S. W. Herb et al. Observation of a dimuon resonance at 9.5 GeV in 400 GeV proton - nucleus collisions. *Phys. Rev. Lett.*, 39:252–255, 1977.

[34] S. Abachi et al. Observation of the top quark. *Phys. Rev. Lett.*, 74(14):2632–2637, Apr 1995.

[35] F. Abe et al. Observation of top quark production in $p\bar{p}$ collisions with the collider detector at fermilab. *Phys. Rev. Lett.*, 74(14):2626–2631, Apr 1995.

[36] M. Nakamura. Result from DONUT: Direct observation of nu/tau interaction. *Nucl. Phys. Proc. Suppl.*, 77:259–264, 1999.

[37] Fermilab Beams Division. The Tevatron Accelerator Complex. (24/09/06). URL:`http://www-bdnew.fnal.gov/operations/rookie_books/rbooks.html`.

[38] The Fermilab Tevatron Collider. URL:`http://www-bd.fnal.gov/runII/index.html`, (24/09/06).

[39] S. Abachi et al. The DØ Detector. *Nucl. Instrum. Meth.*, A338:185–253, 1994.

[40] V. M. Abazov et al. The upgrade DØ Detector. 2005, physics/0507191.

[41] D. Chapin, H. Fox, J. Gardner, R. Illingworth, and J. Zhu A. Lyon. Measurement of $Z \to ee$ and $W \to e\nu$ Production Cross Sections with $|\eta| < 2.3$. 6. DØ Note 4403.

[42] The Data Quality Group. URL:`http://www-d0.fnal.gov/computing/data_quality/d0_private`, (24/09/06). Not public.

[43] How to lumi? – DØ Wiki Page. URL:`https://plone4.fnal.gov/P1/D0Wiki/top/howto-lumi`, (24/09/06). Not public.

[44] G. Snow for the Luminosity Working Group. Adjustments to the Measured Integrated Luminosity in Run IIa. 2006. DØ Note 5139.

[45] P. Verdier. private communication, 15/09/06.

[46] DØ Farm Production. URL:`http://www-d0.fnal.gov/computing/production/Welcome.html`, (24/09/06).

[47] A. Baranovski et al. SAM: Sequential access via meta data. *Fermilab-TM-2175*, (24/09/06). URL:`http://www-d0.fnal.gov/computing/sam/`.

[48] Common Analysis Format. URL:`http://www-d0.fnal.gov/Run2Physics/cs/caf`, (24/09/06).

[49] R. Brun et al. ROOT Users Guide 5.12.

[50] The EM-ID Group. URL:`http://www-d0.fnal.gov/phys_id/emid/d0_private/certification/welcome.html`, (24/09/06). Not Public.

[51] The CAF EM-ID Cuts Package. URL: `http://www-d0.fnal.gov/d0dist/dist/packages/emid_cuts/v02-04-07/doc/`, (24/09/06).

[52] J. Hays, J. Mitrevski, C. Schwanenberger, and T. Toole. Single Electron Efficiencies in p17 Data and Monte-Carlo Using p18.05.00 d0correct. 2004. DØ Note 5105.

[53] S. Anderson and others, (DØProduction Group). Measurement of $t\bar{t}$ cross section at $\sqrt{s} = 1.96\,\text{TeV}$. 2003. DØ note 4116.

[54] J. Pumplin et al. New Generation of Parton Distributions with Uncertainties from Global QCD Analysis. *JHEP*, 0207:012, 2002.

[55] D. Stump et al. Inclusive Jet Production, Parton Distributions, and the Search for New Physics. *JHEP*, 0310:046, 2003.

[56] A. Pukhov et al. CompHEP: A package for evaluation of Feynman diagrams and integration over multi-particle phase space. User's manual for version 33. 1999, hep-ph/9908288.

[57] A. V. Semenov. LanHEP: A Package for Automatic Generation of Feynman Rules in Field Theory. Version 2.0. 2002, hep-ph/0208011.

[58] DØGEANT Simulation of the Total Apparatus Response (D0gstar). URL: `http://www-d0.fnal.gov/computing/MonteCarlo/simulation/d0gstar.html`, (24/09/06).

[59] D0sim. URL: `http://www-d0.fnal.gov/computing/MonteCarlo/simulation/d0sim.html`, (24/09/06).

[60] Drell-Yan, Z/W cross-sections. URL: `http://www-clued0.fnal.gov/~nunne/cross-sections/dy_cross-sections.html`, (24/09/06).

[61] B. Tiller and T. Nunnemann. Measurement of the differential Z^0-boson production cross-section as function of transverse momentum. 2004. DØ Note 4660.

[62] The CAF_MC_UTIL Package. URL: `http://www-d0.fnal.gov/d0dist/dist/packages/caf_mc_util/v01-02-07/doc/html/`, (24/09/06).

[63] MCFM Cross Sections. URL: `http://www-clued0.fnal.gov/~nunne/cross-sections/mcfm_cross-sections.html`, (24/09/06).

[64] R. Hamberg, W. L. van Neerven, and T. Matsuura. A Complete calculation of the order α_s^2 correction to the Drell-Yan K factor. *Nucl. Phys.*, B359:343–405, 1991.

[65] Common Sample Group. URL: `http://www-d0.fnal.gov/Run2Physics/cs/index.html`, (24/09/06).

[66] A. Das and U. Heintz. Search for Randall-Sundrum Gravitons in di-lepton and di-photon final states with $1\,fb^{-1}$ of Data. 2006. DØ Note 5153.

[67] H. Kim and J. Yu. A search for $Wb\bar{b}$ and WH production in $p\bar{p}$ collisions at $\sqrt{s} = 1.96\,\text{TeV}$ with full data set of Pass2. 2005. DØ Note 4706.

[68] Y. Maravin A. Ferapontov. Study of $Z\gamma$ events in DØRun II p17 data. 2006. DØ note5156.

[69] A. Askew S. Mattingly. Measurement of Anomalous Coupling Limits in $W\gamma$ Events. 2005. DØ note 4686.

[70] Y. Gershtein and Y. Maravin. Search for GMSB SUSY in di-photon events with large missing $\not\!\!E_T$. 2006. DØ Note 5019.

[71] J. Hays et al. Electron Trigger Efficiencies using Calorimeter Information in p17 Data. 2006. DØ note 5138.

[72] V. Büscher and J.-F. Grivaz, T. Nunnemann, M. Wobisch. Conclusions of Mini-Workshop on PDF uncertainties and related topics. 2004. DØ note 4618.

[73] V. Büscher, J.-F. Grivaz, J. Hobbs and others. Recommendation of the Ad-Hoc Committee on Limit-Setting Procedures to be Used by DØin Run II. 2004. DØ note 4629.

[74] Simple Limit Calculator. URL:`http://www-clued0.fnal.gov/~hobbs/limit_calc/limit_calc.html`, (28/09/06).

Danksagung

An erster Stelle möchte ich meinen Eltern danken, die mir dieses Studium ermöglicht haben – und das nicht nur aus finanzieller Sicht.

Prof. Dr. Thomas Hebbeker danke ich für die Möglichkeit, diese Diplomarbeit schreiben zu dürfen. Er hat mich während dieses Jahres immer unterstützt und mir ausserdem ermöglicht, das DØ Experiment live zu sehen und meine vorläufigen Ergebnisse auf dem DØ Workshop in Manchester vorzustellen. Vielen Dank.

Danke auch an Prof. Dr. Martin Erdmann für die Zweitkorrektur dieser Arbeit.

Mein Dank gilt auch Dr. Arnd Meyer für die ausgezeichnete Betreuung – auch von der anderen Seite des Ozeans aus. Ein besonderes Dankeschön für die Führung durch den DØ Detektor.

Desweiteren möchte ich der DØ Gruppe in Aachen danken für die vielen Anregungen während des wöchentlichen Meetings. Speziell Carsten Magass danke ich für die Hilfestellungen, besonders zu Beginn meiner Diplomarbeit. Auch Christian Autermann danke ich für die Geduld, meine tausend kleinen und kurzen Fragen zu beantworten, sowie für die gute Stimmung im Büro.

This thesis would be impossible without the DØ collaboration, especially Patrice Verdier, Olav Mundal, Yurii Maravin, Satish Desai, Pedrame Bargassa, and Reinhard Schwienhorst.

Der verrückten Mittagessencrew danke ich für die knappe Stunde Entspannung und Erheiterung jeden Mittag.

Danke an Maike Trenkel für die Unterstützung bei der gauge mediated interaction, sowie für das Korrekturlesen. Für Letzteres danke ich ausserdem Daniel Lenz, Benedikt Mura und Christian Autermann. Für den Blick aus der Aussenwelt danke ich Frank 19-Worte Heuer.

Die gute Stimmung beim Drucken verdanke ich Heidrun Boers, Ulrike Vorwerk, Daniel Lenz, Michael Henke und Benedikt Mura. Prost!

Urte gogor honetan Alemania nahiz Euskal Herrian elkarrekin emandako uneetan eta dei goiztiar bakoitzean helarazi didan indarra nire Aratz maiteari bihotz-bihotzez eman nahi dizkiot eskerrak.

Danke, Danke, Popanke...